

THE FLORIDA STATE UNIVERSITY
COLLEGE OF ARTS AND SCIENCES

NUMERICAL SIMULATION OF THE PLANETARY
BOUNDARY LAYER OVER BARBADOS W.I.


By
JOHN D. LEE

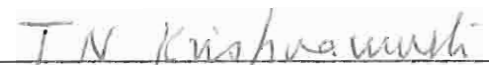
A Dissertation submitted to
the Department of Meteorology
in partial fulfilment of the
requirements for the degree of
Doctor of Philosophy

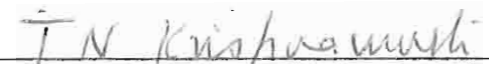
Approved:



Professor directing Dissertation









August, 1973

ABSTRACT

A two-dimensional, four-layer model is developed to simulate the low tropospheric flow over Barbados, W.I., under unsaturated quasi-non-divergent synoptic conditions. Observations indicate that under these conditions the sub-cloud flow over the island is characterized by daytime low-level divergence and minimum cloudiness associated with maximum surface heating, and nighttime low-level convergence with higher frequency of shower activity, especially over the western half of the island. Physical explanations are sought in the model for this unusual behavior of the flow over a small heated tropical island.

The mathematical model consists of layer-averaged equations for the conservation of momentum, mass, moisture, and thermodynamic energy of a Boussinesq fluid in hydrostatic balance. Integrations are made on an f -plane with the effects of moisture on momentum included through the use of virtual potential temperature in the buoyancy expression of the pressure gradient term. Turbulent diffusion processes are parameterized, but moisture phase changes are omitted, and convective processes must be inferred only from the vertical motion fields.

The model includes variable vertical diffusion and surface drag coefficients, variable surface topography, implied time and space-dependent surface heating, and variable initial conditions of the flow and moisture fields. The initial temperature field is neutrally stratified. Stretch coordinates are used to permit high resolution in the vicinity of the

island, and a large enough model width to minimize lateral boundary effects on the interior solutions.

The results indicate that

- (a) The Ekman balance assumption as an initial condition should be avoided in boundary layer models including topography and large changes in surface friction characteristics.
- (b) Nonlinear advection is important over topography, therefore linear analysis is inappropriate for models with topography.
- (c) Topography plays a dominant role in the modification of low-level flow over isolated heat sources, and
- (d) Small variations in topographic geometry can lead to significant changes in flow geometry.

With specific reference to Barbados, the model case studies indicate that

- (a) The low-level land-sea breeze maxima propagate off shore in the absence of a mean flow.
- (b) Advection intensifies the perturbation circulations and inhibits the propagation of the low-level maxima.
- (c) The perturbation circulations are intensified in the presence of moisture and in the absence of a land-sea surface moisture gradient,
- (d) Topography induces downward motions by day and upward motions at night over the western slope with maximum intensity of order 5 cm sec^{-1} near the time of maximum heating.
and
see also the time of maximum heating.
- (e) Precipitation inferred from perturbation flow and moisture fields is most likely at night over the western part of the island.

ACKNOWLEDGMENTS

The author gratefully acknowledges the guidance and supervision of Dr. James J. O'Brien, his major professor and thesis adviser, who suggested the problem. The author is also indebted to Drs. N. E. LaSeur, T. N. Krishnamurti, and A. I. Barcilon for their encouragement and helpful suggestions. The author's interest in problems of this nature is a result of his association with Dr. Michael Garstang. I would be guilty of gross negligence if I overlooked the many useful discussions I had with, and the many helpful ideas and words of encouragement I received from, my colleagues and fellow students, especially Messers Harley Hurlburt, Dana Thompson, and Richard Mc Nider. I was particularly fortunate in having Mr. McNider's wide programming expertise at my disposal. Computations were made on the CDC 6500 of the Florida State University's Computing Facility, and on the CDC 6600/7600 system of the National Center for Atmospheric Research. NCAR is sponsored by the National Science Foundation. This research was supported by Project Themis under Contract No. DAA E07-65-6-0061 with the U.S. Army Electronics Command, and partially by the Office of Naval Research, Contract N00014-67-A-235-002. Finally, the author expresses his gratitude to Dr. R. McWilliams of the Mathematics Department for serving on his committee, to Mrs. J. Richards and Mrs. G. Woodhouse for typing the manuscript, and to Dewey L. Rudd for Mathematics Department for serving on his committee, to Mrs. J. Richards and Mrs. G. Woodhouse for typing the manuscript, and to Dewey L. Rudd for drafting some of the diagrams.

TABLE OF CONTENTS

	Page
ABSTRACT	ii
ACKNOWLEDGMENTS	iv
LIST OF TABLES	vii
LIST OF ILLUSTRATIONS	viii
CHAPTER I	
INTRODUCTION	1
CHAPTER II	
THE MODEL	8
2.1 Initial Conditions	13
(a) Momentum and mass fields	13
(b) Temperature and moisture	16
2.2 Boundary conditions	18
(a) Upper boundaries	18
(b) Lower boundaries	19
(c) Lateral boundaries	22
2.3 Model depth	24
2.4 Stretch coordinates	25
2.5 Experiments and model parameters	27
2.5 Experiments and model parameters	27

	Page
CHAPTER III	
RESULTS	32
3.1 Case A: Sinusoidal topography, $u_g = 0$	34
3.2 Case B: Real island, $u_g = 0$	39
3.3 Case C: Flat island, $u_g = -4 \text{ sec}^{-1}$	46
3.4 Case D: Real island, $u_g = -4 \text{ m sec}^{-1}$	54
3.5 Perturbation temperature and moisture fields	64
3.6 Effect of variation of physical properties	69
(a) Constant versus variable heating	69
(b) Effect of moisture	70
(c) Effect of wind speed	71
CHAPTER IV	
COMPARISON WITH OBSERVATIONS	76
CHAPTER V	
SUMMARY AND CONCLUSIONS	79
APPENDICES	83
A. List of symbols	84
B. Derivation of model equations	88
REFERENCES	99
VITA	102

LIST OF TABLES

Table		Page
1	Coefficients a_n, b_n of the function $T(t)$	20
2	List of hypothetical case studies	28
3	Values of parameters or variables	29
4	Zonal perturbation velocity components over the coasts for Cases B, C, and D at the time of maximum temperature	64
5	Same as Table 4 but for Cases D, H, and I	70

LIST OF ILLUSTRATIONS

Figure		Page
1	Schematic representation of x-z model	7
2	Vertical profiles of the u-component, and hodographs for the undisturbed flow over the east coast (dashed), west coast (dotted), and hill crest (solid) for the real island with a specified easterly geostrophic wind of 4 m sec^{-1}	15
3	Adjustment of the u (lower) and v (upper) components from initial guess fields in the lowest layer over the crest of the island. Easterly geostrophic wind is 4 m sec^{-1} . Solid curves are for a uniform guess profile of 4 m sec^{-1} . Dashed curves are for a linear shear guess profile with an upper value of 4 m sec^{-1}	17
4	Amplitude of the time-dependent land-sea surface temperature difference, $T(t)$, at the center of the island. The initial time corresponds to 0600 LST. The dashed line is the 24 hr mean	21
5	Vertical profiles of the vertical diffusion coefficient over water (solid) and over the crest of the island (dashed)	31
6	Time variation of the maxima in the u-component of the symmetric sea (S) and land (L) breeze circulations (Case A). The initial time corresponds to 0600 LST	35
7	Perturbation streamfunctions for Case A at 1300 LST (left) and 0400 LST (right), the times of maximum and minimum surface temperature, respectively. Contour interval is $40 \text{ m}^2 \text{ sec}^{-1}$	37
8	Schematic of the propagation of the sea (S) and land (L) breeze maxima (Case A). The point S at 24 hr indicates resumption of the seabreeze. The dashed vertical lines indicate the coasts and the dashed horizontal lines indicate the times of maximum (L) breeze maxima (Case A). The point S at 24 hr indicates resumption of the seabreeze. The dashed vertical lines indicate the coasts and the dashed horizontal lines indicate the times of maximum (lower) and minimum (upper) surface temperature, respectively	38

Figure		Page
9	Same as Fig. 6 but for Case B	40
10	Same as Fig. 7 but for Case B	42
11	Same as Fig. 8 but for Case B	44
12	Same as Fig. 2 but for Case C	47
13	Vertical profiles of the u-component, and hodographs over the east coast (dashed), west coast (dotted) and the position of the hill crest (solid) at 1300 LST	49
14	Same as Fig. 13 but for 0400 LST	50
15	Same as Fig. 7 but for Case C	53
16	Same as Fig. 7 but for Case D	58
17	Same as Fig. 13 but for Case D	60
18	Same as Fig. 14 but for Case D	61
19	Same as Fig. 16 but for second heating cycle	62
20	u (upper) and v (lower) components in the lowest layer over the east coast (dashed), west coast (dotted) and hill crest (solid) as functions of time for Case D. The v-scale is magnified 10 times relative to the u-scale	63
21	Perturbation temperatures for Cases B (left) and D (right) at 1300 LST. Values range from 1 K to 9 K by increments of 2 K	65
22	Perturbation mixing ratio for Case B at 1300 LST (left) and 0400 LST (right). Units are 0.1 gm kg^{-1} . Contour interval is 4 units	67
23	Same as Fig. 22 but for Cases with mean flow	68
24	Same as Fig. 7 but for Case E	73
25	Same as Fig. 7 but for Case F	74
26	Same as Fig. 7 but for Case G	75
25	Same as Fig. 7 but for Case F	74
26	Same as Fig. 7 but for Case G	75

CHAPTER I

INTRODUCTION

The common concept of low-level flow over a heated island under unsaturated, quasi-nondivergent synoptic conditions requires that the island behave as a daytime heat source and a nighttime heat sink within a region of almost constant surface temperature. Thermally induced mesoscale low-level convergence with rising motions by day, and low-level divergence and sinking motions by night would normally be expected. Probability of showers is greater during the afternoon than at other times. Under these conditions superadiabatic lapse rates during the day and nighttime radiative temperature inversions near the surface are not unknown.

Observational studies by Garstang (1967), and DeSouza (1972) indicate that, in the absence of synoptic scale disturbances, the sub-cloud flow over Barbados is characterized by low-level daytime divergence and nighttime convergence, with maximum precipitation at night and minimum precipitation during the early afternoon. DeSouza (1972) also found that the period of maximum divergence and minimum cloudiness spanned the time of maximum surface heating. The observed temporal distribution of cloudiness and precipitation is similar to that observed by Garstang (1964) over oceanic regions to the east of the island, and one may surmise that, either (a) the island has no influence on the predominantly oceanic regime around it, or (b) the island has such a strong influence

on the lowest layers of the prevailing flow as to reverse the usual behavior of flows over heated islands. The hypothesis here is that the latter alternative is more plausible and the purpose of this study is to numerically integrate the hydrothermodynamic equations with a view to simulating, and investigating the mechanisms of the sub-cloud flow features observed over Barbados, W.I., under prevailing conditions devoid of synoptic scale disturbances. Physical explanations for the anomalous conditions observed over Barbados are sought in the model results.

Garstang (1967), using a simple momentum flux model, shows that the vertical redistribution of horizontal momentum in a sheared flow can account for the observed downward motions over the island by the downward flux of momentum. Ulanski (1971), using data collected in the Prandtl layer over Barbados in the summer of 1968, and DeScuza (1972), using data collected in the sub-cloud layer in the summers of 1968 and 1969, both support Garstang's hypothesis by the results of their observational studies. They postulate that the daytime heating of the sheared flow over Barbados causes a replacement of the rising warm low-level air with its lower momentum by sinking bubbles of colder air with their higher momentum, thus establishing low-level divergence and setting the pattern of sinking motion over the island. At night, the vertical exchange of momentum is reduced due to lack of heating, and frictional effects account for low-level convergence and rising motions over the island.

Although accounting for frictional and heating effects of the
over the island.

Although accounting for frictional and heating effects of the ground, the above studies tacitly neglect the effects of topography. It will be shown in this study that topography plays a dominant role in

producing daytime sinking motions over the western part of the island, and the reverse effect at night.

The problem of flow over heat sources of limited extent has been extensively studied in the past. A few pertinent results are provided by the linear models of Malkus and Stern (1953), Smith (1955, 1957), and Olfe and Lee (1971), and by the non-linear models of Lavoie (1968, 1972), and Estoque and Bhumralkar (1969). Bhumralkar (1972) has applied the model of Estoque and Bhumralkar (1969) to a study of air flow over Grand Bahama. The heat sources in all the above studies are flat, and except for Lavoie (1972) and Bhumralkar (1972) all studies exclude moisture.

Although the widths of the heat sources vary up to an order of magnitude and model physics differ, most of the results exhibit gross similarities. Except for Malkus and Stern (1953), the models show that in the presence of a basic flow, upward motion develops over the downwind edge of the heat source, and downward motion occurs over the upwind edge. Stern and Malkus (1953) obtained similar results by modifying the treatment of the heating function, thus correcting the anomalous circulation which developed in the earlier study by Malkus and Stern (1953). All models indicate that the strength and vertical shear of the basic current are important. Smith (1957) shows that with advection, downward motions upwind, and upward motions downwind intensify, and their regions expand and move downwind with time. Estoque and Bhumralkar (1969) show that size of the heat source and orientation of the basic flow are important. The effect of orientation of the basic flow relative to that of the heat source is also demonstrated by Lavoie (1968, 1972) and more recently by Pielke (1973) in a study of the South Florida seabreeze circulation. Bhumralkar (1972) shows that increasing the flow along the

heat source increases the intensity of the perturbation, while increasing the flow normal to the heat source has the opposite effect.

Lavoie (1968, 1972) also considers the effect of topography in the vicinity of the heat source. Raymond (1972), in an analytic study of air flow over an arbitrary ridge with diabatic heating and cooling, shows that the shape and size of the ridge are important, and that heating over the ridge dampens the perturbation in the air flow while cooling has the opposite effect.

The physical model used in this study assumes the atmosphere in the vicinity of the island to consist of $n+1$ discrete horizontally stratified quasi-incompressible fluid layers, counting upwards from the surface. The $n+1^{\text{th}}$ layer is assumed to be inactive, that is, it is assumed to be sufficiently deep so that disturbances introduced at its lower interface are completely damped internally. Thus, vertical velocities and x -directed pressure gradients vanish, and y -directed pressure gradients are constant somewhere within the layer. We shall assume that each layer is vertically homogeneous in horizontal momentum, potential temperature and moisture, and that each has a uniform undisturbed thickness H_k (away from any regions penetrated by surface topography), where the subscript k ($k = 1, 2, \dots, n+1$) identifies the general k^{th} layer.

Our interest lies in the response of the prevailing flow to surface induced disturbances in temperature and humidity, and to the effect of the interaction between sub-grid scale influences and the larger scale disturbances.

of the interaction between sub-grid scale influences and the larger scale disturbances.

In order to maintain modest computer requirements, a two-dimensional (x - z), four-layer model on an f -plane is considered. Surface

topography, when included, will be contained entirely within the lowest layer. The undisturbed depth of each layer is 500 m except in the presence of surface topography in the lowest layer. The Prandtl layer is arbitrarily chosen to be 50 m deep, and variations in surface roughness are neglected except between sea and land surfaces. Although north-south homogeneity is implied in a two-dimensional model, here, north-south variations in pressure are retained for consistency with a mean east-west geostrophic flow.

The hydrostatic assumption and Boussinesq approximation are invoked in this model. Dutton and Fichtl (1969) discuss at length the appropriateness of these assumptions.

Although the assumption of vertical homogeneity within each layer allows us to average out vertical advection terms, we expect grid scale convective heat and moisture fluxes to be important, thus vertical advection of temperature and moisture at the interfaces is retained. The convective transfer of temperature and moisture is achieved through the interfacial vertical velocities which are obtained from the continuity equation by treating the interfaces as material surfaces. In addition, sub-grid scale turbulent fluxes of all quantities are parameterized through the interfacial stresses.

The basic assumptions governing the model are:

1. North-south gradients other than pressure gradients are neglected.
2. Pressure is hydrostatic.
3. Vertical variations in density, wind velocity, potential temperature, and moisture within each layer are averaged out.
2. Pressure is hydrostatic.
3. Vertical variations in density, wind velocity, potential temperature, and moisture within each layer are averaged out.

4. Horizontal variations in surface roughness are neglected except for the variation from water to land surfaces.
5. Surface topography does not penetrate any interface above ground.
6. Radiational heating and cooling, latent heating, and heating by cumulus convection are neglected.

The geometry of the general model is shown schematically in Fig. 1.

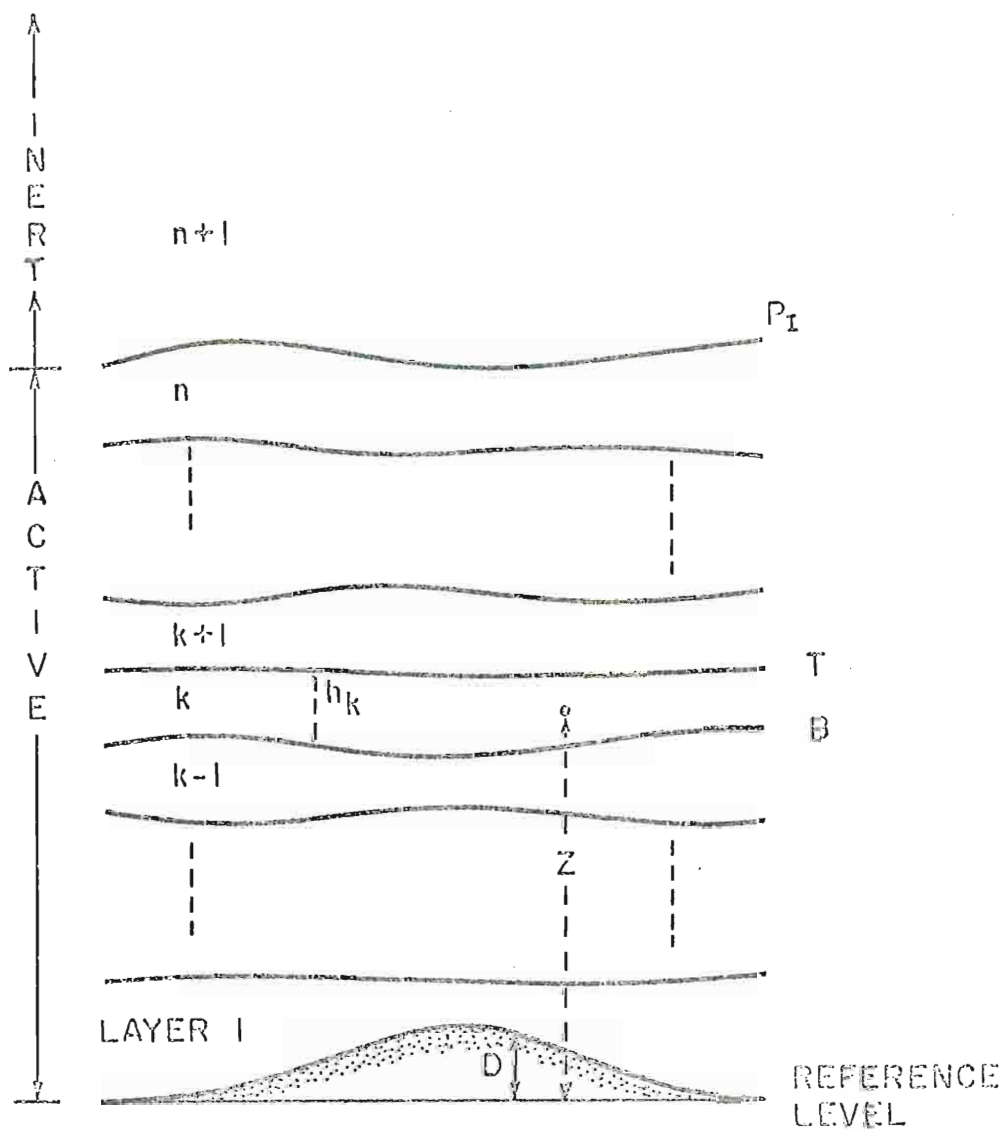


Fig. 1. Schematic representation of x - z model

CHAPTER II

THE MODEL

The mathematical model comprises the hydro-thermodynamic equations together with mass and moisture conservation equations for a Boussinesq viscous fluid in hydrostatic balance. The fluid is assumed to be stratified into four active layers each 500 m thick in their undisturbed state (except in the vicinity of surface topography), and each of which is horizontally stratified but assumed to be vertically homogeneous in the flow variables. Thus, the equations are vertically averaged. The development of the model equations closely follows the methods of Abdullah and O'Brien (1966), O'Brien and Reid (1967), Lavoie (1968, 1972), and O'Brien and Hurlburt (1972). Sub-grid scale eddy fluxes are parameterized by the bulk aerodynamic method at the surface, and through the use of a diffusion coefficient profile as suggested by O'Brien (1970) above the surface. Both methods are included at the surface in the heat and moisture equations since it is desirable to be able to drive the model from a static initial state, when the bulk formulation for heat flux which is dependent on the flow field will not transfer any heat from the surface and no perturbations will develop.

The basic model equations are

The basic model equations are

$$\frac{\partial u}{\partial t} = -u \frac{\partial u}{\partial x} - \frac{1}{\rho} \frac{\partial p}{\partial x} + f_v + \frac{\partial}{\partial x} \left(K_{MH} \frac{\partial u}{\partial x} \right) + \frac{1}{\rho} \frac{\partial \tau^x}{\partial z} \quad (1)$$

$$\frac{\partial v}{\partial t} = -u \frac{\partial v}{\partial x} - \frac{1}{\rho} \frac{\partial p}{\partial y} - fu + \frac{\partial}{\partial x} \left(K_{MH} \frac{\partial v}{\partial x} \right) + \frac{1}{\rho} \frac{\partial \tau^x}{\partial z} \quad (2)$$

$$\frac{\partial u}{\partial x} + \frac{\partial w}{\partial z} = 0$$

$$\frac{\partial \theta}{\partial t} = -u \frac{\partial \theta}{\partial x} - w \frac{\partial \theta}{\partial z} + \frac{\partial}{\partial x} \left(K_{QH} \frac{\partial \theta}{\partial x} \right) + \frac{\theta}{\rho c_p T} H_s \quad (4)$$

$$\frac{\partial q}{\partial t} = -u \frac{\partial q}{\partial x} - w \frac{\partial q}{\partial z} + \frac{\partial}{\partial x} \left(K_{WH} \frac{\partial q}{\partial x} \right) + E \quad (5)$$

$$\rho = \rho_0 (1 - \beta T') \quad (6)$$

$$\frac{\partial p}{\partial z} = -g\rho \quad (7)$$

where all terms are defined in the list of symbols (Appendix A).

The layer-averaged equations are derived from Eqs. (1) through (5) by integration over layer depth. The hydrostatic assumption is included in the pressure gradient term of the u-momentum equation. The pressure gradient term of the v-momentum equation is assumed to balance the specified geostrophic u-component. Since moisture is included only insofar as it produces density gradients and consequently pressure gradients, its effect on the flow field is parameterized by the inclusion of virtual potential temperature in the buoyancy expression of the pressure gradient term. Thus density is not a prognostic variable in the model, and density gradients are replaced by temperature gradients.

For computational economy a modification of Schulman's (1970) stretched coordinate system (to be discussed later) is used together with for computational economy a modification of Schulman's (1970) stretched coordinate system (to be discussed later) is used together with an explicit numerical scheme. The layer averaged equations, derived in Appendix B, are listed below.

The prognostic model equations with coordinate stretching are:

u-momentum

$$\begin{aligned}
 u_{kt} = & -\frac{1}{2} s' (u_k u_k)_s - \frac{gs'}{\rho_{0k}} \left[\epsilon_k^k \phi_s - \frac{1}{2} \rho_{0k} h_k \beta'_k \theta_{ks}' \right. \\
 & \left. - \left\{ \sum_{j=k+1}^n \left(\epsilon_k^j h_{js} + \rho_{0j} h_j \beta'_j \theta_{js}' \right) \right\} \right] + f v_k + \\
 & K_{MH} \left[s'' u_{ks} + (s')^2 u_{kss} \right] + \frac{1}{\rho_{0k} h_k} \left[\tau_T^x - \tau_B^x \right] \quad (8)
 \end{aligned}$$

v-momentum

$$\begin{aligned}
 v_{kt} = & -s' \left[(u_k v_k)_s - v_k u_{ks} \right] + f (u_g - u_k) + \\
 & K_{MH} \left[s'' v_{ks} + (s')^2 v_{kss} \right] + \frac{1}{\rho_{0k} h_k} \left[\tau_T^y - \tau_B^y \right] \quad (9)
 \end{aligned}$$

Mass continuity

$$h_{kt} = -s' (u_k h_k)_s \quad (10)$$

Heat

$$\begin{aligned}
 \theta_{kt} = & -s' (u_k \theta_k)_s - \frac{1}{h_k} \left[w_T \bar{\theta}_T - w_B \bar{\theta}_B \right] + K_{QH} \left[s'' \theta_{ks} + (s')^2 \theta_{kss} \right] \\
 & - \frac{1}{h_k} \left[(K_{QV} \theta_z)_B - (K_{QV} \theta_z)_T \right] - \frac{1}{h_1} \left[C_D |V|_1 (\Delta \theta)_B \right] \quad (11)
 \end{aligned}$$

Moisture

$$\begin{aligned}
 q_{kt} = & -s' (u_k q_k)_s - \frac{1}{h_k} \left[w_T \bar{q}_T - w_B \bar{q}_B \right] + K_{WH} \left[s'' q_{ks} + (s')^2 q_{kss} \right] \\
 & - \frac{1}{h_k} \left[(K_{WV} q_z)_B - (K_{WV} q_z)_T \right] - \frac{1}{h_1} \left[C_D |V|_1 (\Delta q)_B \right] \quad (12)
 \end{aligned}$$

The last terms on the RHS of (10) and (11) are included only for the surface layer.

The last terms on the RHS of (10) and (11) are included only for the surface layer. The Boussinesq equation of state, virtual potential temperature and diagnostic vertical motion equations are:

State

$$\rho = \rho_0 (1 - \beta' \theta') \quad (13)$$

Virtual potential temperature

$$\theta^* = \theta (1 + 0.61q) \quad (14)$$

Vertical motion

$$w_T = w_p - s' \sum_{j=1}^k h_j u_{js} \quad (15)$$

The explicit numerical scheme adopted for the model integrations consists of centered differences in time (leap-frog), Granneltvedt's (1969) scheme F conservative form for the advective terms, lagged in time for diffusion terms, and centered in space and time for all other terms. Using the notation in Granneltvedt (1969) and denoting the grid interval in stretched coordinates by Δ , the terms of the finite difference analogues to Eqs. (8) through (12) can be conveniently expressed through the following sum and difference operators:

$$a_s = \frac{1}{\Delta} \left[a(s_i + \Delta/2) - a(s_i - \Delta/2) \right]$$

$$\bar{a}^s = \frac{1}{2} \left[a(s_i + \Delta/2) + a(s_i - \Delta/2) \right]$$

$$\bar{a}^{2s} = \frac{1}{2} \left[a(s_i + \Delta) + a(s_i - \Delta) \right]$$

from which it can be shown by simple manipulation that derivatives may be expressed as

$$\frac{\partial a}{\partial x} \approx a_s$$

$$\frac{\partial a}{\partial x} \approx \frac{1}{\Delta} \left[\bar{a}^s - \bar{a}^{s-1} \right]$$

$$\frac{\partial}{\partial s} (ab) \approx \left(\bar{a}^s \bar{b}^s \right)_s$$

and

$$\frac{\partial^2 a}{\partial s^2} \approx \frac{2}{\Delta^2} \left[\bar{a}^{2s} - a^{(v-1)} \right]$$

where the superscript $(u-1)$ implies lagged in time. Suppressing the central time indicator (v) , the finite difference forms of (8) through (12) are

u-momentum

$$u_k^{v+1} = u_k^{v-1} + 2\Delta t \left[\begin{aligned} & - \frac{1}{2} s' \left[\bar{u}_k^s \bar{u}_k^s \right]_s \\ & - \frac{gs'}{\rho_{0k}} \left[\epsilon_k^k \bar{\phi}_s^s - \frac{1}{2} \rho_{0k} h_k \beta_k' \frac{\bar{\theta}_k^s}{k_s} \left\{ \sum_{j=k+1}^n \left[\epsilon_k^j \bar{h}_{js}^s \right. \right. \right. \right. \\ & \left. \left. \left. + \rho_{0j} h_j \beta_j' \frac{\bar{\theta}_j^s}{k_j} \right\} \right] \right] + fv + K_{MH} \left[s'' \bar{u}_k^s + 2 \left(\frac{s'}{\Delta} \right)^2 \left\{ \bar{u}_k^{2s} \right. \right. \\ & \left. \left. - u_k^{(u-1)} \right\} \right] + \frac{1}{\rho_{0k} h_k} \left[\tau_T^x - \tau_B^x \right]^{(u-1)} \end{aligned} \right]$$

v-momentum

$$v_k^{v+1} = v_k^{v-1} + 2\Delta t \left[\begin{aligned} & - s' \left[\left(\bar{u}_k^s \bar{v}_k^s \right)_s - v_k \bar{u}_{ks}^s \right] \\ & + f (u_g - u_k) \\ & + K_{MH} \left[s'' \bar{v}_{ks}^s + 2 \left(\frac{s'}{\Delta} \right)^2 \left\{ \bar{v}_k^{2s} - v_k^{(u-1)} \right\} \right] \\ & + \frac{1}{\rho_{0k} h_k} \left[\tau_T^y - \tau_B^y \right]^{(u-1)} \end{aligned} \right]$$

Heat and moisture

Using E to denote either θ or q

$$E_k^{v+1} = E_k^{v-1} + 2\Delta t \left[\begin{aligned} & - s' \left(\bar{u}_k^s \bar{E}_k^s \right)_s \\ & - \frac{1}{h_k} \left[w_T \bar{E}_T - w \bar{E}_B \right] \\ & + K_{QH} \left[s'' \bar{E}_{ks}^s + 2 \left(\frac{s'}{\Delta} \right)^2 \left\{ \bar{E}_k^{2s} - E_k^{(u-1)} \right\} \right] \\ & + K_{QH} \left[s'' \bar{E}_{ks}^s + 2 \left(\frac{s'}{\Delta} \right)^2 \left\{ \bar{E}_k^{2s} - E_k^{(u-1)} \right\} \right] \\ & - \frac{1}{h_k} \left[K_{QV} E_z \right]_B - \left[K_{QV} E_z \right]_T^{(u-1)} \\ & - \frac{1}{h_k} \left[C_D |V|_1 (\Delta E)_B \right]^{(u-1)} \end{aligned} \right]$$

Mass continuity

$$h_k^{v+1} = h_k^{v-1} - 2\Delta t \left[s' (\bar{u}_k^s \bar{h}_k^s)_s \right]$$

2.1 Initial conditions

(a) Momentum and mass fields

It is normally assumed that the initial conditions for boundary layer flow satisfy the Ekman balance, and initial conditions for the flow field are solved as a balance between pressure gradient, Coriolis, and stress terms in the steady state equations of motion. However, topography is not considered in models adopting this assumption, therefore it is not used in deriving the initial flow fields for this model.

In this study, so-called balanced initial conditions (hereafter referred to as the undisturbed state) are derived as steady state solutions to the momentum and continuity equations (the unforced problem) using guess fields from which to start the integrations. We thus treat the undisturbed state as the state resulting after adjustment due to an impulsive start of the model flow without heating or moisture.

Balance of forces computed from the undisturbed state over a flat island indicate that the Ekman balance is approximately satisfied. Over the real island the balance of forces is more complicated, with advection and sometimes horizontal friction playing major roles. In order to examine the influence of friction on the balance of forces, a steady state was generated over a water surface and the results compared with those for the flat island. Over the water surface the Ekman balance was even more closely satisfied. These results suggest that the assumption of Ekman balance as initial conditions is valid over uniform surfaces devoid

of both topography and drastic changes in surface drag coefficients.

In the above experiments surface drag coefficients varied from 1.5×10^{-3} over water to 1.0×10^{-2} over land. We therefore suggest that the assumption of Ekman balance in the boundary layer be avoided in models with topography and large changes in surface friction characteristics.

The undisturbed states derived by the above method also indicate that the velocity field adjusts to the mass field. Further, the undisturbed state is independent of shear in the guess field and depends only on the imposed geostrophic profile. An examination of the divergence of mass fluxes across the island computed as

$$\frac{\partial}{\partial x} (uh) \approx \frac{(uh)_2 - (uh)_1}{x_2 - x_1}$$

where subscripts 1, 2 refer to selected points on the island show that the steady state continuity equation is closely satisfied by the undisturbed condition. Fig. 2 shows the vertical profiles of the u-component of velocity over the coasts and crest of the island, and corresponding hodographs for the undisturbed state with an imposed geostrophic wind of 4 m sec^{-1} from the east. Since there is no shear in the geostrophic profile, frictional resistance at the ground imposes a westerly stress on the air causing a north-south Ekman drift to develop in response to the Coriolis acceleration, thus the northerly component in the undisturbed state. Note also the tendency for the u-components to become geostrophic in all layers except the lowest. Here the departure from geostrophy is most pronounced over the crest of the island. A counterpart experiment with linear shear in the geostrophic profile was conducted. The resulting undisturbed state showed all the characteristics

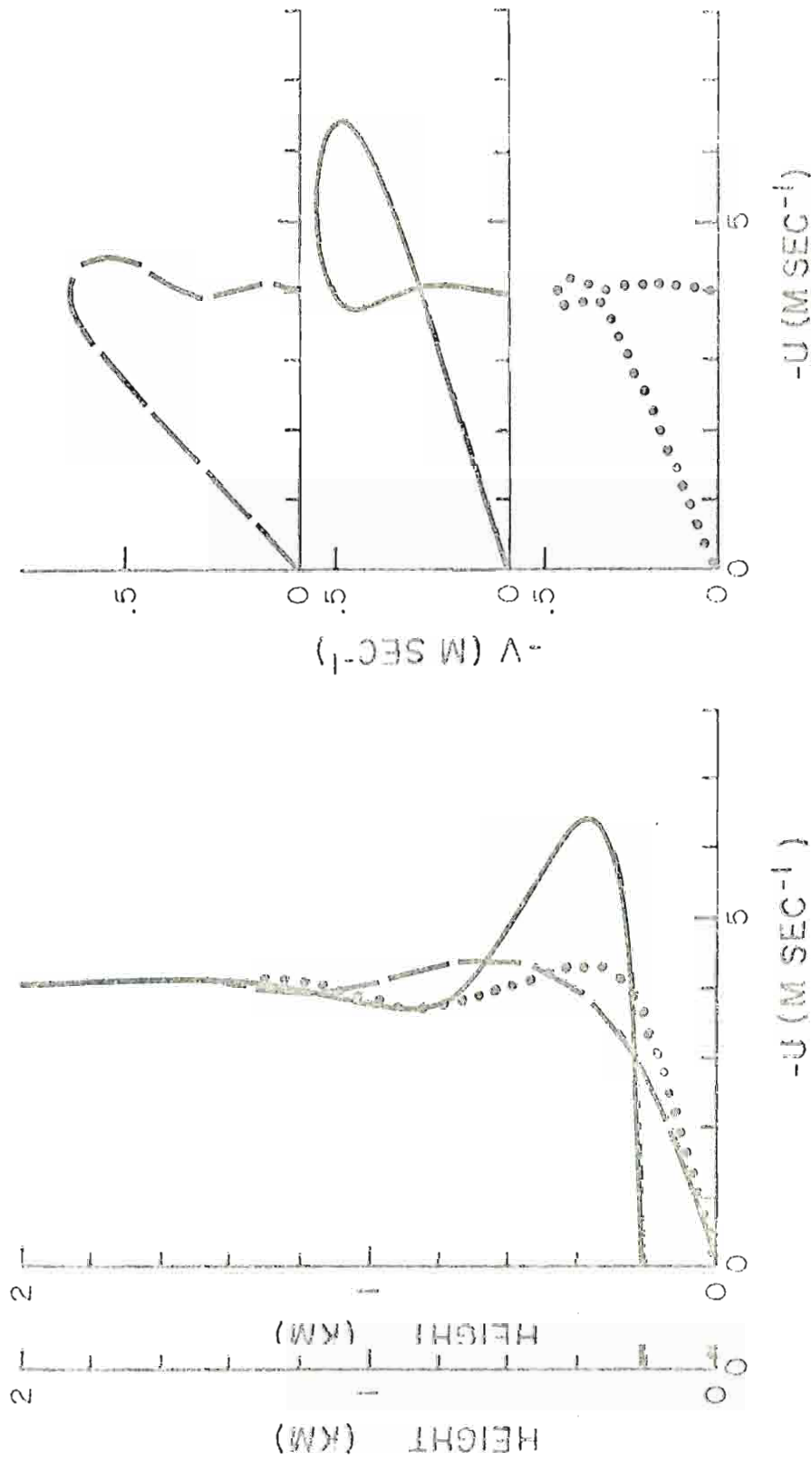


Fig. 2. fig. 2. Vertical profiles of the u-component, and hodographs for the undisturbed flow over the east coast (coast (dashed), west coast (dotted) and the hill crest (solid) of the real island with a specified easterly geostrophic wind of 4 m sec⁻¹.

described above except for the north-south Ekman drift. In this case a southerly component developed during the adjustment process because the surface frictional effect was absent and the Coriolis effect on the imposed easterly flow resulted in a south-north component. In all experiments used in this study a uniform geostrophic profile is imposed for consistency with the imposed spatially uniform initial temperature field.

The adjustment process is illustrated in Fig. 3, which shows the time variation of the wind in the lowest layer over the crest of the island from two imposed guess fields to the adjusted undisturbed states. In both cases the flow is impulsively started over the island. The inertial oscillation is clearly visible during the adjustment process.

(b) Temperature and moisture fields

Initial conditions for temperature and moisture are idealized profiles approximated from mean July and August, 1969 radiosonde data for Seawell, Barbados and from the ship DISCOVERER which was stationed some 60 km east of the island. The soundings show a shallow layer (~150 m deep) immediately above the surface with a weak super-adiabatic lapse rate, a neutral layer above to approximately 1 km, and a deep slightly stable layer above. Thus, neutral temperature stratification is conveniently chosen as the initial condition for the model cases to be discussed later. Provision is made in the computer program to accommodate other temperature stratifications, however no experiments with these changes are conducted for the purposes of this study.

The soundings also show that, except for a very shallow layer of these changes are conducted for the purposes of this study.

The soundings also show that, except for a very shallow layer of almost constant humidity mixing ratio immediately above the surface, the mixing ratio decreases almost linearly with height up to heights in

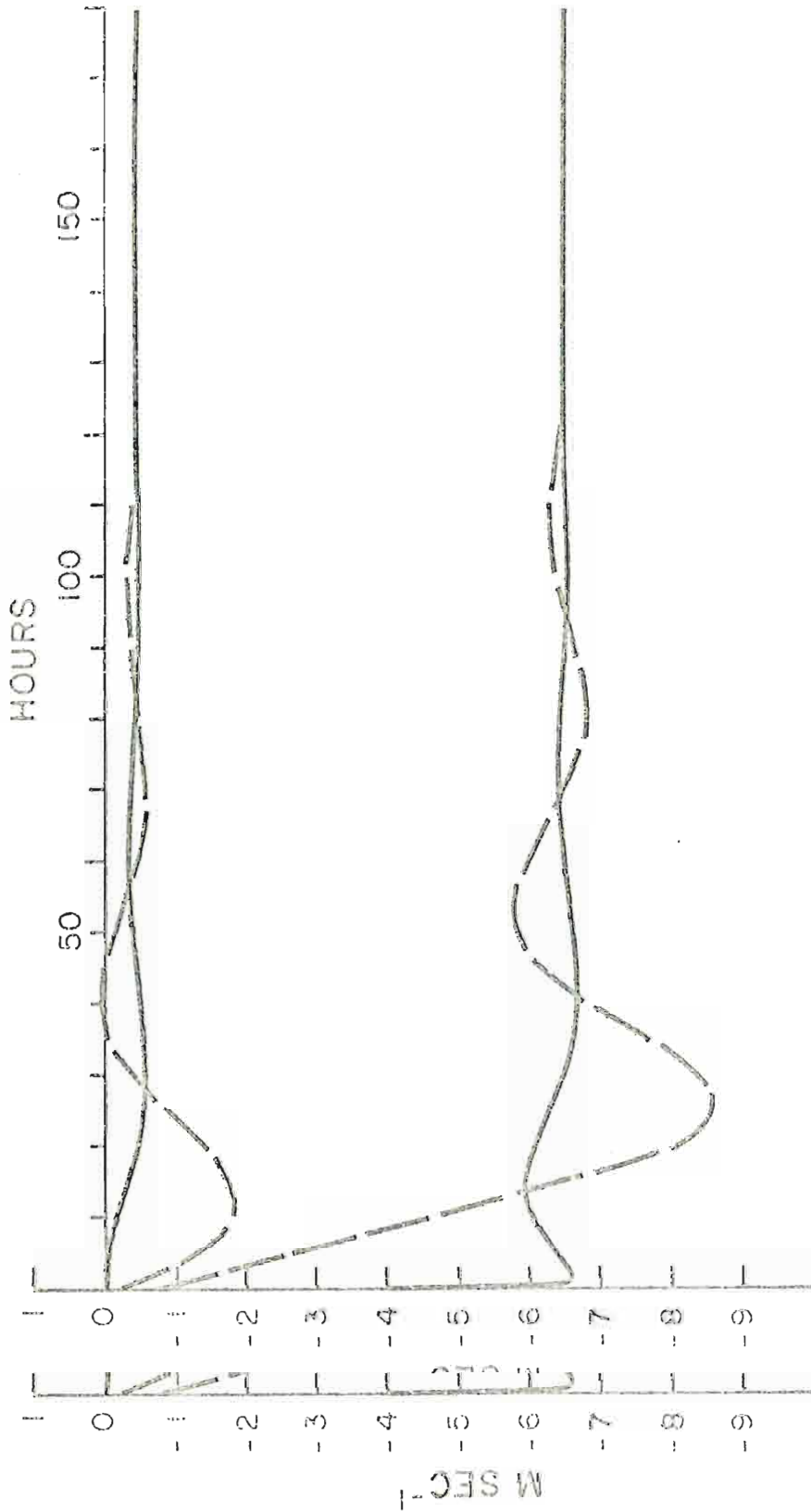


Fig. 3. ig. 3. Adjustment of the u (lower) and v (upper) components from initial guess fields in the lowest layer over the crest of the island. Easterly geostrophic wind is 4 m sec^{-1} . Solid curves are for a uniform shear profile of 4 m sec^{-1} . Dashed curves are for a linear shear guess profile with an upper value of 4 m sec^{-1} .

excess of 2 km, thus a linear profile of humidity mixing ratio is adopted as the initial condition for moisture.

Mean layer densities are computed from an idealized linear density profile suggested by the radiosonde data. The above linear profiles are defined in terms of surface values taken from the radiosonde data and upper-level values approximated from those at the assumed mean level of the inert layer. The sea surface value for humidity mixing ratio is the saturation value corresponding to the assigned sea surface temperature which is held constant in time.

2.2 Boundary conditions

Due to the limited model region, boundary conditions are required on all boundaries.

(a) Upper boundaries

Horizontal velocity components, temperature, humidity mixing ratio, density and pressure are specified and held fixed in time. The upper boundary condition on pressure enters only indirectly in the computation of the buoyancy part of the pressure gradient term in the u-momentum equation. Pressure is not a predicted variable in this model. The upper condition on density appears in the reduced gravity part of the pressure gradient term in the u-momentum equation. Temperature and humidity mixing ratio, assigned as mean values in the inert layer are held constant in time on the assumption that sensible heat and moisture fluxes into the inert layer from below have little effect on the initial conditions within this layer. We note that latent heat release is not into the inert layer from below have little effect on the initial conditions within this layer. We note that latent heat release is not included in the model. An easterly geostrophic flow, independent of time, is imposed as an upper boundary condition on the flow field.

Thus we assume

$$u_{\text{TOP}} = u_g = -\frac{1}{\rho f} \frac{\partial p}{\partial y}$$

$$v_{\text{TOP}} = 0$$

which implies a fixed north-south slope to the interface between the active and inert layers.

(b) Lower boundaries

Since the aim of the study is to obtain an explanation for an observed anomaly in the low-level flow over the island (in response to surface conditions), the model is forced by the surface boundary conditions on temperature and moisture. The surface condition on moisture is prescribed from an idealized surface value of humidity mixing ratio obtained from radiosonde data. Over oceanic areas, the surface value of the humidity mixing ratio is prescribed as the saturation value corresponding to the sea surface temperature which is held fixed in time.

The surface temperature on the island is prescribed in terms of a time and space-dependent function representing land-sea temperature differences. The spatial dependence is assumed to be sinusoidal with maximum amplitude in the middle of the island and decreasing to zero amplitude at a distance of 1 km off shore. The choice of a smooth variation at coastal regions instead of a sudden change in heating between sea and land helps to suppress the development of $2\Delta x$ temperature waves which form as a result of the centered differencing scheme used for the advective terms (see Fisher, 1961). The suppression of $2\Delta x$ temperature waves which form in this manner is very important to used for the advective terms (see Fisher, 1961). The suppression of $2\Delta x$ temperature waves which form in this manner is very important to the success of the model since growing $2\Delta x$ oscillations in the height field develop in response to the temperature waves leading eventually

to computational instability and explosive destruction of the solutions. This problem is bypassed in models using an upstream differencing scheme because of its inherent viscosity.

The time variation of the surface temperature is specified as a truncated Fourier representation of land-sea temperature differences derived by Holley (1972) from radiometer data collected over Barbados in 1969 during the BOMEX experiment.

The surface boundary condition on temperature over land may be represented in the form

$$T(x,t) = T(t) \left[1 + \cos \frac{2\pi}{R} (x - x_0) \right]$$

where

$$T(t) = a_0 + \sum_{n=1}^4 \left(a_n \cos \frac{2\pi n t}{N} + b_n \sin \frac{2\pi n t}{N} \right)$$

a_0 is the 24-hour mean land-sea temperature difference;

N is one day;

R is the horizontal distance over which heating is applied;

x_0 is the distance of the center of the island from the west boundary;

x is the distance from the west boundary of points lying within $R/2$ of x_0 .

The function $T(t)$ is shown in Fig. 4, and the coefficients a_n and b_n are given in Table 1.

Table 1. Coefficients a_n , b_n of the function $T(t)$

n	a_n	b_n
0	2.85	
1	-5.28	-0.92
0	2.85	
1	-5.28	-0.92
2	1.85	0.30
3	0.22	-0.35
4	-0.22	0.18

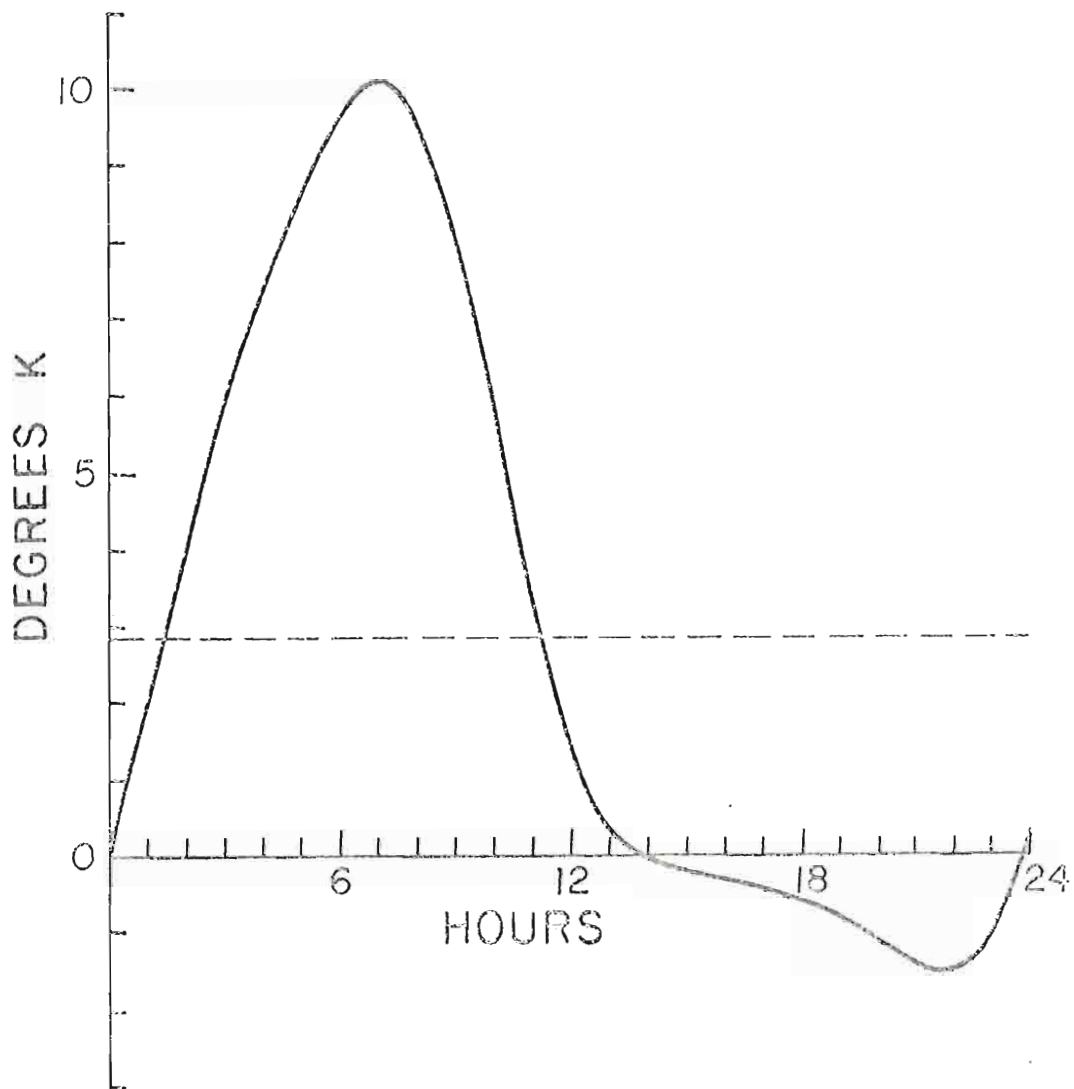


Fig. 4. Amplitude of the time dependent land-sea surface temperature difference, $T(t)$, at the center of the island. The initial time corresponds to 0600 LST. The dashed line is the 24 hr. mean.

... .., $T(t)$, at the center of the island. The initial time corresponds to 0600 LST. The dashed line is the 24 hr. mean.

(c) Lateral boundaries

Cyclic boundary conditions are assigned to the lateral boundaries to ensure mass conservation within the model region. This, however, introduces the problem that the model now represents a series of islands separated by the width of the model region, and the solutions upwind of and over the island may, in time, be affected by downstream propagation of island generated disturbances. This problem can be minimized by increasing the width of the model region so that the boundaries are far enough away from the island to allow propagating disturbances to be sufficiently damped before reaching the boundaries, thus suppressing their effects and allowing the interior solutions to be representative of flow over a single island. In order to retain a limited number of grid points within a sufficiently wide model region, and to maintain relatively high resolution (small grid interval) over and in the immediate vicinity of the island, a stretched coordinate system (after Schulman, 1970) is adopted. This system will be discussed later.

Since internal gravity waves are the fastest moving disturbances generated in the model, and are most likely to propagate through the boundaries both up and downstream, experiments were conducted to examine their effect on the interior solutions both in a limited width model using a regular grid, and in an extended width model using stretched coordinates. Model depth for these experiments was 1 km. In the case of the limited width model, the model width was 120 km with a grid interval of 2 km, and gravity waves were generated either by disturbing of the limited width model, the model width was 120 km with a grid interval of 2 km, and gravity waves were generated either by disturbing an interface between layers in a static field over a flat surface, or by impulsively starting a flow over topography. All solutions with

this model blew up after 1 or 2 hours of integration. At the time of conducting these experiments, results had already been obtained from the 1 km deep model with stretch coordinates for the case of dry flow over topography with and without heating for periods of up to 4 days with no sign of instability, therefore specific experiments on gravity waves only were not conducted. It was concluded from the available results that gravity waves were not detrimental to the solutions in the case of the extended width model using stretch coordinates and that the interior solutions were not affected by gravity waves propagating through the boundaries.

The question of the effect of the stretch coordinates on the gravity waves will be considered later. It is still necessary to investigate the effect of the boundary positions on the interior solutions since phenomena other than gravity waves propagating through the boundaries could be affecting the interior solutions. This is accomplished by varying the model width and comparing the interior solutions. It was found that for model widths in excess of 600 km the differences in the interior solutions were negligible when compared with differences in solutions from smaller model widths. Tests were conducted with 60, 180, and 300 km wide regular grid models, and with 300, 600, and 1000 km stretched grid models. The 300 km test also showed that the results from both regular and stretched grids were in agreement. The number of grid points was kept constant for tests with the 600 and 1000 km stretched grid models. Thus, the tests also served the purpose of of grid points was kept constant for tests with the 600 and 1000 km stretched grid models. Thus, the tests also served the purpose of examining the effect of grid resolution on model solutions. Tests on the effect of grid resolution were also made with the 600 km wide model

by varying the number of grid points. It was found that this effect was also negligible. Thus, all further experiments in this study are made with a 600 km wide model utilizing 65 grid points inclusive of boundary points. Minimum grid distance is 1 km near the center, with a maximum of 47 km at the boundaries. There are 23 grid points over the island which is 24 km wide, and a total of 49 grid points over a distance of 80 km centered at the center of the model region. This configuration gives rather high resolution over and in the immediate vicinity of the island, and lower resolution towards the boundaries.

2.3 Model depth

Comparisons between 1 and 2 km deep models were made by generating the dry thermally driven flow over real topography. The strength of the mean layer velocities decreased in the 2 km model relative to that in the 1 km model due to the greater layer depths. Vertical profiles of the u-components over selected points of the island derived from the mean layer velocities in each case showed that the low-level inflow occurred at a greater height in the 2 km model than in the 1 km model, again, because of the greater layer depths in the former, but that the height at which the maximum in the return flow aloft occurred remained approximately the same in both cases. A possible explanation for this result is that the vertical profile of the vertical diffusion coefficient for momentum is the same below 1 km for both models and remains constant above 1 km in the deeper model. The major difference between the velocity profiles occurs at the top of the models where, in order to satisfy above 1 km in the deeper model. The major difference between the velocity profiles occurs at the top of the models where, in order to satisfy the fixed boundary conditions, unrealistically steep gradients result in the shallower model. More specifically, in the 2 km model the

vertical gradient of horizontal velocity at the upper boundary is approximately zero. Similar observations are made of the vertical profiles of the potential temperature fields in the two models. As a consequence of these results the model depth for the experiments in this study is chosen to be 2 km. It should be noted that this depth is not fixed in time because a rigid lid is not imposed at the top, i.e., $w = 0$ is not assumed, however the vertical variations in the upper boundary remain small in time because of the fixed conditions on pressure and density.

2.4 Stretch coordinates

The stretch coordinate system used in this model is adapted from Schulman (1970). For this study stretching is applied symmetrically about the center of, and continuously across the model region. The stretching function is defined as

$$s(x) = c \left[ax + \tanh \left(\frac{x - x_0}{\sigma} \right) + b \right]$$

where b and c are chosen such that

$$s(0) = 0 \quad \text{and} \quad s(1) = 1.$$

x is measured from the west boundary of the grid and is normalized by the model width, i.e.,

$$0 \leq x \leq 1$$

x_0 is the normalized position of the center of the model region, thus

$$x_0 = 0.5$$

σ ($= 0.044$) is a stretching scale factor. The value of σ was found empirically to suit the model.

σ ($= 0.044$) is a stretching scale factor. The value of σ was found empirically to suit the model.

$$a = 0.5$$

$$b = \tanh \frac{x_0}{\sigma}$$

and

$$c = \left[a + b + \tanh \left(\frac{1 - x_0}{\sigma} \right) \right]^{-1}$$

The first and second derivatives in x are given by

$$\frac{\partial}{\partial x} = s' \frac{\partial}{\partial s} \quad \text{and} \quad \frac{\partial^2}{\partial x^2} = s'' \frac{\partial}{\partial s} + (s')^2 \frac{\partial^2}{\partial s^2}$$

where

$$s'(x) = \frac{ds}{dx}.$$

Experiments with this coordinate system showed that gravity waves had apparently no adverse effects on the solutions in a 600 km wide model over a period of 4 days, while in a limited width model with regular grid gravity waves quickly destroyed the solutions. It is suggested that gravity waves are effectively suppressed by the stretched coordinates in this model because the grid distances in the outer region near the boundaries exceed the wavelength of these disturbances generated by the model and that the system also introduces computational smoothing through the extra term arising from the finite difference form of the horizontal diffusion term in the equations. For the u -momentum equation this term takes the form

$$K_{MH} \left[s'' \frac{\partial u}{\partial s} + (s')^2 \frac{\partial^2 u}{\partial s^2} \right]$$

The additional smoothing referred to above is provided by the expression $s'' \frac{\partial u}{\partial s}$. The ratio

$$\left[s'' \frac{\partial u}{\partial s} / (s')^2 \frac{\partial^2 u}{\partial s^2} \right]$$

$$\left[s'' \frac{\partial u}{\partial s} / (s')^2 \frac{\partial^2 u}{\partial s^2} \right]$$

increases outward from the center of the model region to a maximum value of 0(1) in the region where the grid interval is approximately twice the

length of the gravity wave. It is surmised that the combined effects of this extra smoothing and loss of resolution are responsible for suppressing the gravity waves.

2.5 Experiments and model parameters

The results of four case studies comprise the basis of the present investigation. The main characteristics of these cases (A - D) are listed in Table 2, together with the characteristics of comparative case studies (E - L) used to establish the effect of variations in physical properties of the model. Physical constants in the model are listed in Table 3.

The diffusion coefficients for momentum, heat, and moisture are assumed to be equal, however the horizontal coefficient is not the same as the vertical coefficient. The vertical diffusion coefficients are defined in the manner suggested by O'Brien (1970). The value of the coefficient and its vertical derivative at the top of the Prandtl layer (50 m) are approximated from wind data obtained from the 16 m towers on Barbados (LaSeur and Clary, 1973, personal communication) on the assumption that the log-linear profile is valid within this depth.

Thus we have

$$k = ku^*z$$

and

$$\frac{\partial k}{\partial z} = ku^*$$

where k is von Karman's constant (≈ 0.4);

u^* is the friction velocity (taken as 0.4 m sec^{-1} from the Barbados data);

u^* is the friction velocity (taken as 0.4 m sec^{-1} from the Barbados data); and

z is the depth of the Prandtl layer (assumed = 50 m).

Table 2. List of hypothetical case studies. u_g is the specified geostrophic wind

Case	u_g (m sec ⁻¹)	Topography	Remarks
A	0	sinusoidal	Cases A-G forced by space-time dependent land-sea surface temperature difference, and moisture profiles discussed in Section 2.1(b)
B	0	real	
C	-4	flat	
D	-4	real	
E	-2	real	
F	-6	real	
G	-8	real	
H	-4	real	Dry ⁽¹⁾
I	-4	real	Surface humidity mixing ratio constant in x, and equal to value on land.
J	-4	flat	Land-sea surface temperature difference constant in space and time.
K	-4	real	Land-sea surface temperature difference constant in space and time.

(1) Remarks in cases H-K indicate deviations from forcing applied to cases A-G.

(1) Remarks in cases H-K indicate deviations from forcing applied to cases A-G.

Table 3. Values of parameters and variables

C_D (over land)	1.0×10^{-2}	
C_D (over water)	1.5×10^{-3}	
K_{MH}, K_{QH}, K_{WH}	$10^3 \text{ m}^2 \text{ sec}^{-1}$	$(u_g = 0)$
	$10^3 \times u_g \text{ m}^2 \text{ sec}^{-1}$	$(u_g \neq 0)$
q_l	17 gm kg^{-1}	
q_s	23 gm kg^{-1}	(except in Case I)
q_{TOP}	7 gm kg^{-1}	
θ_s	300 K	
θ_{TOP}	300 K	
ρ_s	1.16 kg m^{-3}	
ρ_I	0.80 kg m^{-1}	
f	$3.15 \times 10^{-5} \text{ sec}^{-1}$	
g	9.8 m sec^{-2}	
Δt	15 sec	$(u_g = 0)$
	10 sec	$(u_g \neq 0)$
Δx	1 km	(minimum)
	47 km	(maximum)
β	10^{-2} K^{-1}	
κ	0.286	

Therefore, at the top of the Prandtl layer we assume

$$K = 8 \text{ m}^2 \text{ sec}^{-1} \quad \text{and} \quad \frac{\partial K}{\partial z} = 0.16 \text{ m sec}^{-1}.$$

The vertical diffusion coefficient is assumed to be $10 \text{ m}^2 \text{ sec}^{-1}$ at and above 1 km with zero vertical slope at 1 km. The values of the vertical diffusion coefficient at all levels within the model region are computed at each grid point and each time step from the profile defined above. Schematics of the profile over water and over the crest of the island conforming to the above specifications are shown in Fig. 5. No experiments are conducted to examine the effect of varying the structure of the vertical diffusion coefficient profile.

Model integrations are made over a minimum of 24 hr and a maximum of 10 1/2 days. The 24-hr integrations are carried out to examine the thermally generated circulations in an initially static state. When a mean flow is specified, the model is integrated without heating and moisture for 7 1/2 days to obtain a steady state which is used as the initial undisturbed condition. Heating, with or without moisture, is then applied for 24 to 72 hrs. An oscillatory steady state is observed in the flow fields, and even after a total of 10 1/2 days of integration there is no sign of destructive instability in the model results.

It is of interest to note that Neumann and Mahrer (1972) have integrated a modified version of Estoque's (1961) sea-breeze model (flat island) over three daily heating cycles from a state of rest with similar results.

similar results.

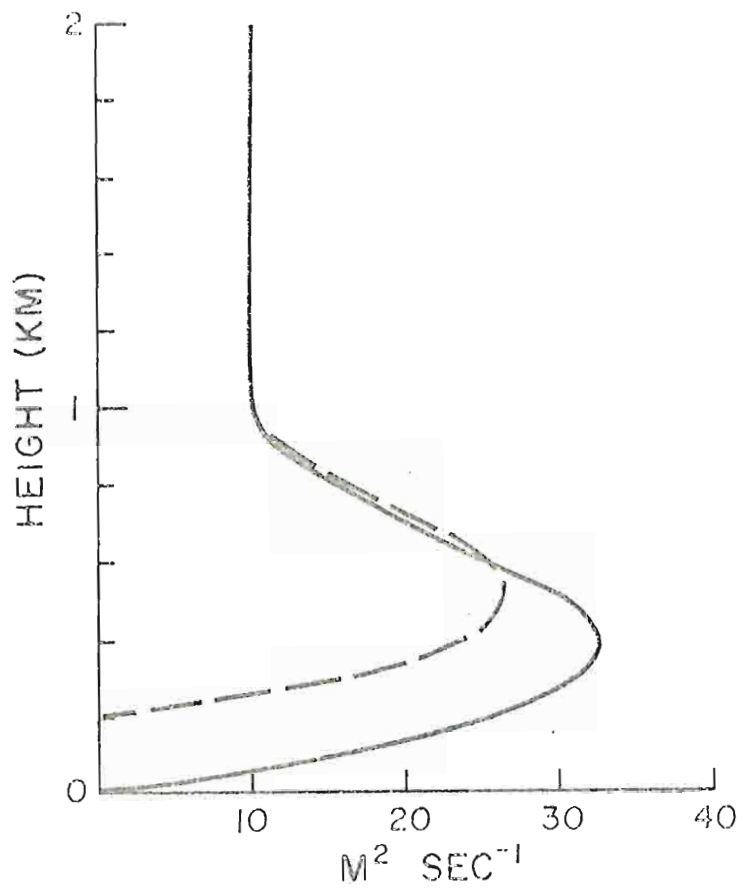


Fig. 5. Vertical profiles of the vertical diffusion coefficient over water (solid) and over the crest of the island (dashed)

CHAPTER III

RESULTS

Although our goal is to find physical explanations for the anomalous flow over Barbados under synoptically unsaturated, quasi-nondivergent conditions, it is useful to consider the model results without reference to observations in order to understand the characteristics of the model. The results are presented in part as vertical profiles of zonal velocity components and hodographs of the flow field over the coasts and the crest of the island. In the flat island case which provides a reference for determining topographic effects, the grid point corresponding to the position of the crest of the island is used as the inland point. These points will subsequently be referred to as the reference points. In addition, the spatial distribution of the perturbations generated in response to surface forcing is shown and discussed in terms of perturbation streamfunctions which are derived as differences between the streamfunctions for the forced flow and the unforced or undisturbed flow, i.e.,

$$\psi'(t) = \psi(t) - \psi(0)$$

where $\psi(t)$ and $\psi(0)$ are calculated from the total motion fields using the technique described by McNider and O'Brien (1973). The streamfunctions are displayed in stretched coordinates to emphasize the details over the island. For a general discussion of the model characteristics the are displayed in stretched coordinates to emphasize the details over the island. For a general discussion of the model characteristics the results of four case studies are presented. The forcing in the four

cases consist of time and space-dependent surface heating, and moisture profiles as described in Section 2.1(b). The forcing due to moisture included in this manner is constant in time at the surface.

The four cases examine the following phenomena:

- A. The moist symmetric double seabreeze circulation generated from an initial state of rest over sinusoidal topography.
- B. The moist double seabreeze circulation generated from an initial state of rest over the real island.
- C. The effect of surface heating on an easterly flow in a moist atmosphere over a flat island; and
- D. The combined effects of surface heating and the real island on an easterly flow in a moist atmosphere. The strength of the imposed easterly geostrophic flow is 4 m sec^{-1} in both Cases B and C.

We use the term real island to denote smooth topography approximated from topographic maps of Barbados for the widest east-west cross section of the island. This section corresponds to the east-west line along which three 16-m observational towers were sited during the field experiments.

Ideally we should have considered the thermal flow over a flat island in Case C as a standard of reference, however, due to loss of resolution, the thermal flow generated in the 2-km deep model with equal initial layer depths over a flat island was so weak that it was essentially indistinguishable from computational noise. This problem could have been rectified by using thinner lower layers, however, direct comparisons
 been rectified by using thinner lower layers, however, direct comparisons of the intensities of the resulting flow fields from the cases with topography would have been misleading since a relatively thick lower layer is

necessary to accommodate the topography. The problem of the intersection of an interface with the topography has not yet been solved for this model. Thus, the model is restricted only to shallow topographic profiles as is the case for the idealized cross section of Barbados chosen in this study. The crest of the island in this model is 204 m high.

An alternative to the thermal flow over a flat island is provided by Case A, the double seabreeze over sinusoidal topography. The sinusoidal hill allows the generation of a thermal circulation because of the thinner low-layer depth above its crest which is 200 m high at the center of the grid, and provides for symmetry in the flow field as would be obtained with a flat island. Model integrations are made over a 24-hr period (1 heating cycle) in each of Cases A, B, and C, and for 48-hr (2 heating cycles) for Case D. Integrations are initiated at 0600 LST and we associate the intensity of the perturbation circulations with the maxima in the u-component of velocity, which usually occur in the lowest model layer.

3.1 Case A: Sinusoidal topography, $\underline{u}_g = 0$

Hourly output of the streamfunction patterns show that the thermally generated circulation over sinusoidal topography is symmetric at all times during the heating cycle. The maxima in the u-component of velocity (Fig. 6) show that the symmetric seabreeze intensifies to a maximum near noon then decays to a minimum between 1600 and 1700 LST when the land breeze develops. The land breeze attains its maximum between 1900 and 2000 LST after which it decays gradually during the night with a secondary maximum develops. The land breeze attains its maximum between 1900 and 2000 LST after which it decays gradually during the night with a secondary maximum occurring at the time of minimum surface temperature (0400 LST). Note from Fig. 4 that the surface temperature has a maximum at approximately

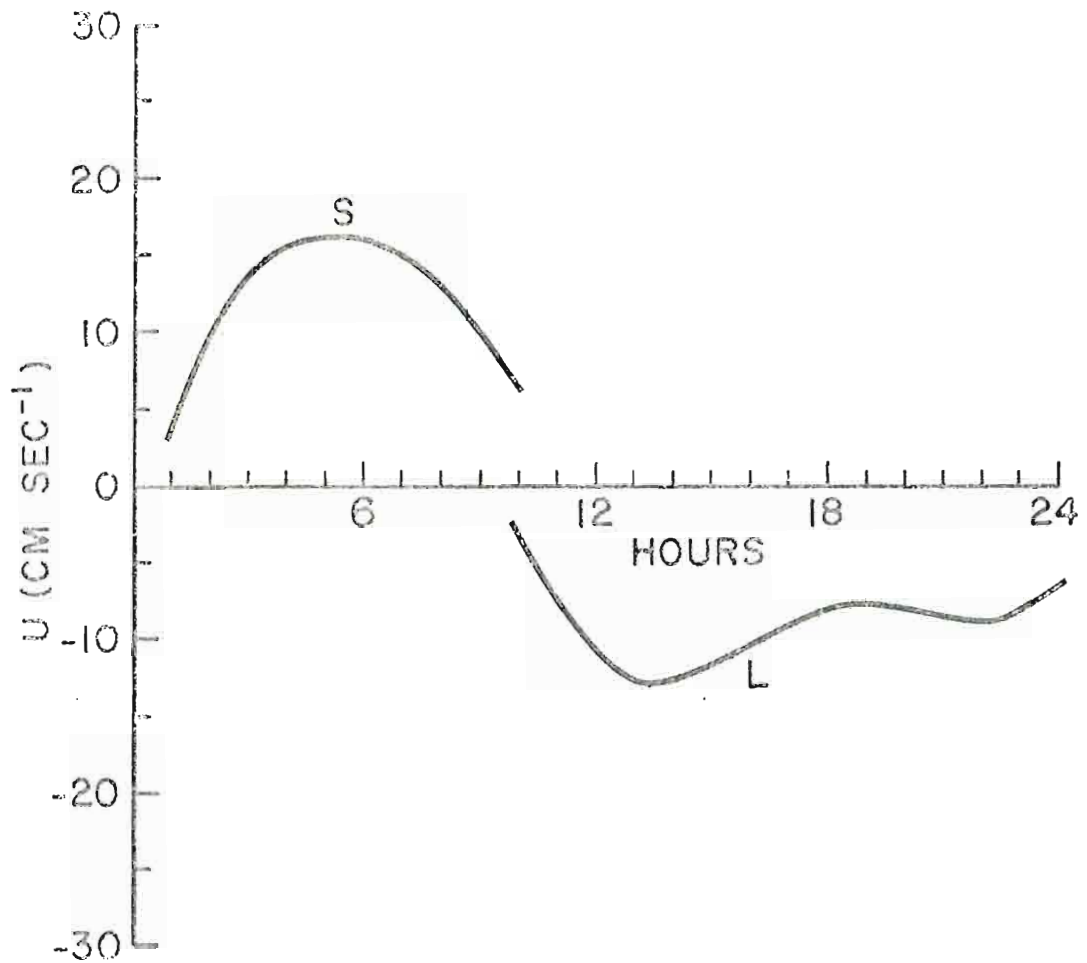


Fig. 6. Time variation of the maxima in the u-component of the symmetric sea (S) and land (L) breeze circulations (Case A). The initial time corresponds to 0600 LST.

1300 LST and a minimum at approximately 0400 LST with zeros at 0600 and 2000 LST. Fig. 7 shows the perturbation streamfunctions at 1300 and 0400 LST. By the end of the heating cycle the land breeze is rather weak and it will be seen under Case D that the seabreeze redevelops in response to the resumption of heating.

Upward vertical motions associated with the seabreeze attain a maximum in excess of 1 cm sec^{-1} by 1000 LST and sinking motions during the land breeze reach a maximum just less than 1 cm sec^{-1} by 1900 LST at the top of the lowest layer over the crest of the island. The region of vertical motion over the island, which is always symmetrically placed relative to the topography, expands continuously in time. Initially, for both sea and land breeze circulations, the region is approximately 12 km wide (or about half the width of the island) with its edges about 6 km inland of each coast. It is observed that the maxima in the lowest layer u-component are closely associated with the edges of this region of vertical motions and also move away from the island in time. Fig. 8 shows the propagation away from the island of the maxima in the u-component of the western cell of the symmetric circulation for both the sea and land breeze. The diagram is symmetric about the time axis. Thus, the model indicates that in the symmetric thermal circulation over a small island with sinusoidal topography, the maxima in both the land and sea breeze develop approximately midway between the crest and coasts and propagate seaward in time. An explanation for this phenomenon will be given in the discussion of the asymmetric seabreeze (Case B). Figs. 6 and 8 together show that at the time of maximum intensity, the maximum in the u-component in both the land and sea breeze is located offshore. Further, Fig. 8 indicates accelerated

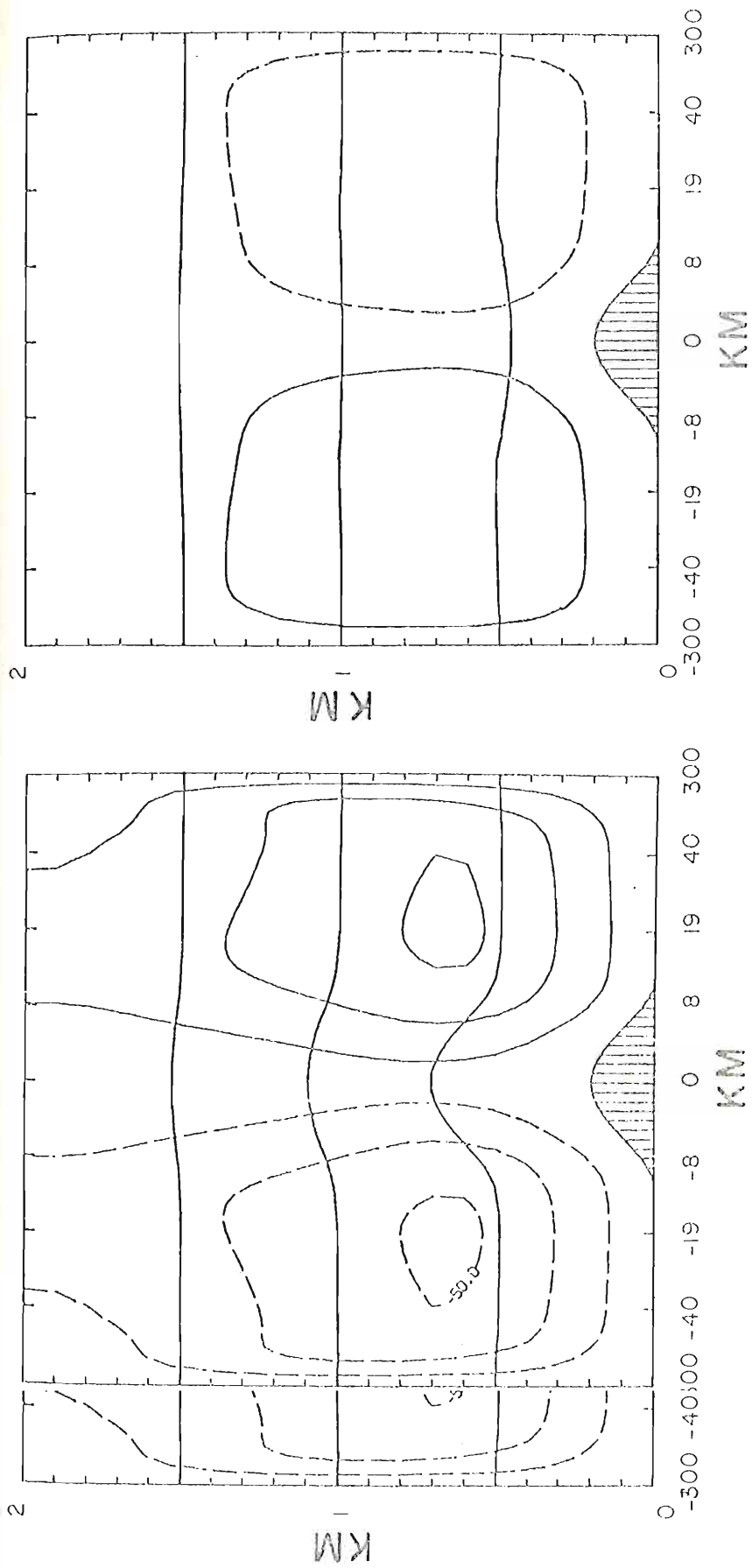


Fig. 7. P_0 Perturbation stream functions for Case A at 1300 LST (left) and 0400 LST (right), the times of maximum and minimum surface temperature respectively. Contour interval is $40 \text{ m}^2 \text{ sec}^{-1}$.

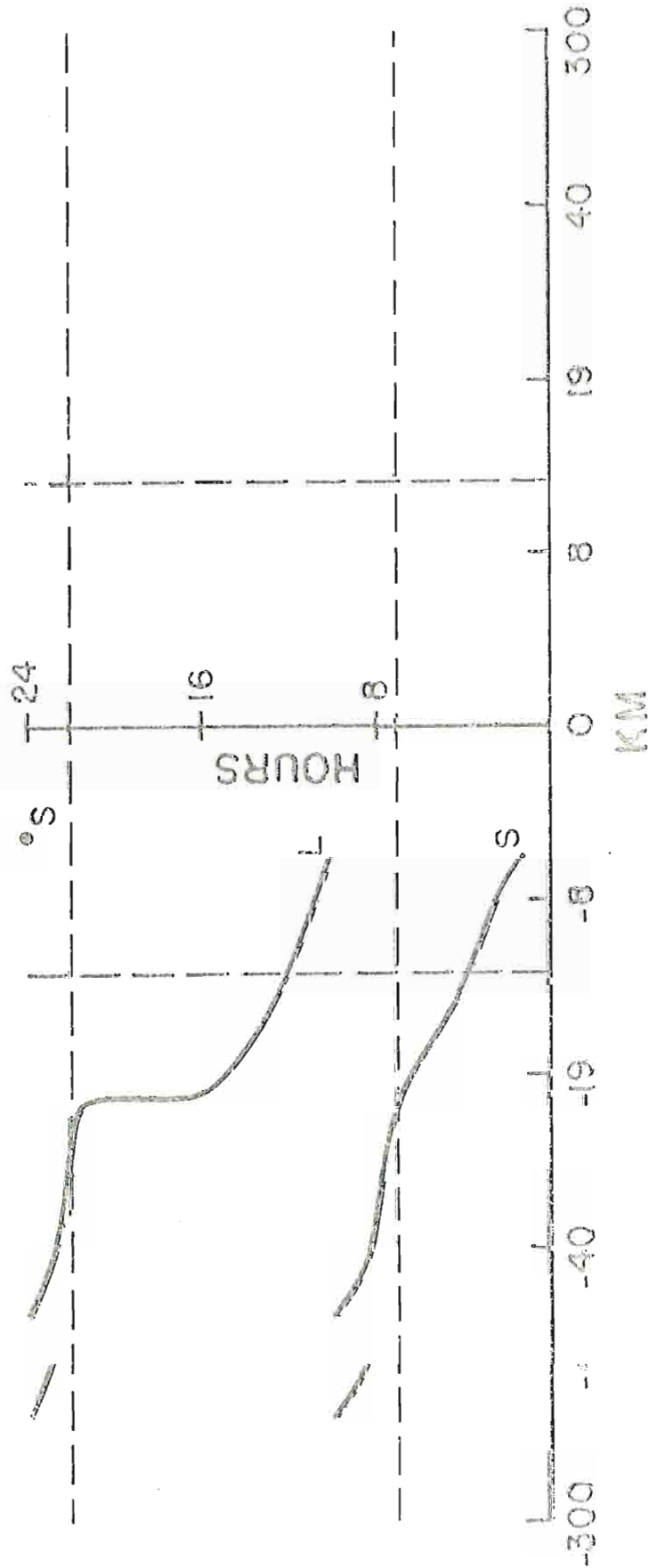


Fig. 8. Schem. Schematic of the propagation of the sea breeze (Case A). The point S at 24 hr. indicates resumption of the sea breeze. The dashed vertical lines indicate the coasts, and the dashed horizontal lines indicate the times of maximum (lower) and minimum (upper) surface temperature respectively.

propagation away from the island after the times of maximum and minimum surface temperature. This acceleration is also observed in the hourly streamfunctions (not shown).

3.2 Case B: Real island, $u_g = 0$

This case differs from the previous case only in the shape of the topography, therefore all differences between the results can be attributed to the geometry of the topography. The streamfunction patterns indicate that an asymmetric double seabreeze develops in response to heating with a more intense circulation on the east of the island than on the west. The eastern cell is also more intense than that in the symmetric case. Fig. 9 shows the relative intensities of the east and west circulations. The broken S-line represents the time variation of the maxima in the eastern seabreeze circulation, and the solid S-curve shows the same for the western cell. Comparison of the broken S-curve with the S-curve in Fig. 6 shows the relative intensities of the eastern cells between the asymmetric and symmetric circulations. Fig. 9 shows further that the western cell of the asymmetric seabreeze intensifies to a maximum between 0900 and 1000 LST, while the eastern cell attains its maximum between noon and 1300 LST. The land breeze (L-curves) develops between 1600 and 1700 LST, attaining a maximum on the west of the island between 1800 and 2000 LST (solid L-curve). On the east of the island the maxima in the land breeze circulation occur in the second layer rather than in the lowest layer between 1700 and 0100 LST, after which the maxima occur in the lowest layer. The land breeze attains its maximum intensity on the west rather than in the lowest layer between 1700 and 0100 LST, after which the maxima occur in the lowest layer. The land breeze attains its maximum intensity on the east at approximately 1900 LST with a secondary maximum occurring at approximately the time of minimum surface temperature

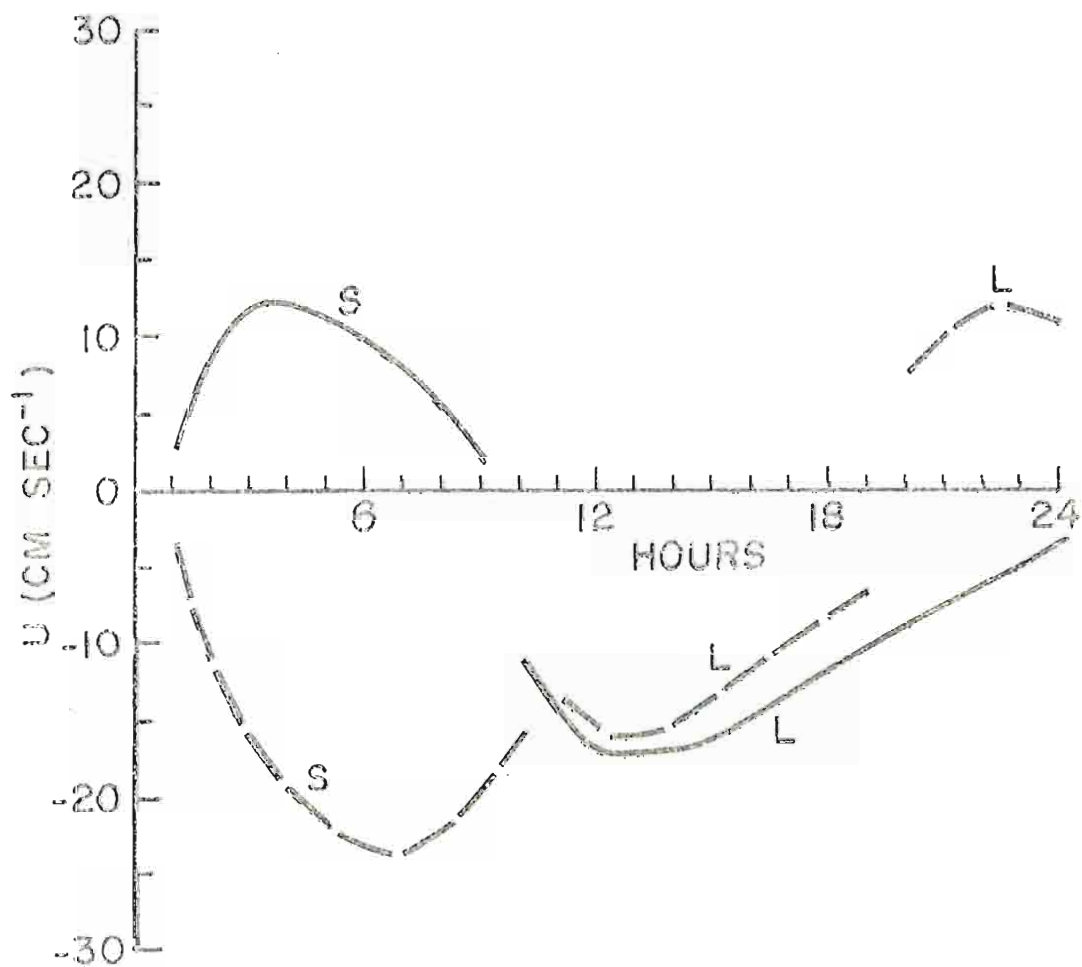


Fig. 9. Same as Fig. 6 but for Case B.

(0400 LST). This is demonstrated by the two sections of the broken L-curve in Fig. 9.

The hourly streamfunctions show that by 1800 LST a closed circulation in the land breeze has formed near the east coast below the 1 km level while a closed circulation on the west has formed far downstream and above the 1 km level. The eastern cell expands eastward and downward in time. The western cell of the land breeze disappears after the time of minimum surface temperature just as the western cell of the seabreeze does after the time of maximum surface temperature. Fig. 10 shows the perturbation streamfunctions for the times of maximum and minimum surface temperature.

We note that in both the symmetric (Case A) and asymmetric (Case B) circulations, the surface forcing functions and all other features are identical. In particular, the surface heating is symmetrically distributed in space about the center of the island, therefore the asymmetries and variations in intensities in Case B relative to Case A can be attributed to the difference in the slopes of the topography on the east and west sides of the island. A Fourier decomposition of the real topography shows that 95 per cent of the variance is accounted for by the first harmonic, 2 per cent each by the second and third, and 1 per cent by the fourth harmonic. Thus, we find that small deviations from symmetry in the geometry of the topography are responsible for noticeable changes in the resulting flow, indicating that we may expect topography to play an important role in the modification of the low-level flow over islands. ~~the resulting flow, indicating that we may expect topography to play an~~ important role in the modification of the low-level flow over islands.

Upward vertical motions in the seabreeze circulation attain a maximum in excess of 1 cm sec^{-1} over the island at the top of the lowest

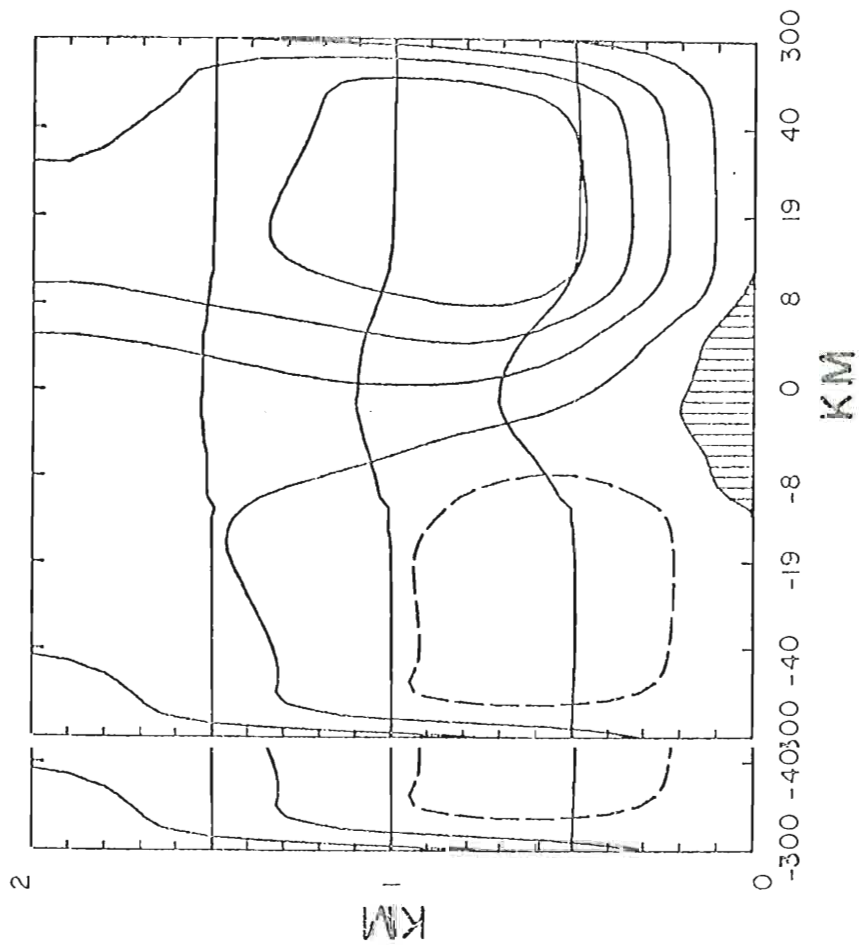
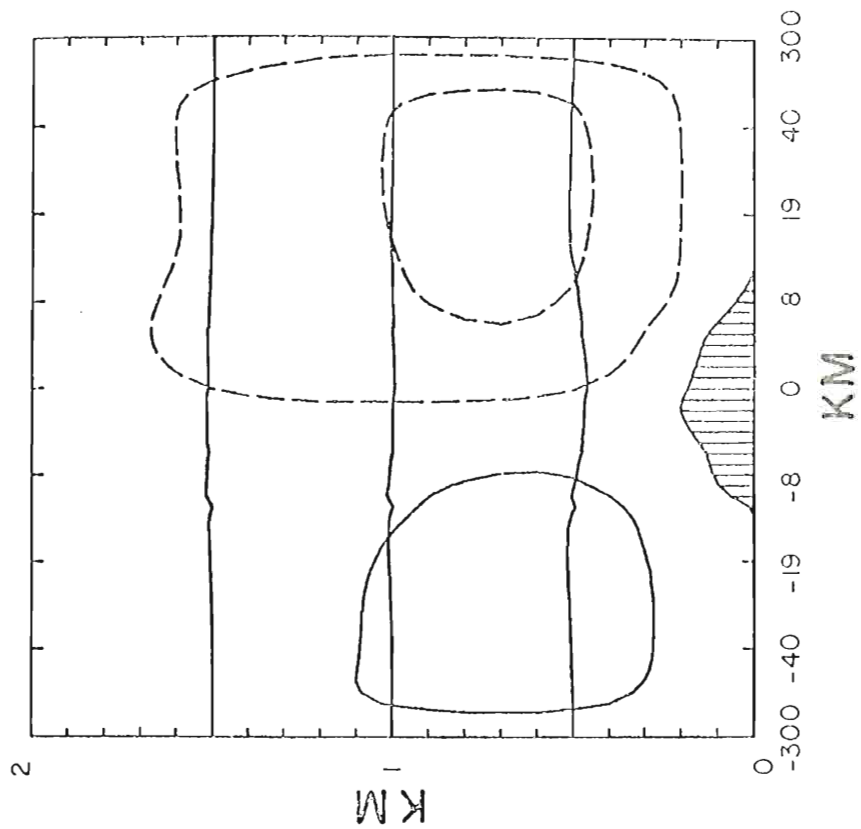


Fig. 10. Same as Fig. 7 but for Case B.

layer by 1000 LST. Maximum sinking motion in the land breeze at the top of the lowest layer is just less than 1 cm sec^{-1} by 1900 LST. As in the symmetric case, the maxima in the horizontal flow in both the land and seabreeze circulations are closely associated with the edges of the region of vertical motion over the island and both propagate seaward in time. Fig. 11 shows the propagation of the maxima in the u-component of both the sea and land breeze away from the island in time. Note that the sea breeze is re-established at the start of a new cycle earlier on the west than on the east as indicated by the point denoted with an S at 24 hr on the west side. As in the symmetric circulation the maxima develop over land and move seaward. In conjunction with Fig. 9 we observe that at the time of maximum intensity the maxima in the western cells are inland of the west coast and some acceleration is evident in the propagation of the maxima across the coast. On the east, however, the maxima are off shore at the time of maximum intensity. The change in location of the land breeze maximum from the second layer to the lowest layer is reflected in the discontinuity in the L-curve on the east side of the island after 0100 LST. Accelerated movement of the maxima away from the island after the times of maximum and minimum surface temperature is evident in Fig. 11. Thus, in both the symmetric and asymmetric double sea (land) breeze circulations, we observe that the maxima in the low level flow drift away from the island in time, accompanied by an expansion of the region of vertical motion over the island at the top of the lowest layer. Observational evidence in support or contradiction of this expansion of the region of vertical motion over the island at the top of the lowest layer. Observational evidence in support or contradiction of this result is lacking and it is contrary to results obtained in single coast sea breeze models (see for example, Fisher, 1961; Estoque, 1961, 1962),

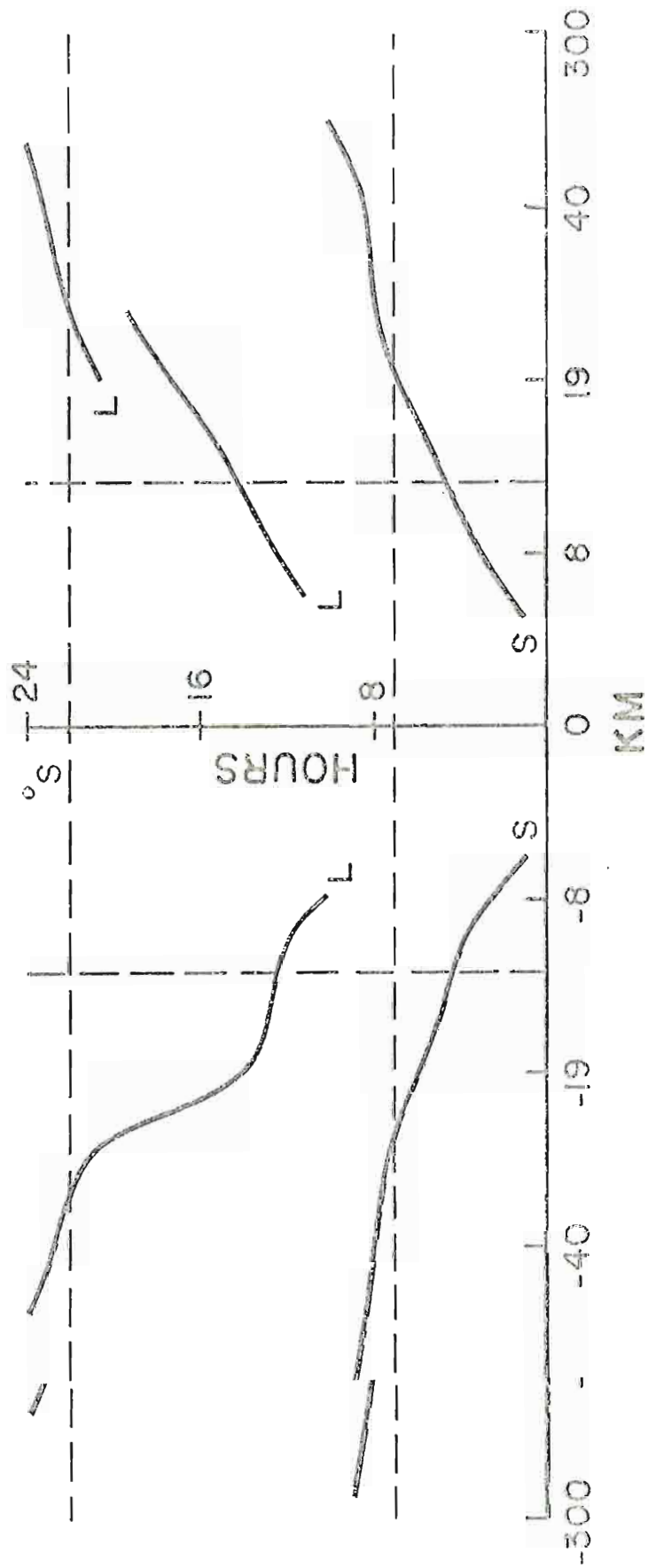


Fig. 11. Same as Fig. 8 but for Case B.

or in double seabreeze circulations over larger land widths (see, for example, Smith, 1957). The result also differs from those of Malkus and Stern (1953) and Estoque and Bhumralkar (1969). However, except for Estoque (1961, 1962) in the above models, the surface heating of the source is either independent of space or of both space and time, and topography is excluded.

The following explanation is advanced for the result observed in the present model. The spatial dependence of the surface heating places the source of maximum heating at the center of the island with a sinusoidal decrease towards each coast. A small region of effectively reduced mass due to heating is established over and near the center of the island early in the heating cycle. By continuity, an influx of low level air from the far field is accelerated towards this region, but is decelerated by the increased surface friction over the island and by convergence towards the center. Therefore, we expect maxima in the inflow to be established between the heat source and the coasts. As the width of the heat source increases with time to that of the island, the maxima must recede seaward away from their original positions. As surface heating decreases and cooling becomes effective, low-level outflow is established with maxima developing between the center of the island where maximum cooling occurs and the region where the developing outflow of the land breeze converges with the opposing inflow of the decaying seabreeze. Again the maxima develop initially over the island and move outward as the cooling region expands in time. The region of vertical motion over the island at the top of the lowest layer develops between the maxima in the low-level flow due to the method of computing

w at the interfaces, i.e., at the top of the lowest layer,

$$w_1 = w_p - h_1 \frac{\partial u_1}{\partial x}$$

For the seabreeze (inflow) $w_p > 0$, $\partial u_1 / \partial x < 0$ between the maxima, therefore $w_1 > 0$. The opposite is true for the land breeze (outflow). Thus, expansion of the region of vertical motions over the island at the top of the lowest layer is due to the seaward propagation of the maxima in the low-level flow.

These results suggest that an observational investigation of the seabreeze over Barbados might be appropriate; we can speculate immediately that the results should be different in some respects because the spatial distribution of surface heating in reality is most likely asymmetric with a maximum near the west coast.

Cases A and B demonstrate the relative importance of asymmetries in the geometry of topography on the low-level flow over a small heated island. The importance of the topography itself, without regard to its shape is examined in the following Cases C and D.

3.3 Case C: Flat island, $u_g = -4 \text{ m sec}^{-1}$

Vertical profiles and hodographs of the undisturbed state at the coasts and over the point corresponding to the crest of the real island are shown in Fig. 12. Note that the shear due to surface friction appears below the 500-mb level and that the flow becomes approximately geostrophic above. This is due to the fact that the lowest model layer extends initially to 500 m and that the velocity field adjusts to the geostrophic above. This is due to the fact that the lowest model layer extends initially to 500 m and that the velocity field adjusts to the mass field during the generation of the adjusted undisturbed conditions. Note further that a single profile is presented indicating that

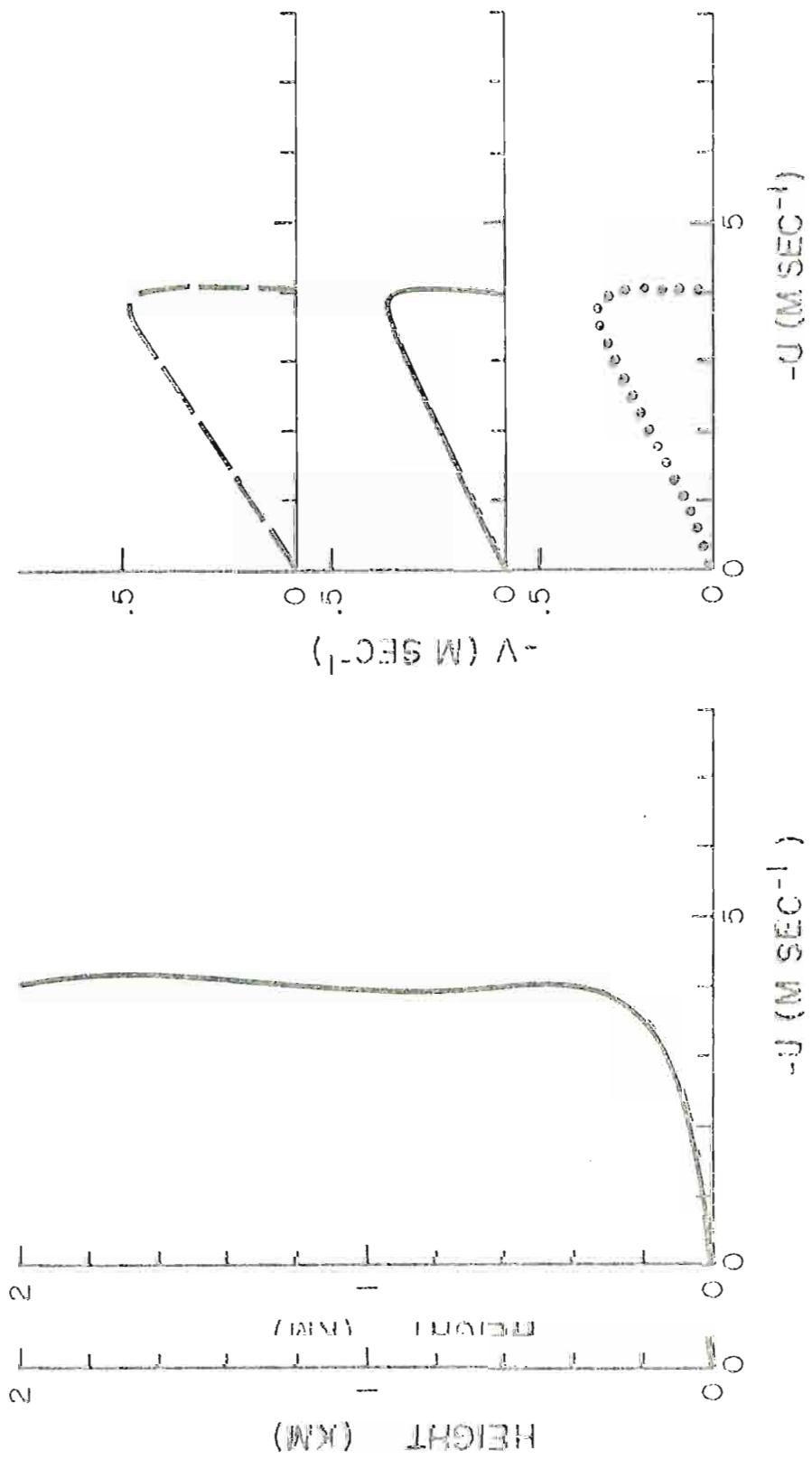


Fig. 12. Same as Fig. 2 but for Case C.

negligible differences exist between the three profiles. The northerly components shown in the hodographs have been discussed in Section 2.1(a) on initial conditions. The following are also observed in the adjusted flow field.

In the lowest layer the upstream zonal component decreases towards, then increases downward of, the east coast. The opposite occurs in the second layer, however the changes in wind speed across the model region are approximately 1 per cent of the wind at the east coast and may be considered negligible. The meridional component in the lowest layer increases approaching the east coast from upwind of the island, decreases downwind of the east coast over the island, and increases again downwind of the west coast. The decrease in speed across the island is approximately 16 per cent of the wind speed at the east coast. Downward vertical motions of the order of 1 mm sec^{-1} are observed at the top of the lowest layer over the island. Balance of forces computed at selected points in the model region shows an approximate Ekman balance in the undisturbed flow over the flat island and mass flux divergences between the reference points indicate that the steady state continuity equation is approximately satisfied.

Figs. 13 and 14 show the vertical profiles of the u-component, and hodographs at times of maximum and minimum surface temperature for the reference points. At the time of maximum surface temperature an increase in the u-component in the low-level flow, and a decrease in the mid levels over the east coast with the opposite result over the west coast in the u-component in the low-level flow, and a decrease in the mid levels over the east coast with the opposite result over the west coast suggest the establishment of a double seabreeze circulation with maximum inflow (sea to land) near 300 m and maximum outflow (land to sea) near

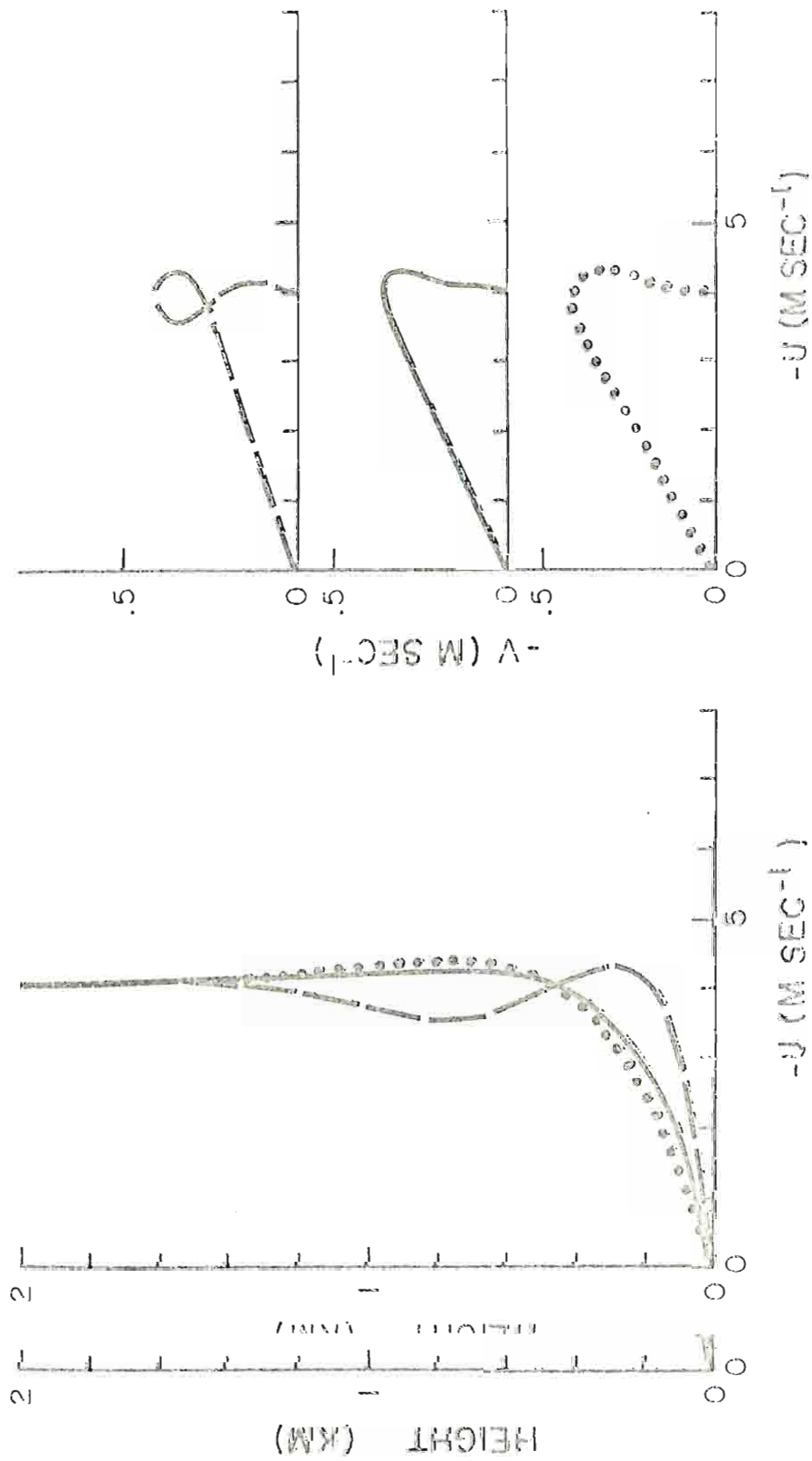


Fig. 13. Vertical profiles of the u-component, and hodographs over the east coast (dashed), west coast (dotted) and the position of the hill crest (solid) at 1300 LST.

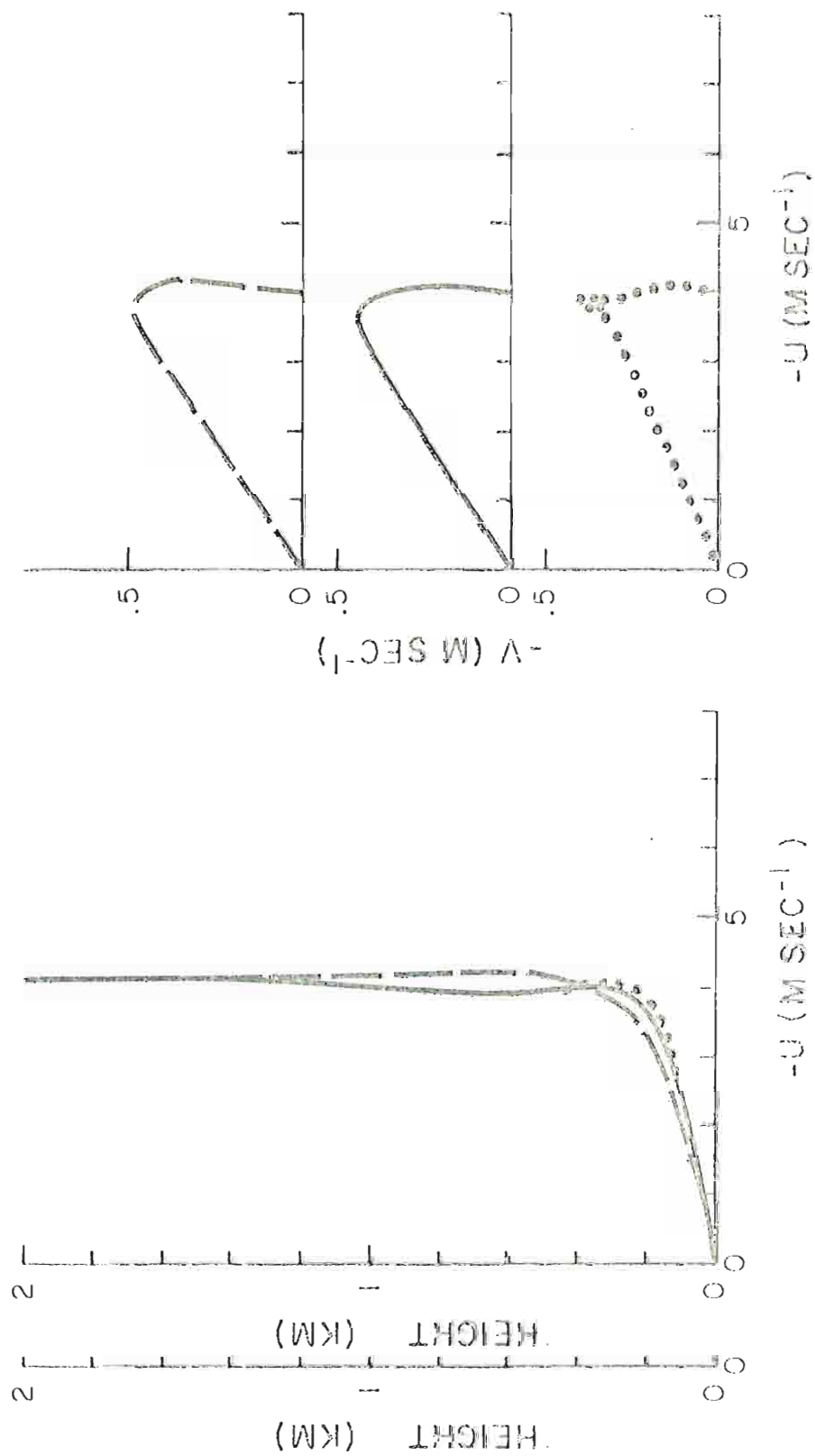


Fig. 14. Same as Fig. 13 but for 0400 LST.

800 m. The hodographs for this time show low-level veering and slight backing aloft over the east coast which is consistent with the superposition of the seabreeze circulation in the undisturbed flow. The interpretation of the result on the west coast is somewhat more complicated. Here the backing in the lowest layer and veering in the second layer are consistent with a shallow seabreeze cell, however backing above the 1 km level is evident in the v-component. The reason for this result is not clear. By comparison we find a stronger perturbation circulation resulting from an imposed mean flow over a flat island than for initially static conditions over topography. The reason for this result will be discussed later when a similar observation will be made for the results of Case D.

The time variation of the perturbation circulation exhibits the following features. By 0800 LST a slightly larger seabreeze cell develops on the eastern than on the western side of the island. The region of upward vertical motion associated with the seabreeze is centered over the center of the island or directly over the heat source. By 1000 LST the western cell becomes larger than the eastern cell, but the intensity of the low-level flow is approximately the same in each. The region of upward motion is now centered slightly to the east of its original position. Thereafter, the intensity of the flow increases, attaining a maximum at the time of maximum surface temperature, then decreases with the decline in temperature when the western cell becomes more intense than the eastern cell. Both eastern and western circulations move away from the island after the time of maximum surface temperature, and by 1300 LST the eastern cell has disappeared but the western cell is still evident

far downstream of the island. The flow then undergoes a transition from the daytime seabreeze to the nighttime land breeze which first becomes evident as a small low-level circulation near the west coast by midnight. During the last six hours of the heating cycle, the land breeze develops with a deep circulation on the west and a shallow circulation on the east of the island. Unlike the circulation generated in static initial conditions over asymmetric topography, the asymmetries in this case are due to the existence of a large-scale flow. Fig. 15 shows the perturbation streamfunction for the times of maximum and minimum surface temperature. Upward vertical motions of approximately 2 cm sec^{-1} at the 500 m level occur over the island with sinking motions off shore in the seabreeze. The opposite occurs in the land breeze in which the downward motions over the island at 500 m average 6 mm sec^{-1} .

By comparing the forced solutions with the adjusted initial state we observe that, in the lowest layer, the western maxima in the perturbation u-component of both the land and seabreeze remain virtually stationary within 1-4 km of the west coast. On the east the seabreeze maximum propagates from approximately 3 km inshore to about 4 km offshore, while the land breeze maximum remains fixed about 1 km offshore. The region of vertical motions at the top of the lowest layer over the island is again closely associated with the perturbation maxima. Although comparison with Case A is not entirely feasible, we may ascribe the differences between the results, i.e., the changes in the propagation of the perturbation maxima, to the effect of nonlinear advection of the mean flow.

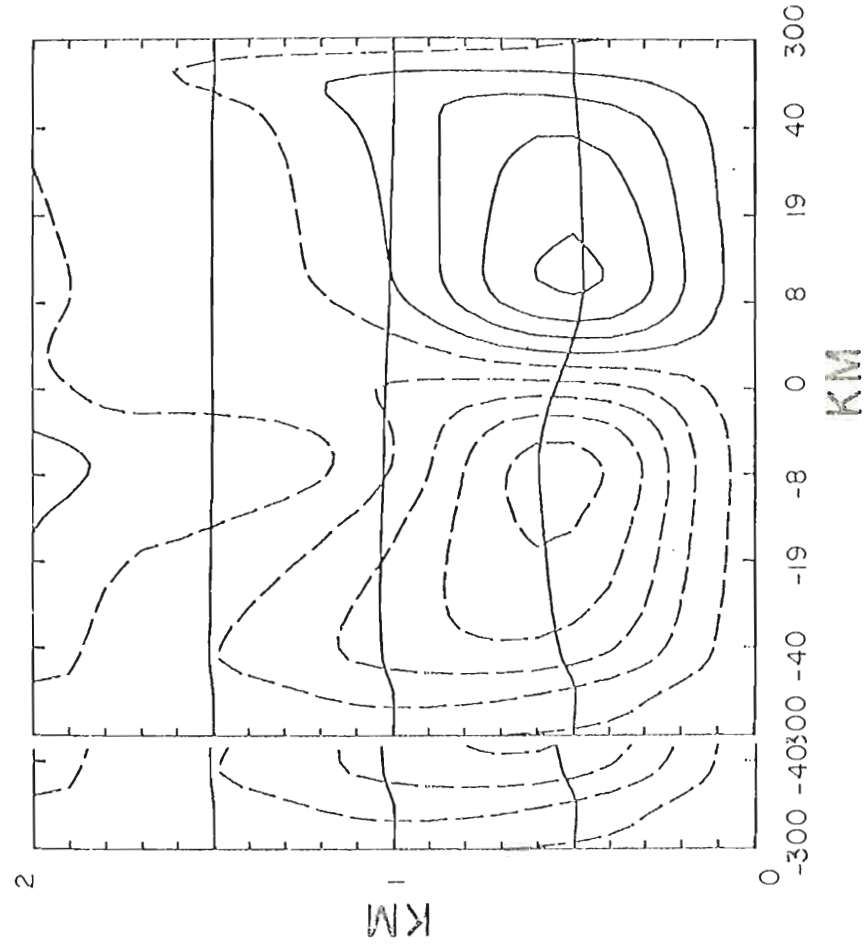
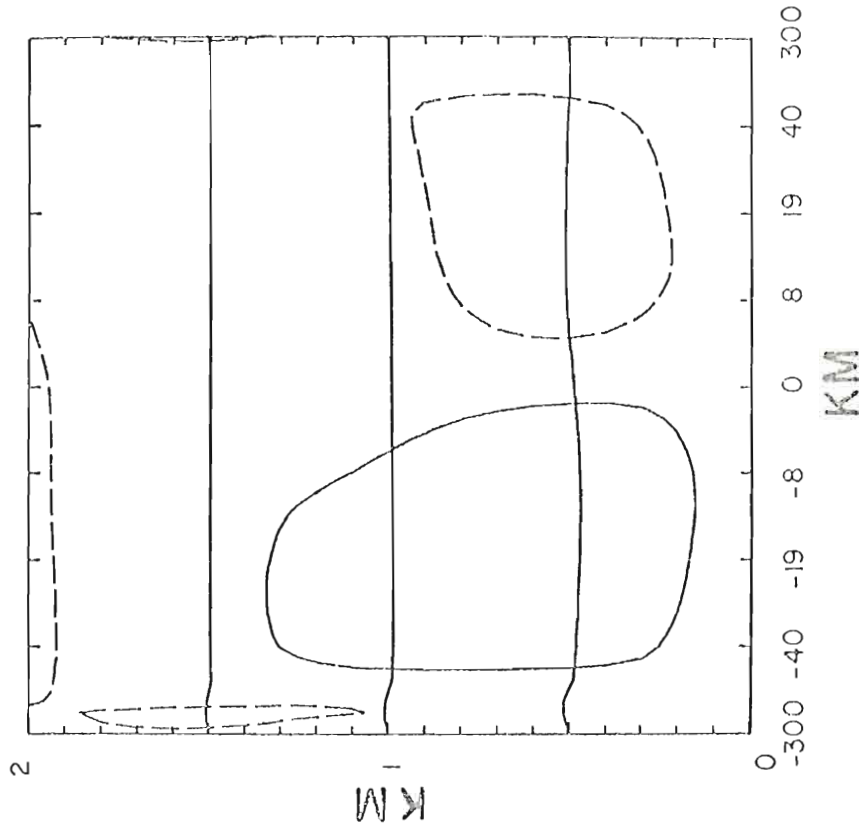


Fig. 15. Same as Fig. 7 but for Case C.

3.4 Case D: Real island, $u_g = -4 \text{ m sec}^{-1}$

The combined effects of the island and the surface heating on the flow are demonstrated in this case. Fig. 2 shows the vertical profiles of the zonal components and the hodographs for the adjusted undisturbed state over the reference points. The profiles and balance of forces computations indicate an approximate geostrophic flow in the upper two layers, however, no simple balance can be determined in the lower layers as in Case C. The balance of forces indicates that over the island both advection and horizontal friction play important roles in the lowest order balance. The role of advection both here and in Case C, is an indication of the importance of the nonlinearity of the model. Thus, some of the main results cannot be obtained by linear analytical methods. The importance of horizontal friction may be, however, peculiar to the model and unrepresentative of the atmosphere. It is associated with the determination of the horizontal diffusion coefficient which was chosen to control the development of $2\Delta x$ oscillations. The suppression of $2\Delta x$ temperature oscillations was mentioned in Section 2.2(b) on boundary conditions. During preliminary tests, $2\Delta x$ oscillations were generated by the centered difference form of the advection term in the temperature equation (see Fisher, 1961). The horizontal diffusion coefficient required to sufficiently smooth these spurious oscillations and prevent their growth was determined by assuming the balance

$$u \theta_x = K \theta_{xx} .$$

For grid scale motion

$$u \theta_x = K \theta_{xx} .$$

For grid scale motion

$$K = u \Delta x .$$

Since the diffusion coefficients are assumed to be the same for all quantities, the diffusion coefficient for momentum is conveniently defined as the product of the magnitude of the imposed geostrophic flow at the upper boundary (u_g) and the minimum grid distance in the model (1 km). When $u_g = 0$, the diffusion coefficient is taken to be $10^3 \text{ m}^2 \text{ sec}^{-1}$, i.e.,

$$K(u_g = 0) = K(u_g = 1 \text{ m sec}^{-1}).$$

The maximum imposed geostrophic flow in this study is 8 m sec^{-1} , thus

$$K_{\text{max}} = 8 \times 10^3 \text{ m}^2 \text{ sec}^{-1}$$

which is of the order of the commonly used value ($10^4 \text{ m}^2 \text{ sec}^{-1}$) for the horizontal diffusion coefficient. Consequently, we maintain that the argument for the inapplicability of the Ekman balance assumption over topography remains valid. The profiles (Fig. 2) clearly show the supergeostrophic zonal component developed over the crest of the island due to the decrease in layer thickness which demonstrates the adjustment of the velocity field to the mass field. The spatial distribution of the velocity components display similar characteristics to those observed in Case B, however, due to the maximum over the crest of the zonal component in the lowest layer, there is a decrease in this component downwind of the crest. Further, the v-component in the lowest layer becomes less than that in the layer above over a distance of approximately 24 km westward from just east of the crest. The region shifts eastward with heating and is situated over the island at the time of maximum surface temperature, extending a few kilometers upwind of the east coast. It returns westward as the land cools. This shift is due in part to the

changes in the v-component resulting from the Coriolis effect on the u-component of the perturbation flow. By comparison, the undisturbed condition for the flow over the flat island does not show a decrease in the v-component in the lowest layer relative to the layer above it anywhere in the model region. However, with heating this differential develops over a region from approximately 30 km east of the east coast to about the midwestern section of the island, due again in part to the Coriolis effect on the perturbation zonal flow, which causes a decrease in the northerly component in the lowest layer and an increase in the layer above on the east of the island. The opposite occurs on the west of the island. Sinking motions of up to 7 cm sec^{-1} are observed at the top of the lowest layer mainly over the eastern slope of the island above the region of increasing easterlies. Maximum sinking motions between 2 and 7 cm sec^{-1} occur at all levels above the crest of the island. Weak sinking motions dominate the upper levels east of the island with wavelike motions over the island. The region of sinking motion associated with the wave structure is found over and to the east of the crest. We observe that the maximum sinking motions in this case are an order of magnitude larger than those over the flat island in the undisturbed state.

The development of the perturbation circulation in time shows that on the eastern side of the island the circulation is similar to that for the flat island. The seabreeze circulation on the east develops to a maximum by 1300 LST then decays, and by 1700 LST the that for the flat island. The seabreeze circulation on the east develops to a maximum by 1300 LST then decays, and by 1700 LST the circulation disappears.

The similarity in the time-dependent behavior of the eastern sea-breeze cell to that of the flat island may be attributed to the fact that the major disturbing influences on the flow are applied downwind of the east coast.

As in the flat island case, the propagation of this cell is most pronounced after the time of maximum surface temperature. A noticeable difference from the flat island case occurs in the western circulation which is now centered over the crest of the island with upward motions at 500 m of order 7 cm sec^{-1} concentrated over the eastern slope and downward motions of order 3 cm sec^{-1} over the western slope. As early as 0800 LST, the western cell of the seabreeze is more intense than the eastern. The increase in intensity of the circulation persists until approximately 1400 LST. The western cell of the seabreeze remains over the island during the day then its center propagates rapidly upward between 1700 and 1800 LST. However, a secondary cell forms off shore between 1600 and 1700 LST above the 1-km level and drifts downwind and upward, disappearing by 2200 LST. The transition flow between the sea and land breeze is more complex and more intense than in the flat island case. The nighttime land breeze circulation is evident by 2300 LST, an hour earlier than in the flat island case. This circulation develops almost above the crest of the island. The land breeze persists until heating is resumed with maximum intensity at 0500 LST. Upward vertical motions of order 2 cm sec^{-1} occur over the western slope and sinking motions of order $1-2 \text{ cm sec}^{-1}$ over the eastern slope of the island. Fig. 16 shows the perturbation streamfunctions for the sea and land breeze at the time of maximum and minimum surface temperature during the first heating cycle. The vertical profiles of zonal components and hodographs

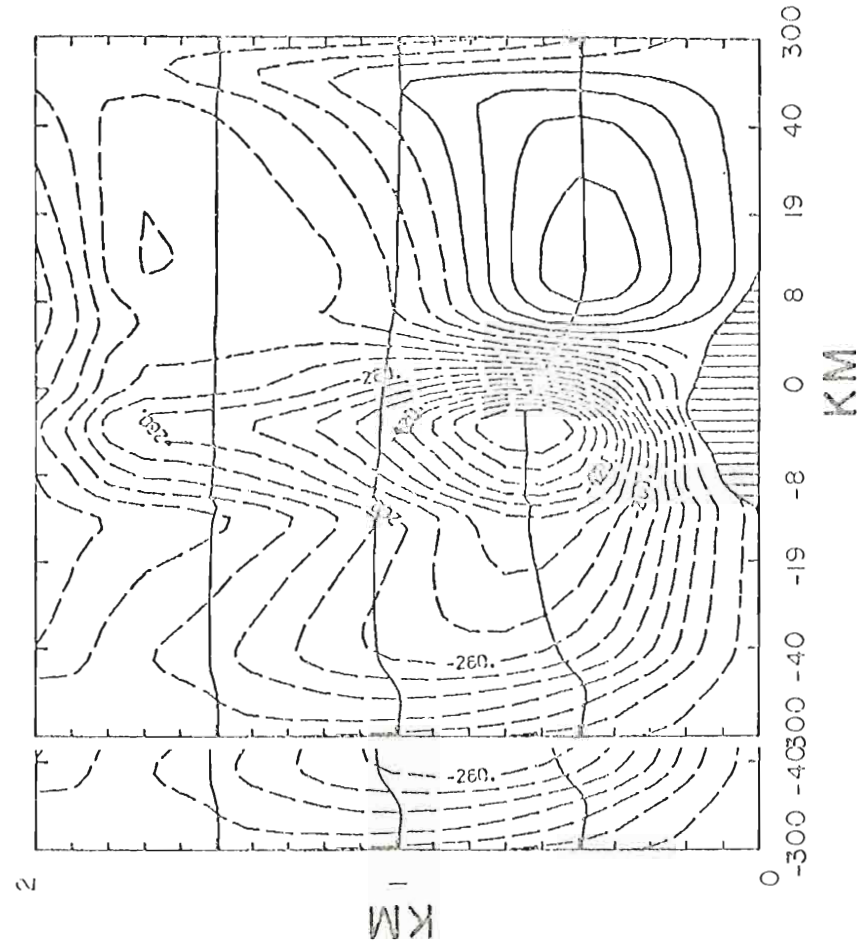
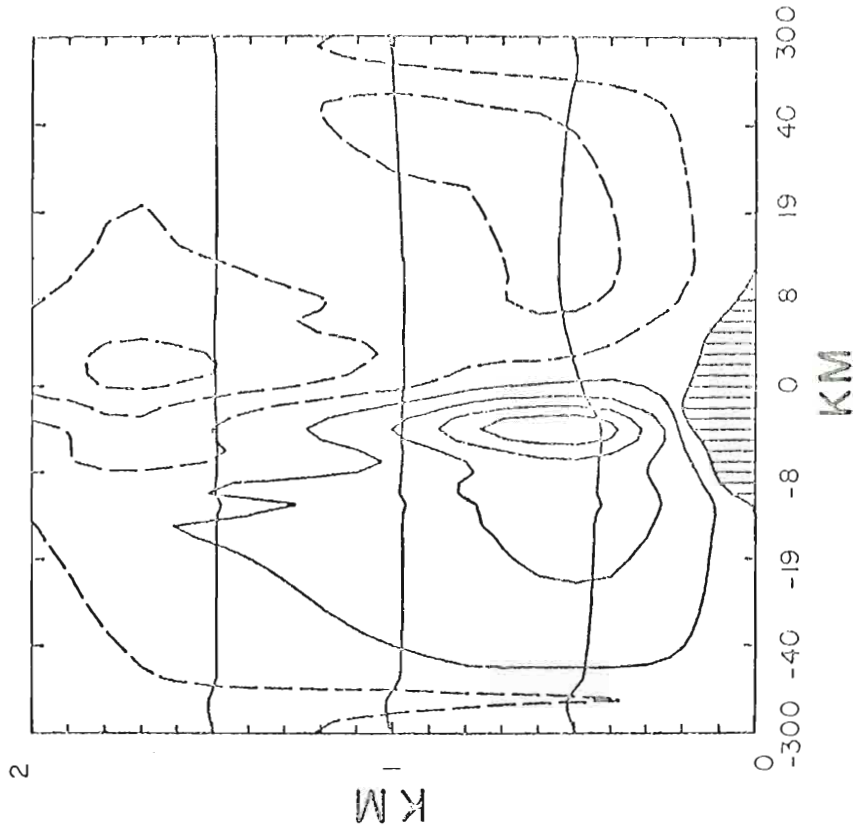


Fig. 16. Same as Fig. 7 but for Case D.

at the times of maximum heating and cooling are shown in Figs. 17 and 18, respectively. The effect of the double sea (land) breeze is evident from the time variations in the profiles. On the resumption of the heating cycle the sea (land) breeze cycle repeats itself. Fig. 19 shows the perturbation streamfunctions at the time of maximum and minimum surface temperature during the second heating cycle. By comparison with Fig. 16 we observe that, although the actual values of the isolines differ, the spatial distribution of the circulations is almost identical, and the flow intensities depicted by the gradients of the streamfunctions are essentially equal. The cyclic repetition of the flow in response to the repetition of the heating cycle is demonstrated in Fig. 20 which shows the u- and v-components in the lowest layer over the reference points for two heating cycles (18 hrs). Table 4 lists the u-components of the seabreeze circulation at 1300 LST for Cases B, C, and D. The perturbation circulation for the flow over topography (Case D) is, in general, stronger than that over a flat island (Case C) with all other conditions equal, or the thermal circulation generated over topography in an initially static condition (Case B). Further, the strength of the former is usually greater than the combined strengths of the latter two, which is an indication of the nonlinearity of the problem. The increase in intensity of the perturbation flow in Cases C and D relative to Cases A and B is due to the existence of a mean flow in C and D which causes increased fluxes of sensible heat and moisture from the surface mainly through the increased existence of a mean flow in C and D which causes increased fluxes of sensible heat and moisture from the surface mainly through the increased influence of the bulk aerodynamic terms.

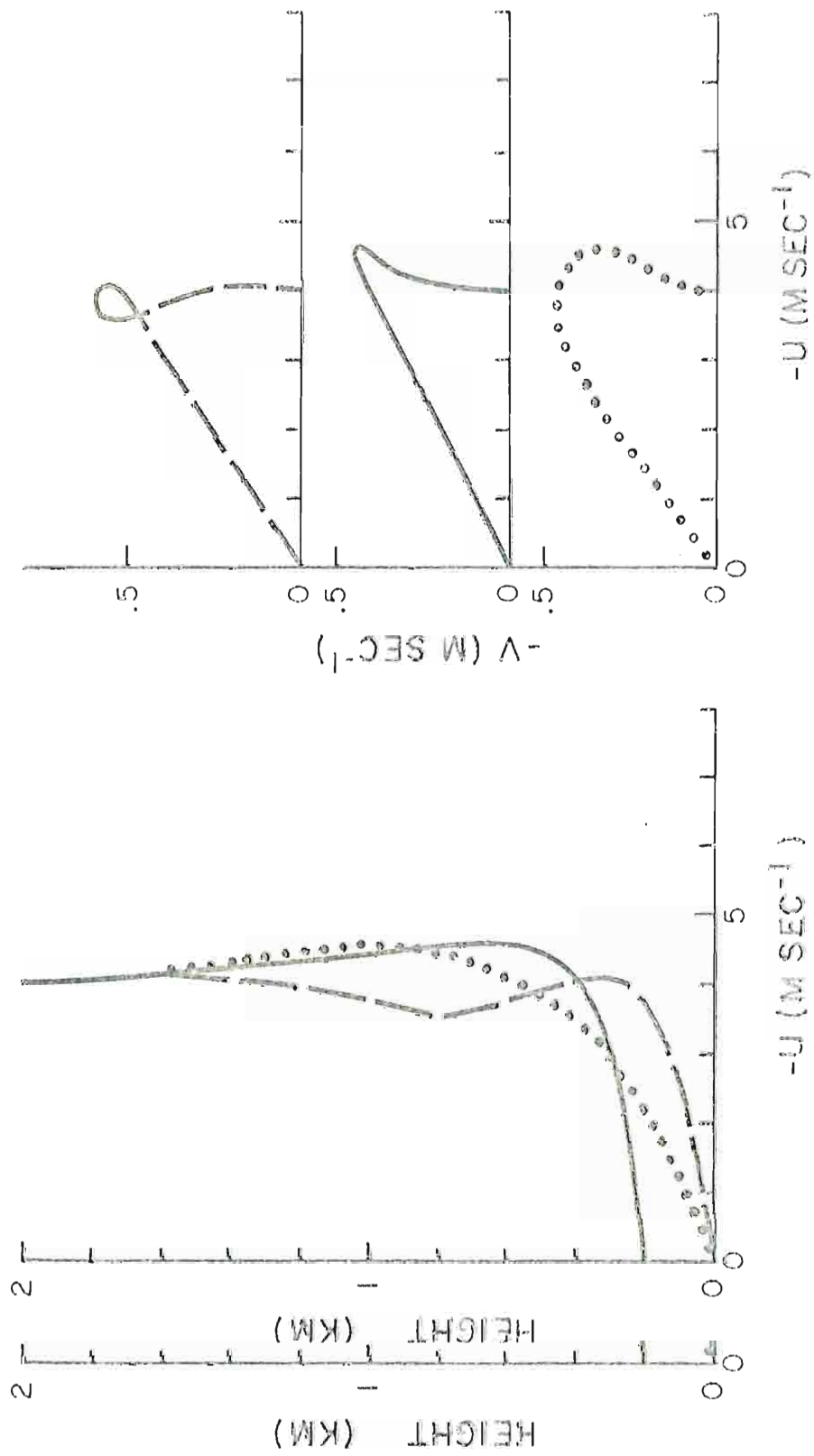


Fig. 17. Same as Fig. 13 but for Case D.

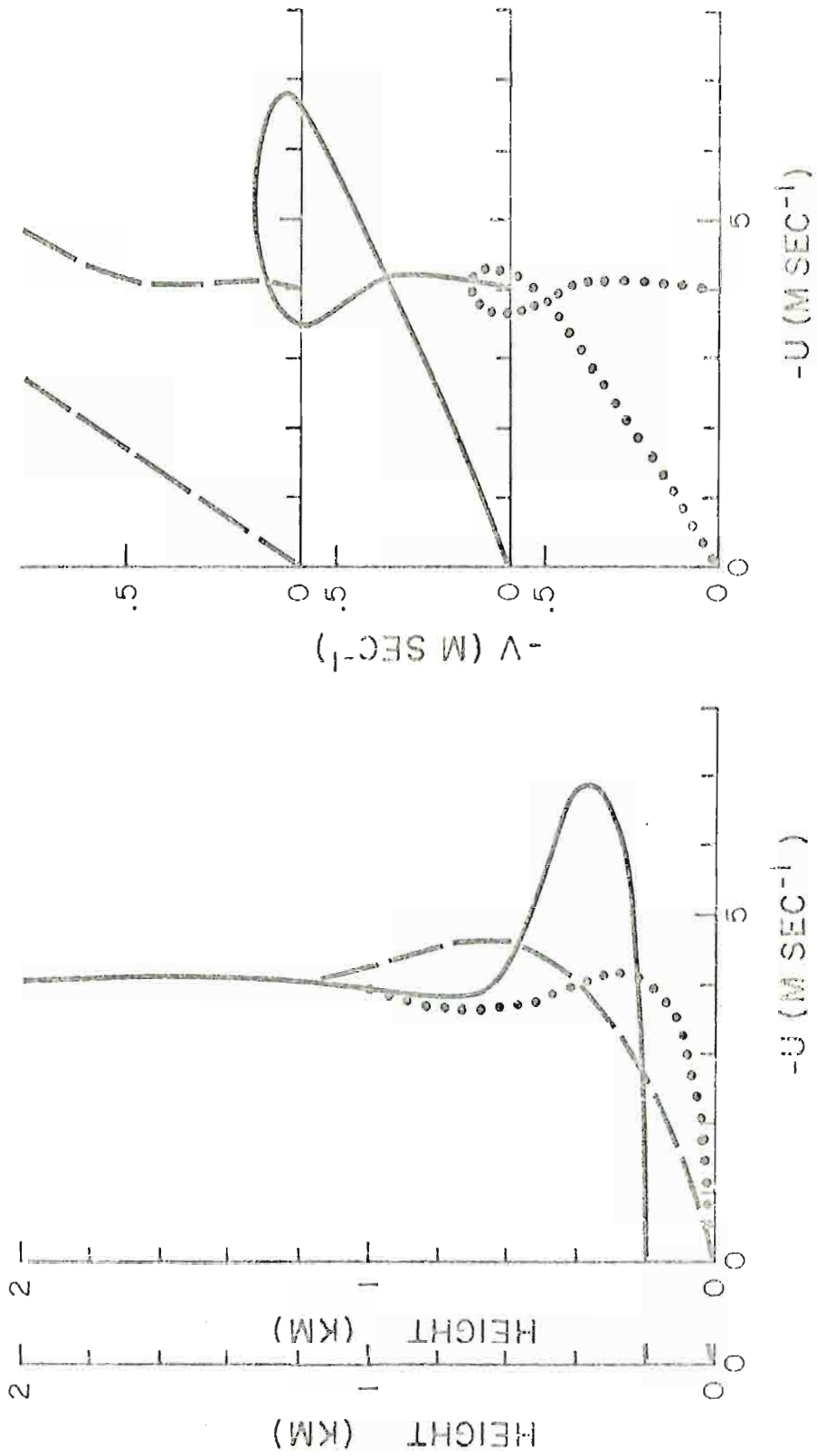


Fig. 18. Same as Fig. 14 but for Case D.

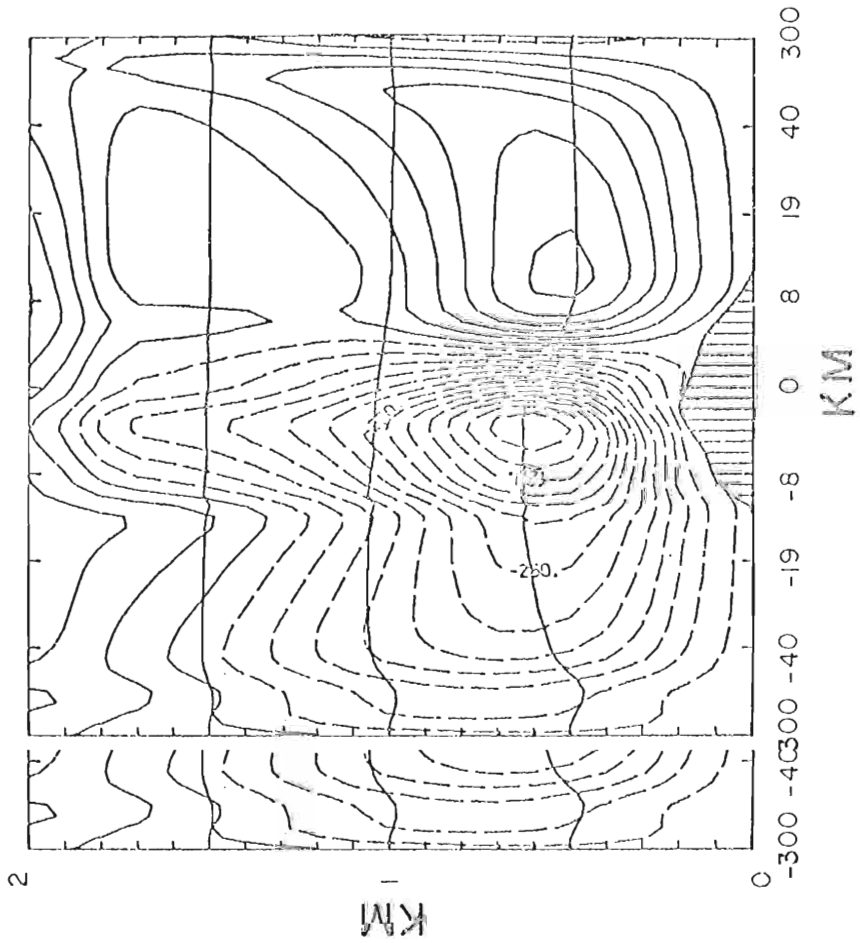
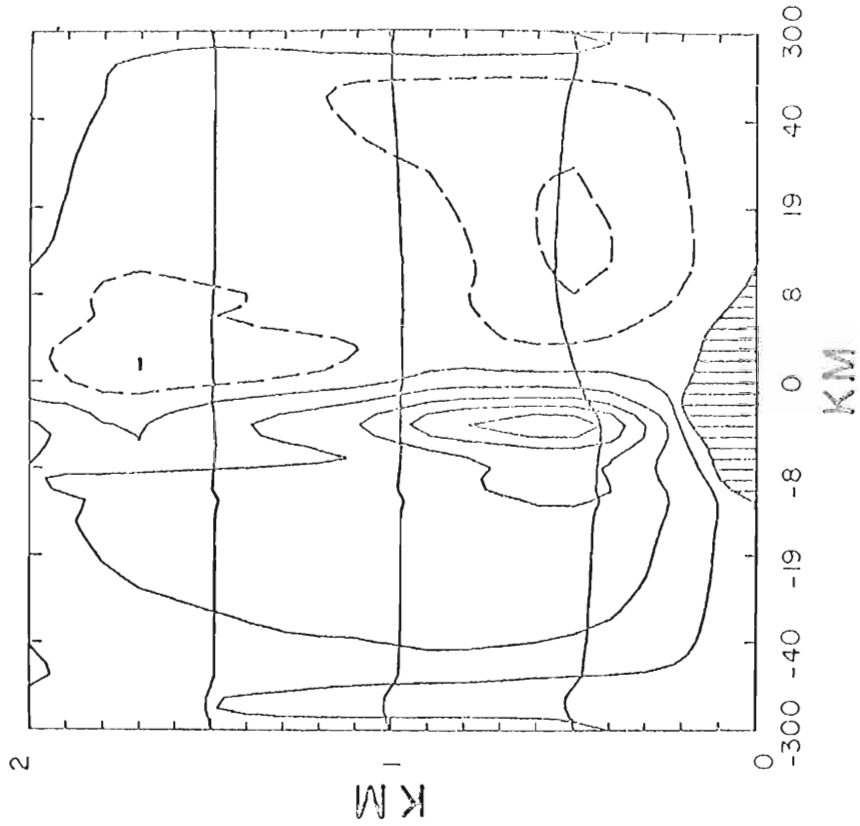


Fig. 19. Same as Fig. 16 but for second heating cycle.

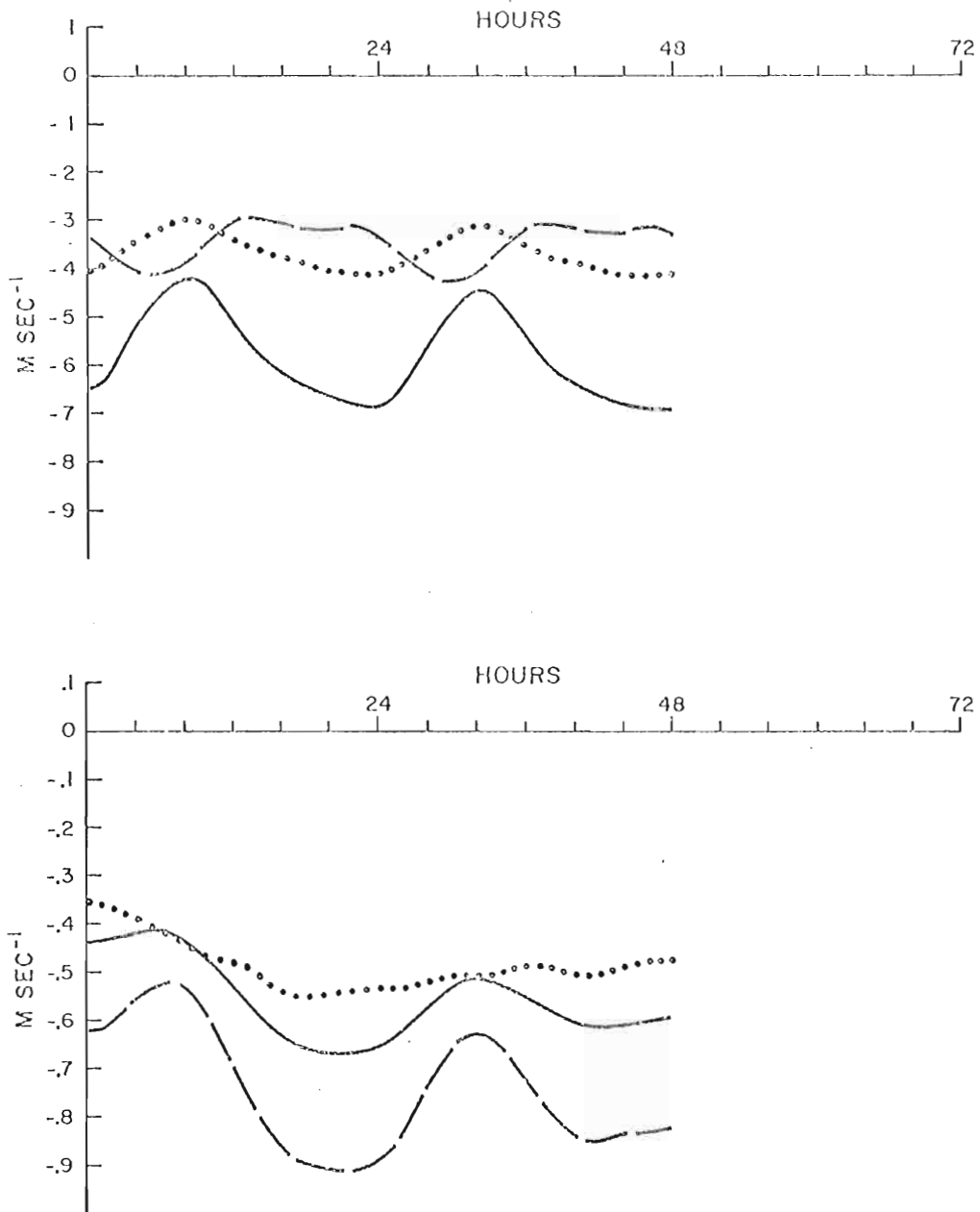


Fig. 20. u (upper) and v (lower) components in the lowest layer over the east coast (dashed), west coast (dotted) and hill crest (solid) as functions of time for Case D. The v scale is magnified 10 times relative to the u scale.

Table 4. Zonal perturbation velocity components over the coasts for Cases B, C, and D at 1300 LST. Negative values indicate easterly winds. Units are m sec^{-1} .

Layer	Case B		Case C		Case D	
	WC*	EC [†]	WC	EC	WC	EC
1	0.06	-0.22	0.44	-0.49	0.93	-0.58
2	-0.07	0.04	-0.43	0.43	-0.68	0.84
3	-0.04	0.05	-0.11	0.08	-0.28	0.06
4	-0.04	0.04	0.00	0.01	-0.01	0.04

*WC - West Coast

†EC - East Coast

The western maxima in both land and seabreeze remain within 2 km downwind of the crest of the island in time. The maxima on the east drift from approximately 6 km inland to about 7 km offshore. By comparison with Case B, we may account for the change in propagation characteristics of the maxima by nonlinear advective effects of the mean flow. By comparison with Case C the repositioning of the western maxima may be ascribed to the existence of topography.

3.5 Perturbation temperature and moisture fields

We have discussed the perturbation flow fields resulting from the surface heating of moist air over selected topographic configurations with and without an initial flow. We now look briefly at the perturbation temperature and moisture distributions. Cross sections of with and without an initial flow. We now look briefly at the perturbation temperature and moisture distributions. Cross sections of perturbation temperature for Cases B and D at the time of maximum surface temperature (1300 LST) are shown in Fig. 21. Note the symmetry in

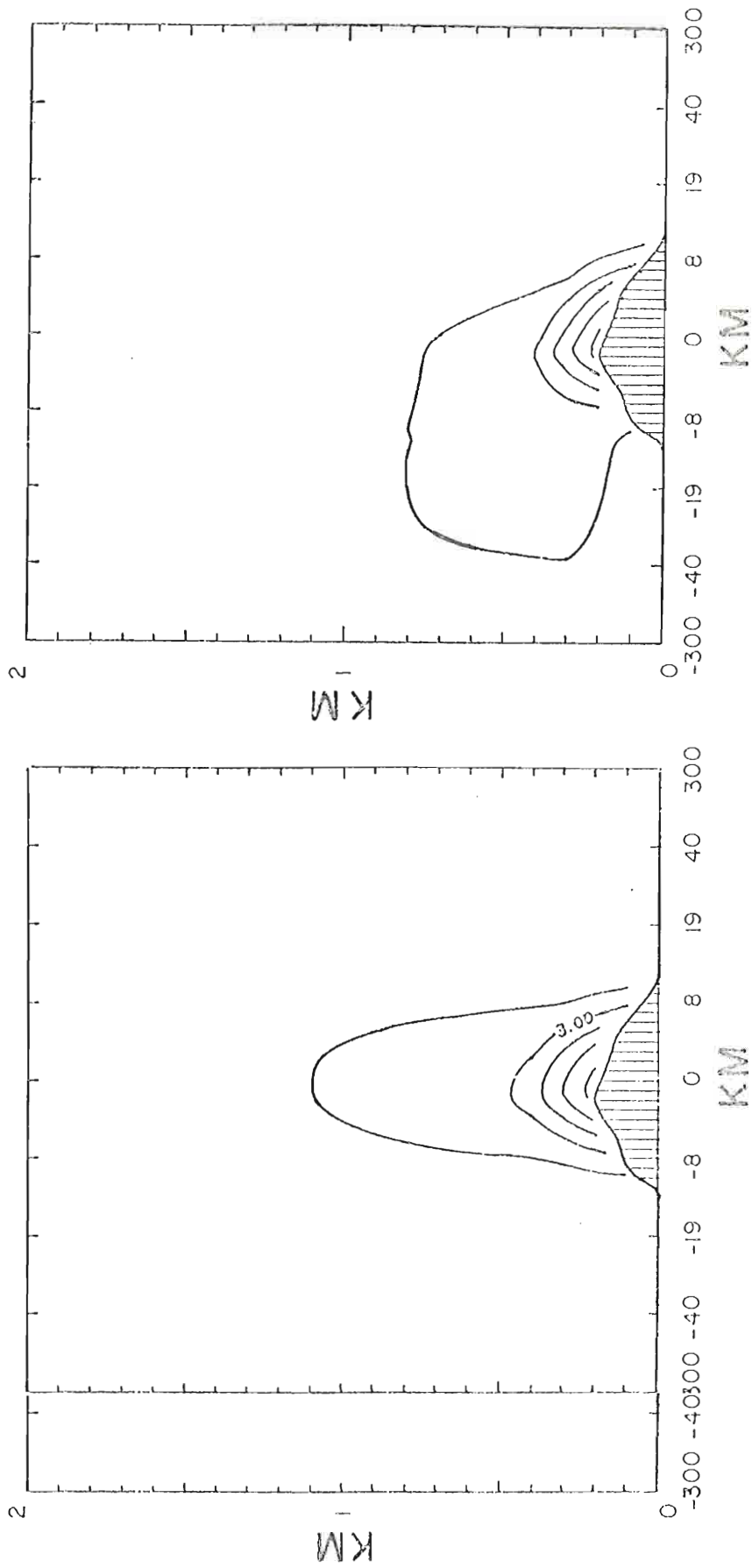


Fig. 21. . 21. Perturbation temperatures for Cases B (left) and D (right) at 1300 LST. Values range from 1K to 9K by increments of 2K.

Case B due to lack of advection by the mean flow, and the downwind plume in Case D due to advection. The cross section for Case B also indicates that topographic effects are less detectable in the perturbation temperatures than in the perturbation flow fields.

Cross sections of the perturbation moisture fields for Case B at the times of maximum and minimum surface temperature are shown in Fig. 22. In the absence of a mean flow the perturbation moisture maxima are concentrated over water at approximately 750 m with a dry region over the island below 500 m. A comparison of the perturbation moisture fields for all cases with mean flow indicate that they are essentially independent of the strength of the mean flow, and attain a quasi-steady state after the first 24 hrs of heating. Cross sections of the perturbation moisture fields representative of this steady state are shown in Fig. 23 for Case F at 1300 and 0400 LST of the third day of heating. There is a daytime concentration of moisture at approximately 850 m over land and at 750 m over water, with a maximum over and to the west of the hill crest in the region of downward perturbation motion. At night, the maximum shifts offshore.

The redistribution of moisture (Figs. 22, 23) is most likely due to turbulent fluxes rather than to vertical motions. The all positive perturbations for cases with mean flow (Fig. 23) is due to an effective and constant moisture source at the surface, and less effective moisture sinks anywhere in the model region.

At night, the region of upward motion over the western slope could interact with the available moisture to produce convective shower

At night, the region of upward motion over the western slope could interact with the available moisture to produce convective shower activity. These conclusions are highly speculative since no attempt is made to parameterize latent heat release and condensation processes.

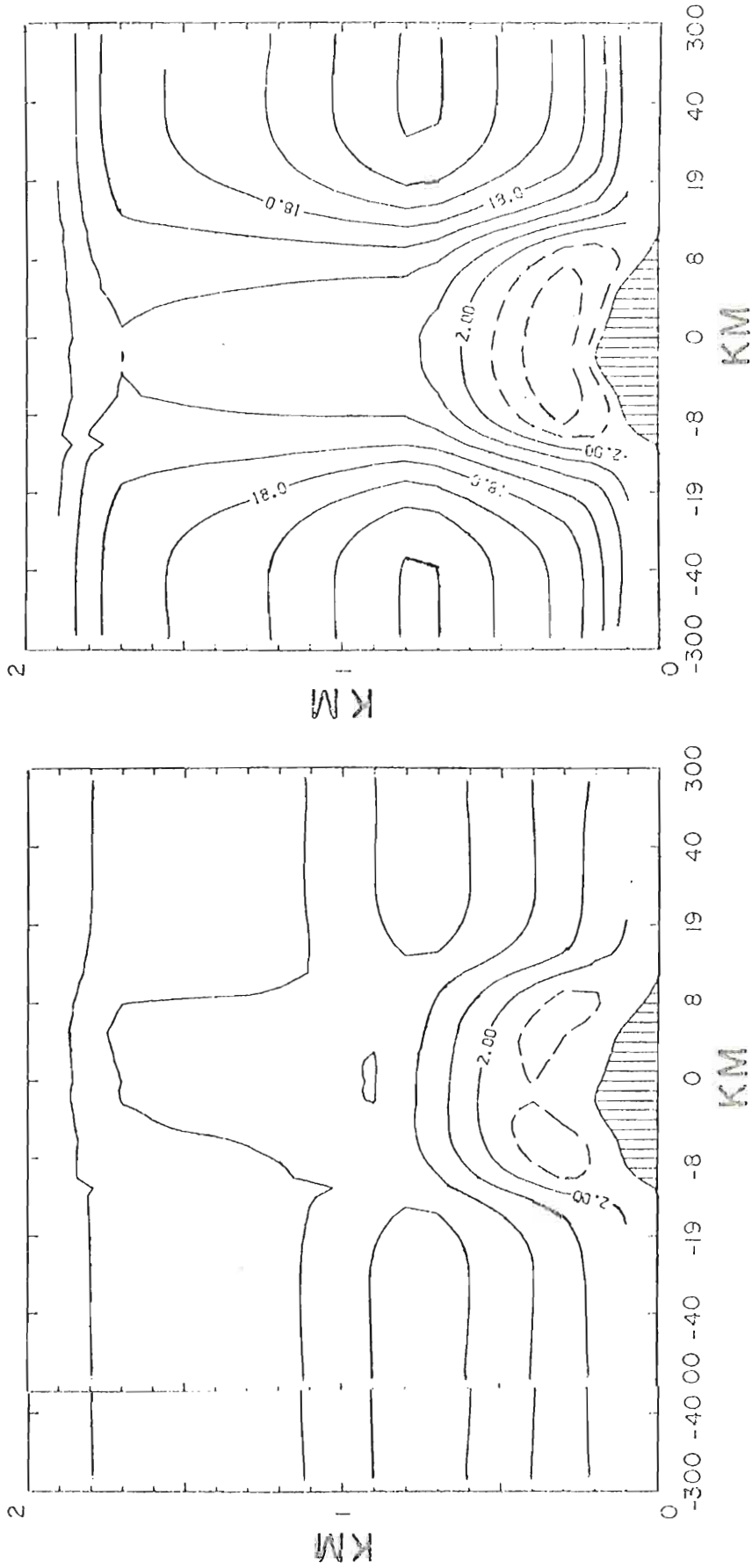


Fig. 22. . 22. Perturbation mixing ratio for Case B at 1300 LST (left) and 0400 LST (right). Units are 0.1 gm kg⁻¹. Contour interval is 4 units.

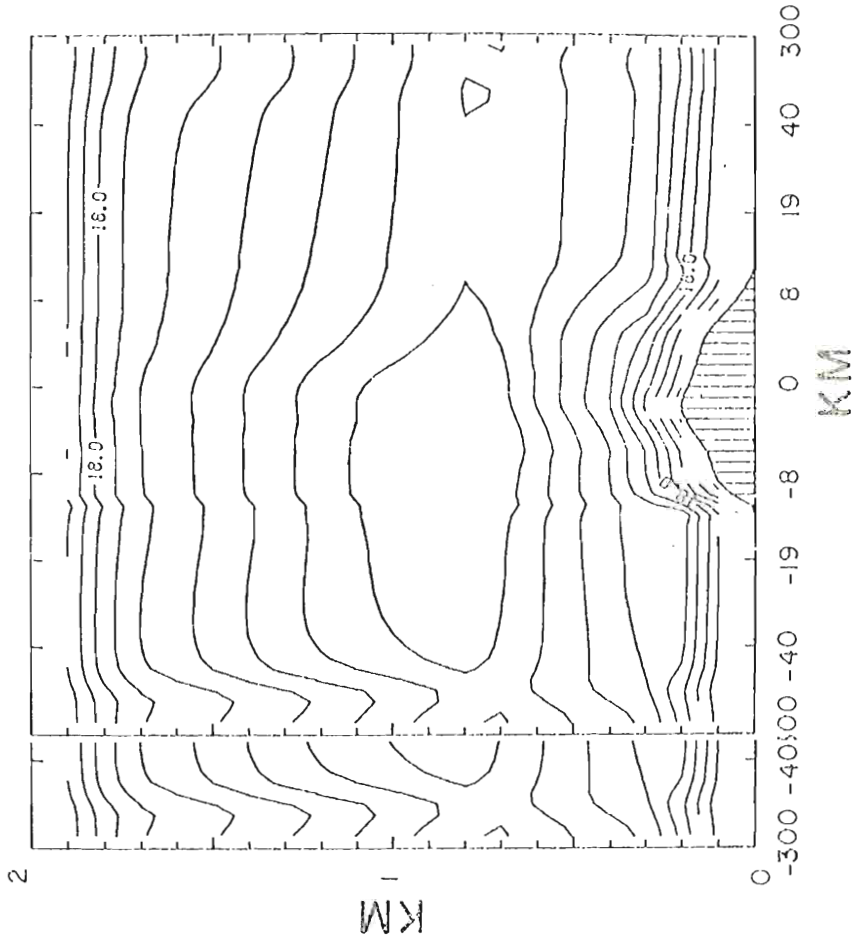
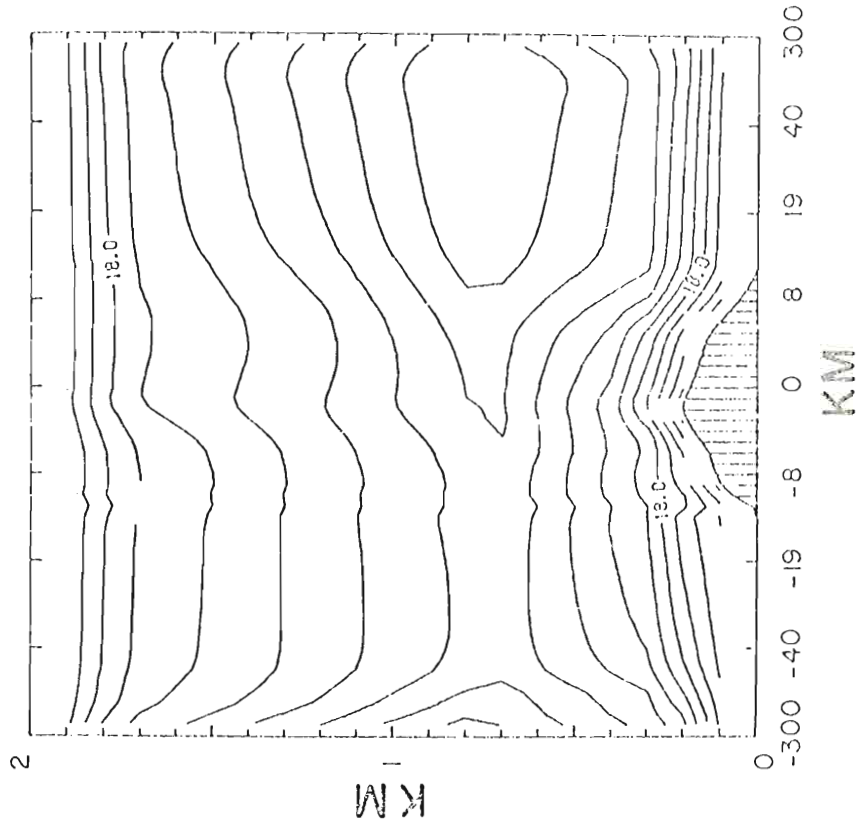


Fig. 23. Same as Fig. 22 but for cases with mean flow.

3.6 Effect of variation of physical properties

A brief discussion follows on the effect of constant heating, moisture, and changes in geostrophic wind speed on the model results.

(a) Constant versus variable heating

The results of Cases A through D indicate that the time and spatial dependence of the surface heating cause offshore propagation of the perturbation circulations and the maxima in the low-level flow. The results also show that nonlinear and topographic effects modify both the geometry and behavior of the circulation features. We now consider the effect of maintaining the surface heating constant in space and time by examining the perturbation over both the flat and real islands forced by the mean land-sea temperature excess of 2.85 K (Cases J and K). Only a seabreeze circulation results in these cases. The specified easterly geostrophic wind is 4 m sec^{-1} .

Over the flat island (Case J), constant heating produces maximum intensity in the eastern seabreeze cell at approximately two hours after the start of heating. A relatively steady state is reached after eight hours. The intensity of the western cell of the seabreeze and of the minor upper circulation cell on the east oscillate with a periodicity of approximately 10 hours. The oscillation is due to the impulsive application of heating to the model. Over the real island (Case K) the intensity of the eastern sea breeze cell gradually decreases during the first six hours then reaches a steady state. The western cell, which as with variable heating is centered over the crest of the island, in first six hours then reaches a steady state. The western cell, which as with variable heating is centered over the crest of the island, intensifies to a maximum by the tenth hour then weakens slightly to reach a steady state after fourteen hours. In both cases the western maximum

remains within 4 km off the west coast. The region of vertical motion at the top of the lowest layer is closely associated with the perturbation maxima in the flat island case but not in the real island case. Maximum vertical motion at this level is of order 1 cm sec^{-1} at approximately 2 km inland from the east coast.

(b) Effect of moisture

The effect of moisture is demonstrated by comparing Cases H and I with Case D. Comparison of Cases H and D shows the total effect of moisture, and comparison of Case I with Case D shows the effect of surface moisture gradient on the perturbation flow. In Case I the sea surface evaporative flux is reduced to that of the land. Comparative results for the east and west coasts at the time of maximum heating are listed in Table 5. Apart from the results in layer 3, we observe that moisture causes the perturbation flow to be at least 70 per cent stronger over the west coast and up to 30 per cent stronger over the east coast (Case D vs. Case H), while the absence of the land-sea surface moisture gradient allows for an increase of order 10 per cent over that with increased sea surface evaporative flux (Case I vs. Case D).

Table 5. Zonal perturbation velocity components over the coasts for Cases D, H, and I at the time of maximum temperature

Layer	Case D		Case H		Case I	
	WC	EC	WC	EC	WC	EC
1	0.93	-0.58	0.55	-0.55	1.02	-0.70
2	-0.68	0.84	-0.37	0.64	-0.78	0.92
1	0.93	-0.58	0.55	-0.55	1.02	-0.70
2	-0.68	0.84	-0.37	0.64	-0.78	0.92
3	-0.28	0.06	-0.15	0.08	-0.29	0.05
4	-0.01	0.04	0.00	0.01	0.00	0.04

(c) Effect of wind speed

The effect of varying the strength of the specified geostrophic wind, and therefore of the mean undisturbed flow, is shown by comparison of Case D with Cases E, F, and G in which the easterly geostrophic wind is 2, 6, and 8 m sec⁻¹, respectively. These tests tacitly involve the effect of shear in the lowest layer. A test of the effect of shear throughout the model depth was not possible with the cases chosen because of the uniform geostrophic profile specified for reasons cited in Section 2.1(a) on initial conditions.

Except for intensity, Case E exhibits similar characteristics to Case D with a somewhat shallower western seabreeze circulation and delayed development of the land breeze, the closed circulation of which first becomes evident at 0200 LST, three hours later than in Case D.

In addition to greater intensity of the perturbation flow relative to Case D, Case F also shows that the entire circulation system on the east drifts slowly westward due to stronger advection. By 0200 LST an extension of the land breeze circulation appears over the crest of the island at approximately 1 km. In time this cell expands, intensifies and sinks to the 500 m level becoming the eastern seabreeze cell during the next heating cycle. As in Case D, the western seabreeze cell is centered over the crest of the island with a region of sinking motion over the western slope.

The strength of the mean flow in Case G is reflected in the position of the western seabreeze cell over the west coast with rising motions over the entire island below 1 km. The land breeze circulation of the western seabreeze cell over the west coast with rising motions over the entire island below 1 km. The land breeze circulation is evident by 1700 LST, much earlier than in Case D and is centered

above the crest of the island at 1 km as opposed to 500 m in Case D. Figs 24 through 26 show the perturbation streamfunctions for Cases E - F at the times of maximum heating and cooling.

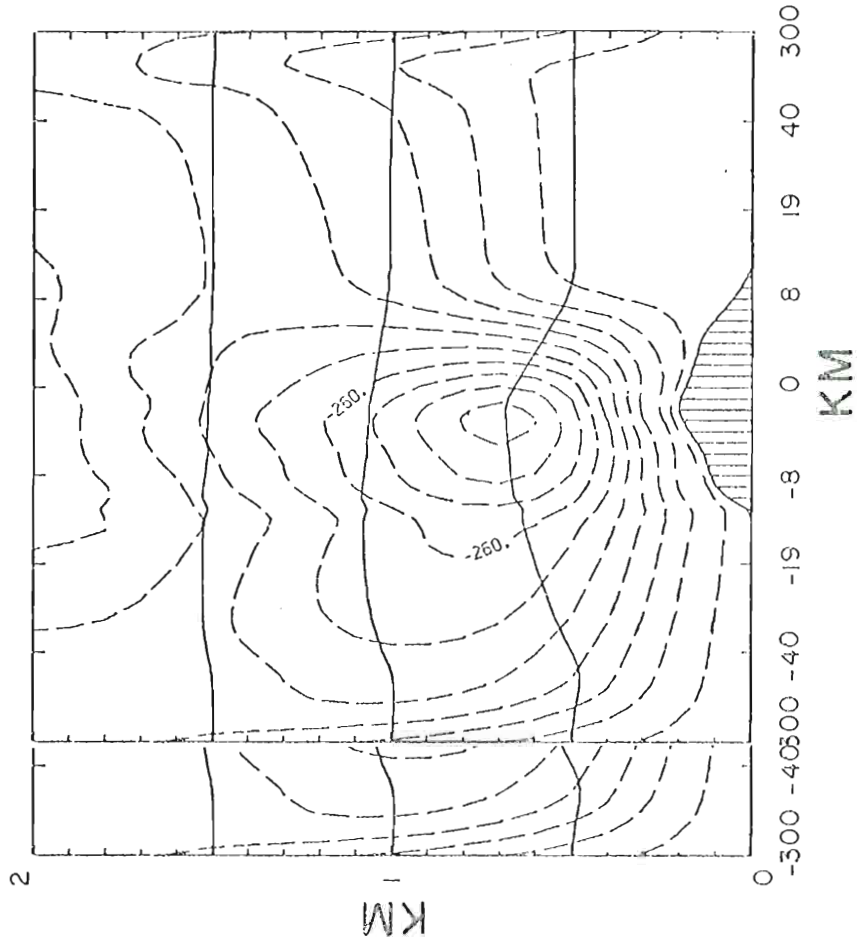
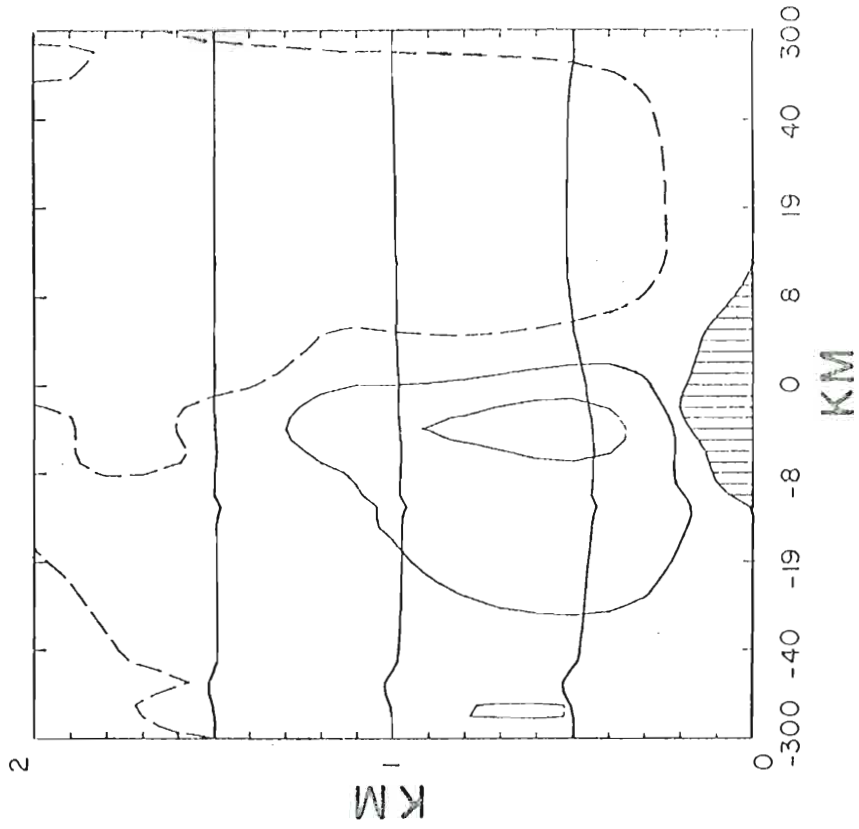


Fig. 24. Same as Fig. 7 but for Case E.

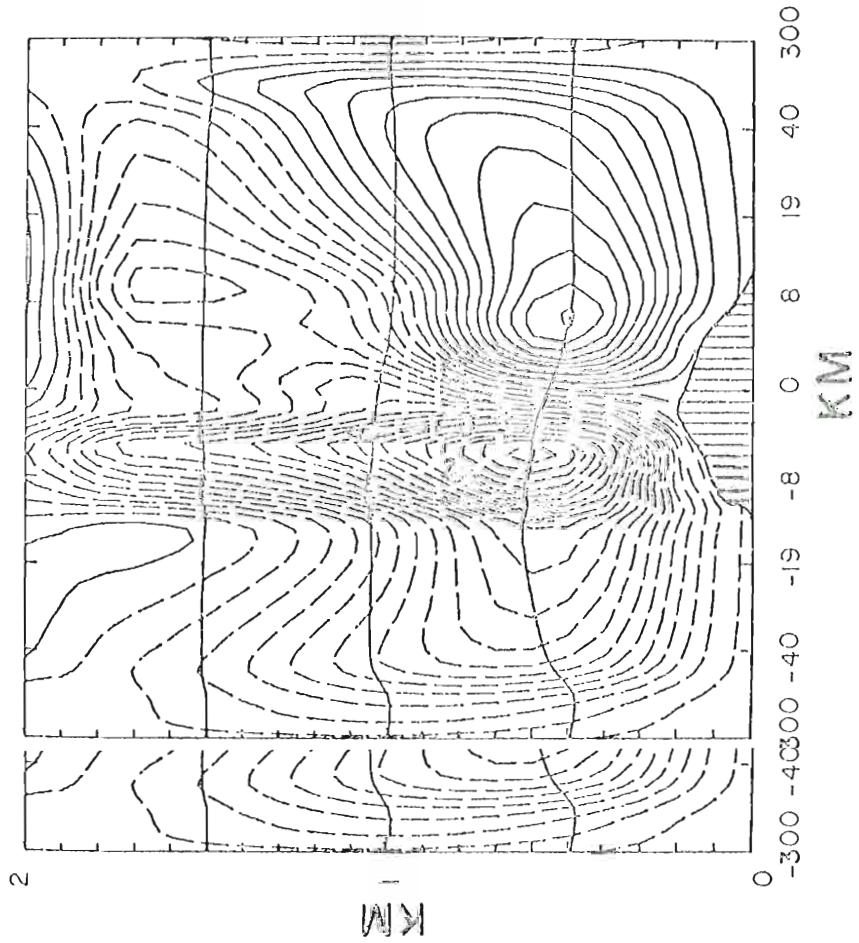
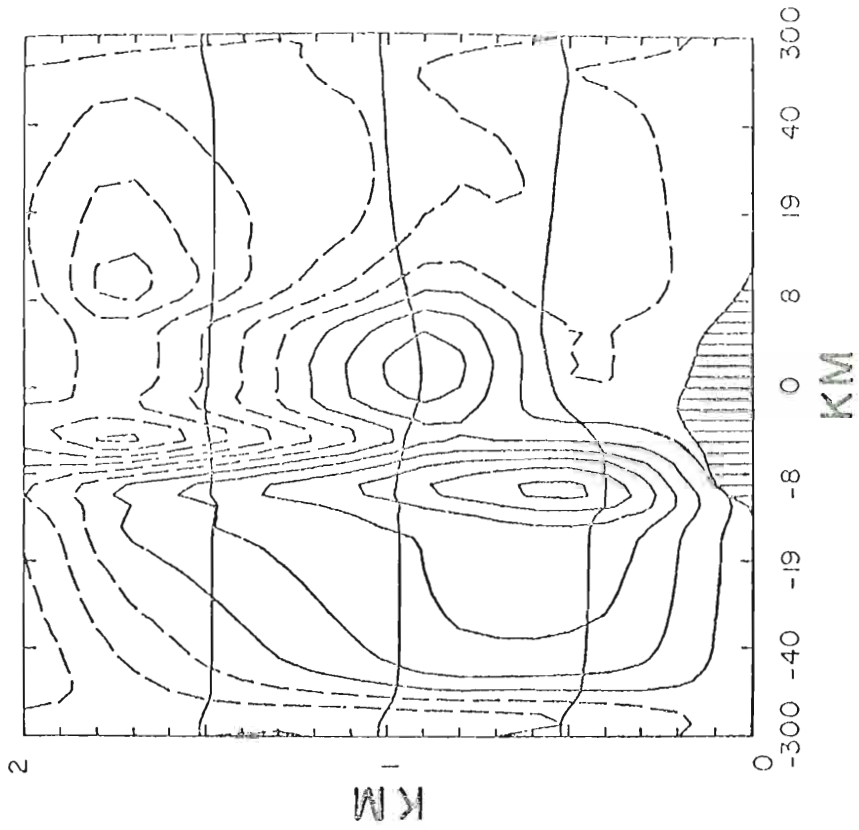


Fig. 25. Same as Fig. 7 but for Case F.

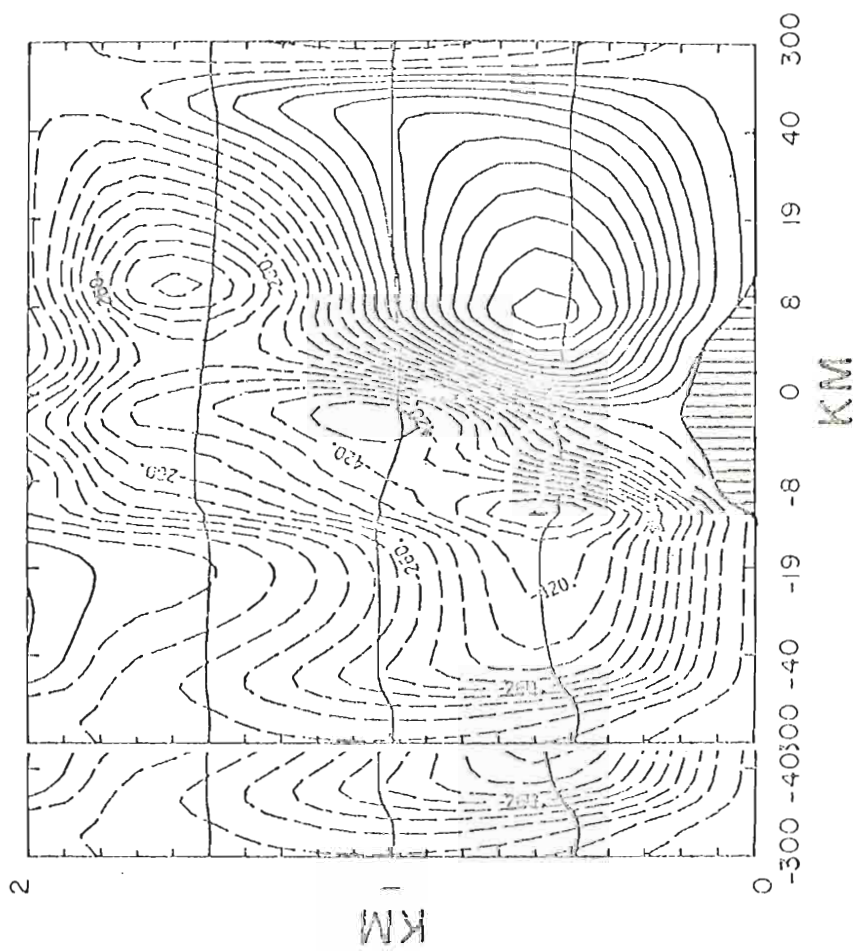
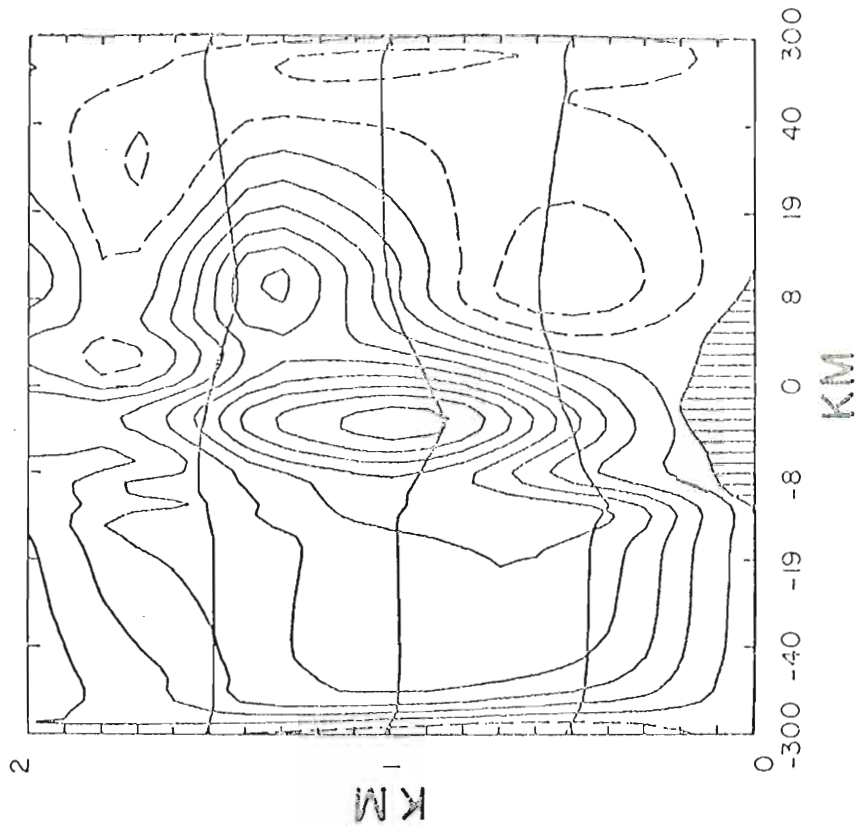


Fig. 26. Same as Fig. 7 but for Case G.

CHAPTER IV

COMPARISON WITH OBSERVATIONS

A major result of the observational study of the boundary layer over Barbados which provided the impetus for this investigation, was the anomaly of sinking motion mainly over the western part of the island during the day, and increased convective shower activity over the west coast at night.

Although methods of data analyses differ, the model results show encouragingly that in the presence of a mean flow a region of downward motion develops over the western slope of the real island during the day, while no such region appears over a flat island. An immediate implication of this result is the importance of topography in the modification of the low-level flow over isolated heat sources.

General comparisons of the model results with observations is complicated by the differences in data analysis techniques. In the observational studies, the island effect is determined by comparing the downwind properties of the flow with the conditions at the east coast, where it is assumed that the latter are representative of the undisturbed conditions upwind of the island. In the numerical model, island effects are deduced by comparing the perturbation circulations over a flat and a simulated real island representative of the Barbados topography. The perturbation circulations are derived as time responses to forcing on an initial undisturbed balanced state.

Some discrepancies between model results and observations are evident. For example, although the downward motions over the western part of the island seem realistic, the cross section of the perturbation circulation differs from that suggested by observations in which rising motions are indicated off both coasts. The occurrence of rising motions over the western part of the island at night in the model disagrees with observations which indicate rising motions over the east coast.

During the day the perturbation temperature field in the model shows the development of a plume downwind of the heat source, similar to the observed conditions. However, the maximum perturbation temperature in the model is confined, by design, to the center of the island while the maximum observed temperature departure occurs at approximately 500 m centered a few kilometers off the west coast. The observed perturbation moisture field shows a maximum deficit or drying of approximately 0.6 gm kg^{-1} at 500 m centered a few km. off the west coast, with little change between day and night. The model develops a moist layer near the 800 m level with maximum concentration over the western slope by day and over water by night in the presence of a mean flow. In still air, the maximum concentration occurs over water with a dry zone over land below 500 m. However, for cases with mean flow, if the model solutions over and downwind of the island are compared with those over the east coast as in the observational studies, we find in the lowest model layer a daytime temperature plume with a maximum of order 2 K over the east coast as in the observational studies, we find in the lowest model layer a daytime temperature plume with a maximum of order 2 K over the western slope and a nighttime deficit of order 0.1 K off the west coast. The perturbation moisture fields derived by this method show a deficit

of order 1 gm kg^{-1} by day and 1.5 gm kg^{-1} by night over the west coast. These results are in closer agreement with observations and suggest that the choice of data analysis techniques and reference standards are important to the results.

Comparisons of horizontal divergence fields between model results and observations are not made for two reasons:

- (1) in an x-z layered model, horizontal divergences of mass transport are more representative than velocity divergences, however observed mass transports are not available;
- (2) topographic influences are neglected in the observed divergence fields. Schaefer (1972) alludes to the importance of topography by showing that significant differences arise in divergence computations in different vertical coordinate systems.

CHAPTER V

SUMMARY AND CONCLUSIONS

A two-dimensional four-layer model is applied to an investigation of the boundary layer flow over Barbados, West Indies. The main feature of the study is the inclusion of topography together with variable surface heating in a non-linear numerical model which also includes variable surface drag coefficients and variable initial conditions of the flow fields. Initial conditions for cases with a basic current are generated with a dry version of the model as 7 1/2 day integrations to steady state from guess fields. Integrations with heating are carried out for as many as 3 days beyond the initial conditions without noticeable instability. A search of the open literature reveals that this combination of features has not been previously attempted in models of this type.

Moisture is included insofar as it affects momentum, and its effect is parameterized through the virtual temperature correction in the buoyancy term of the u-momentum equation. Latent heat release and condensation are excluded so that convective processes are not treated directly and are inferred only from the distribution of the perturbation vertical motion and moisture fields.

Model integrations are initiated from an initial balanced field or from a state of rest. Surface heating and moisture fluxes are re-

Model integrations are initiated from an initial balanced field or from a state of rest. Surface heating and moisture fluxes are re-distributed upwards by parameterized turbulent diffusion processes.

The major results of the model are summarized as follows:

1. Ekman balance as an initial condition should be avoided in boundary layer models which include topography and drastic changes in surface friction characteristics.
2. Nonlinear advection is important over topography, therefore linear analysis is inappropriate for models with topography.
3. Topography plays a dominant role in the modification of low-level flow over isolated heat sources, and
4. Small variations in topographic geometry can lead to significant changes in flow geometry.

With specific reference to Barbados, model case studies indicate the following:

1. The low-level land-sea breeze maxima propagate offshore in the absence of a mean flow.
2. Advection intensifies the perturbation circulations and inhibits the propagation of the low-level maxima.
3. The perturbation circulations are intensified in the presence of moisture, and in the absence of a land-sea surface moisture gradient.
4. Topography induces downward motions by day and upward motions at night over the western slope with maximum intensity of order 5 cm sec^{-1} near the time of maximum heating.
5. Precipitation inferred from perturbation flow and moisture fields is most likely at night over the western part of the island.
5. Precipitation inferred from perturbation flow and moisture fields is most likely at night over the western part of the island.

The propagation characteristics are unusual features of the Barbados land and seabreeze circulations which differ from previous model and

observational results of seabreeze circulations, and for which no corroborating or contradictory observational evidence is available. This suggests that an observational study of the Barbados seabreeze might be appropriate. For this purpose the scale of the circulations depicted in the perturbation streamfunctions implies that the network of 16 m towers used in the observational studies is inadequate, and that at least two intermediate observing sites are necessary. Observations would also be required from at least two ocean sites within 50 km of each coast in order to monitor the propagation of wind maxima. Simultaneous multi-level airborne observations along selected cross sections would be required to obtain the three-dimensional structure of the circulations.

Although the model does not reproduce all the observed characteristics of the boundary layer over Barbados, the results indicate that downward vertical motions over the western part of the island during the day are directly associated with the topography. Topography is neglected in the observational studies (Ulanski, 1971; and DeSouza, 1972) and in the momentum flux model (Garstang, 1967), in which the sinking motions are attributed to the downward flux of momentum associated with colder air bubbles subsiding through the boundary layer to replace rising warm air. It is argued in the above studies that vertical shear of the undisturbed horizontal wind throughout the boundary layer plays an important role in the vertical transfer of momentum. We note that the shear of the horizontal wind in the undisturbed state for the model occurs mainly in the lowest layer, and that over the island the sense of the shear immediately above the first layer is opposite to that normally

expected in the atmosphere. Nevertheless, the perturbation developed in response to surface heating shows daytime sinking motion over the western part of the island. Model tests show that this does not occur over a flat island. In this respect, the model suggests that topography presents a different mechanism for the daytime sinking motions.

APPENDICES

A. LIST OF SYMBOLS

A.1 Roman symbols

a	linear slope in coordinate stretching function.
a_0	24 hr mean land-sea temperature difference (constant term in Fourier expansion of surface forcing)..
a_n	Fourier cosine coefficients of surface heating.
b	constant in coordinate stretching function.
B	subscript denoting bottom of a model layer.
b_n	Fourier sine coefficients of surface heating.
c	multiplicative constant in coordinate stretching function.
C_D	surface drag coefficient.
c_p	specific heat capacity at constant pressure.
D	height of topography above reference level.
E	symbol for evaporative flux in moisture equation; symbol for θ or q in numerical scheme.
f	Coriolis parameter.
g	acceleration of gravity.
h	layer depth.
H	total depth from reference level to top of inert
h	layer depth.
H	total depth from reference level to top of inert layer; subscript for horizontal.

H_s	sensible heating rate.
k	von Karman's constant; subscript for general model layer.
K_{MH}, K_{QH}, K_{WH}	horizontal diffusion coefficients for momentum heat and moisture, respectively.
K_{MV}, K_{QV}, K_{VH}	vertical diffusion coefficients for momentum heat and moisture, respectively.
LST	local standard time.
p	pressure.
P_I, P_H	pressure at bottom and top of inert layer.
q	humidity mixing ratio.
\bar{q}	humidity mixing ratio at an interface between two layers.
q_l	surface humidity mixing ratio over land.
q_s	saturation humidity mixing ratio over water.
Q_s	vertical sensible heat flux.
R	gas constant; horizontal space scale for surface heating.
s	coordinate stretching function.
s', s''	first and second derivatives of coordinate stretching function.
T	temperature; subscript denoting top of a model layer.
\bar{T}	mean layer temperature. layer.
$\bar{\bar{T}}$	mean layer temperature.
T'	temperature deviation from initial value.
TOP	subscript denoting top of active model region.

u	east-west velocity component.
u^*	friction velocity.
u_g	east-west geostrophic wind component.
u_p	east-west velocity component at top of Prandtl layer.
v	north-south velocity component.
v_g	north-south geostrophic velocity component.
\vec{V}	vector wind.
w	vertical velocity component.
w_p	topographically induced vertical velocity at top of Prandtl layer.
x_0	distance of central grid point from west boundary.

A.2 Greek symbols

β	coefficient of thermal expansion.
β'	modified coefficient of thermal expansion.
ϵ	differences between layer densities.
θ	mean layer potential temperature.
$\bar{\theta}$	potential temperature at an interface between layers.
θ'	potential temperature deviation from initial value.
θ^*	mean layer virtual potential temperature.
κ	R/c_p
ν	time level index.
ξ	vertical deviation of interface from undisturbed position
ξ	vertical deviation of interface from undisturbed position.
ρ	mean layer density.
ρ_I	mean density of inert layer.

ρ_0	initial mean layer density.
σ	scaling factor for coordinate stretching function.
τ	interfacial stress.
ϕ	height of uppermost interface above reference level.
ψ	x-z streamfunction.

B. DERIVATION OF MODEL EQUATIONS

B.1 Introduction

The equations are derived in general for an n-level model, and are developed following the methods of Abdullah and O'Brien (1966), O'Brien and Reid (1967), Lavoie (1968, 1972), and O'Brien and Hurlburt (1972). Abdullah and O'Brien (1966) studied internal gravity waves of finite amplitude in a stratified incompressible atmosphere with a layered model. O'Brien and Reid (1967) used a two-layer model to study the response of the ocean to a stationary axially symmetric hurricane. Lavoie (1968, 1972) investigated lake effect storms with a layered model. His model region consisted of three layers, however all integrations were made for the middle (or so-called well mixed) layer. O'Brien and Hurlburt (1972) applied a two-layer model to the study of coastal upwelling. More recently Thompson and O'Brien (1973), and McNider and O'Brien (1973) have used two- and four-layer models, respectively, in further studies of coastal upwelling. The equations are derived with the inclusion of the stretch coordinates.

Assuming north-south homogeneity, independence in x of the horizontal diffusion coefficients, and neglecting vertical advection of momentum as discussed in Chapter 1, the equations of motion for the model become

model become

$$\frac{\partial u}{\partial t} + u \frac{\partial u}{\partial x} = - \frac{1}{\rho} \frac{\partial p}{\partial x} + fv + K_{MH} \frac{\partial^2 u}{\partial x^2} + \frac{1}{\rho} \frac{\partial \tau^x}{\partial z} \quad (B-1)$$

$$\frac{\partial v}{\partial t} + u \frac{\partial v}{\partial x} = -\frac{1}{\rho} \frac{\partial p}{\partial y} - fu + K_{MH} \frac{\partial^2 v}{\partial x^2} + \frac{1}{\rho} \frac{\partial \tau^y}{\partial z} \quad (\text{B-2})$$

$$\frac{\partial u}{\partial x} + \frac{\partial w}{\partial z} = 0 \quad (\text{B-3})$$

$$\frac{\partial \theta}{\partial t} + u \frac{\partial \theta}{\partial x} + w \frac{\partial \theta}{\partial z} = \frac{\theta}{\rho c_p T} H_s + K_{QH} \frac{\partial^2 \theta}{\partial x^2} \quad (\text{B-4})$$

$$\frac{\partial q}{\partial t} + u \frac{\partial q}{\partial x} + w \frac{\partial q}{\partial z} = E + K_{WH} \frac{\partial^2 q}{\partial x^2} \quad (\text{B-5})$$

$$\frac{\partial p}{\partial z} = -g\rho \quad (\text{B-6})$$

$$\rho = \rho_0 (1 - \beta T') \quad (\text{B-7})$$

B.2 The layer averaged equations

Eqs. (B-1) through (B-5) are integrated over layer depth h of each layer with the assumption of vertical homogeneity of velocity, temperature, moisture, and density within each layer. In the following development the subscript k is used to identify the k^{th} layer, superscripts x and y to denote direction of stresses, and the letters B , T , to denote the height of the lower and upper interfaces of the k^{th} layer measured from the reference level. Subscripts indicating grid position in the horizontal are omitted for simplicity. The subscripts t are used to denote local time differentiation while subscripts x and s are used for space differentiation. Multiple differentiation is denoted by the appropriate multiple subscripts.

appropriate multiple subscripts.

(a) u-momentum

The layer averaged version of (B-1) is

$$u_t + uu_x = -\frac{1}{\rho h} \int_B^T p_x dz + fv + K_{MH} u_{xx} + \frac{1}{\rho h} \left[\tau_T^x - \tau_B^x \right]$$

Using (B-6) and Fig. 1, the pressure at a point P in layer k at a height z above the reference level is given by

$$p(z) = P_I + g \sum_{j=k+1}^n \rho_j h_j + g \rho_k \left(\sum_{j=1}^k h_j + D - z \right)$$

where P_I is the pressure at the interface between the uppermost active layer and the inert layer, and D is the height of the topography above the reference level. The equation for $p(z)$ is conveniently rewritten as

$$p(z) = P_I + g \rho_k \left(\sum_{j=1}^n h_j + D - z \right) - g \sum_{j=k+1}^n \left\{ (\rho_k - \rho_j) h_j \right\}$$

We now let

$$\phi = \sum_{j=1}^n h_j + D$$

By our definition of the inert layer, if we consider the height H to be the level at which $\partial P_H / \partial x = 0$, we may define the pressure P_I as

$$P_I = P_H + g \rho_I (H - \phi)$$

where ρ_I is the inert layer mean density, then

$$p(z) = P_H + g \left\{ \rho_I H + (\rho_k - \rho_I) \phi - \rho_k z - \sum_{j=k+1}^n (\rho_k - \rho_j) h_j \right\}$$

Assuming that $\partial \rho_I / \partial x = 0$, we have by differentiation w.r. to x

$$p_x(z) = g \left[(\rho_k - \rho_I) \phi_x + \rho_{kx} \phi - \rho_{kx} z - \sum_{j=k+1}^n \left\{ (\rho_k - \rho_j) h_{jx} + (\rho_k - \rho_j)_x h_j \right\} \right]$$

$$p_x(z) = g \left[(\rho_k - \rho_I) \phi_x + \rho_{kx} \phi - \rho_{kx} z - \sum_{j=k+1}^n \left\{ (\rho_k - \rho_j) h_{jx} + (\rho_k - \rho_j)_x h_j \right\} \right]$$

Averaging in z within the kth layer, all terms retain their form except that

$$\begin{aligned} \frac{1}{h_k} \int_B^T \rho_{kx} z \, dz &= \frac{\rho_{kx}}{2h_k} (z_T^2 - z_B^2) \\ &= \frac{\rho_{kx}}{2h_k} [(z_T - z_B)(z_T + z_B)] \end{aligned}$$

But $z_T - z_B = h_k$, since $z_T = \sum_{j=1}^k h_j + D$ and $z_B = \sum_{j=1}^{k-1} h_j + D$

Therefore

$$\frac{1}{h_k} \int_B^T \rho_{kx} z \, dz = \rho_{kx} \left[\sum_{j=1}^k h_j + D - \frac{1}{2} h_k \right]$$

and

$$\begin{aligned} \frac{1}{h_k} \int_B^T p_x(z) \, dz &= g \left[(\rho_k - \rho_I) \phi_x + \rho_{kx} \phi - \rho_{kx} \left(\phi - \sum_{j=k+1}^n h_j - \frac{1}{2} h_k \right) \right. \\ &\quad \left. - \sum_{j=k+1}^n \left\{ (\rho_k - \rho_j) h_{jx} + (\rho_k - \rho_j)_x h_j \right\} \right] \\ &= g \left[\epsilon_k^k \phi_x + \frac{1}{2} h_k \rho_{kx} - \sum_{j=k+1}^n \left\{ \epsilon_k^j h_{jx} - h_j \rho_{jx} \right\} \right] \end{aligned}$$

where $\epsilon_k^k = \rho_k - \rho_I$ and $\epsilon_k^j = \rho_k - \rho_j$.

It will be shown later that the horizontal gradient of density may be approximated by horizontal potential temperature gradient in the form

$$\rho_x = -\rho_0 \beta' \theta'_x$$

where β' is a function of the coefficient of thermal expansion and height (pressure).

It was shown in Section 2.4 on stretch coordinates that the height (pressure).

It was shown in Section 2.4 on stretch coordinates that the first and second derivatives in x are given by

$$\frac{\partial}{\partial x} = s' \frac{\partial}{\partial s} \quad \text{and} \quad \frac{\partial^2}{\partial x^2} = s'' \frac{\partial}{\partial s} + (s')^2 \frac{\partial^2}{\partial s^2}$$

where $s' = \frac{\partial s}{\partial x}$, $s'' = \frac{\partial^2 s}{\partial x^2}$ and $s(x)$ is the stretch function. Incorporating the above transformations, the virtual potential temperature correction, and the flux form of the advective term, the layer averaged u-momentum equation for layer k is

$$\begin{aligned} u_{kt} = & -\frac{1}{2} s' (u_k u_k)_s - \frac{gs'}{\rho_{0k}} \left[\epsilon_k^k \phi_s - \frac{1}{2} \rho_{0k} h_k \beta'_k \theta_{ks}^{*'} \right. \\ & \left. - \left\{ \sum_{j=k+1}^n (\epsilon_k^j h_{js} + \rho_{0j} h_j \beta'_j \theta_{js}^{*'}) \right\} \right] + f v_k \\ & + K_{MH} \left[s'' u_{ks} + (s')^2 u_{kss} \right] + \frac{1}{\rho_{0k} h_k} \left\{ \tau_T^x - \tau_B^x \right\} \quad (B-8) \end{aligned}$$

(b) v-momentum

The pressure gradient term of the v-momentum equation is simply assumed to balance the imposed geostrophic u-component of the wind, i.e.,

$$-\frac{1}{\rho} \frac{\partial p}{\partial y} = f u_g$$

Other terms in this equation are treated analogously with similar terms in the u-momentum equation, thus the equation becomes

$$\begin{aligned} v_{kt} = & -s' \left[(u_k v_k)_s - v_k u_{ks} \right] + f (u_g - u_k) \\ & + K_{MH} \left[s'' v_{ks} + (s')^2 v_{kss} \right] + \frac{1}{\rho_{0k} h_k} \left[\tau_T^y - \tau_B^y \right] \quad (B-9) \end{aligned}$$

(c) Mass continuity

Applying the assumption of north-south homogeneity, the continuity equation for shallow convection after Dutton and Fichtl (1969) is

Applying the assumption of north-south homogeneity, the continuity equation for shallow convection after Dutton and Fichtl (1969) is

$$\frac{\partial u}{\partial x} + \frac{\partial w}{\partial z} = 0$$

Integrating with respect to z we have

$$h \frac{\partial u}{\partial x} + w_T - w_B = 0$$

Treating the interfaces bounding the k^{th} layer as material surfaces, we let ξ represent a deviation from their undisturbed positions, and define the surfaces by

$$F_T = \sum_{j=1}^k h_j + D - \xi_T$$

$$F_B = \sum_{j=1}^{k-1} h_j + D - \xi_B$$

where $\frac{dF}{dt} = 0$ satisfies the kinematic condition at the surfaces. Thus

$$\frac{d}{dt} (F_T) = \sum_{j=1}^k \frac{dh_j}{dt} + \frac{dD}{dt} - \frac{d}{dt} (\xi_T) = 0$$

By definition $\frac{dD}{dt} = w_P$ is the topographically induced vertical motion at the top of the Prandtl layer, and $\frac{d}{dt} (\xi_T) = w_T$ is the vertical motion at the upper interface.

We write for the upper interface

$$w_T = w_P + \sum_{j=1}^k \frac{dh_j}{dt} \quad (\text{B-10})$$

and similarly for the lower interface

$$w_B = w_P + \sum_{j=1}^{k-1} \frac{dh_j}{dt}$$

Substituting in the integrated equation we have

$$h_k \frac{\partial u_k}{\partial x} + \frac{dh_k}{dt} = 0 \quad (\text{B-11})$$

$$h_k \frac{\partial u_k}{\partial x} + \frac{dh_k}{dt} = 0 \quad (\text{B-11})$$

which can be rewritten in stretch coordinates as

$$h_{kt} + s' (u_k h_k)_s = 0 \quad (\text{B-12})$$

From (B-10) and (B-11) we derive the diagnostic equation for the vertical motion at the top of level k as

$$w_T = w_P - \sum_{j=1}^k h_j u_{jx} \quad (\text{B-13})$$

where $w_P = \frac{dD}{dt} = u_P \frac{\partial D}{\partial x}$

For computational purposes $u_P = u_1$.

(B-12) is the continuity equation for the model.

(d) Heat

Combining Eqs. (B-3) and (B-4), we have

$$\theta_t + (u\theta)_x + (w\theta)_z = \frac{\theta}{\rho c_p T} H_s + K_{QH} \theta_{xx}$$

H_s , the rate of sensible heating by turbulent mixing, is the divergence of the vertical flux of sensible heat defined by

$$H_s = - \frac{\partial Q_s}{\partial z}$$

The layer averaged equation is

$$\theta_{kt} + u_k \theta_{kx} + \frac{1}{h_k} \left[(w\theta)_T - (w\theta)_B \right] = - \frac{\theta_k}{\rho_{0k} c_p \bar{T}_k h_k} \left[Q_{sT} - Q_{sB} \right] + K_{QH} \theta_{kxx}$$

Note that T and ρ have been replaced by mean layer values \bar{T}_k and ρ_{0k} .

Note also that w is calculated at the interfaces while θ is a layer mean value, therefore the vertical advection may be written as

$$\frac{1}{h_k} \left[w_T \bar{\theta}_T - w_B \bar{\theta}_B \right]$$

$$\frac{1}{h_k} \left[w_T \bar{\theta}_T - w_B \bar{\theta}_B \right]$$

where $\bar{\theta}_T, \bar{\theta}_B$ are interfacial temperatures obtained from the mean value

in adjacent layers. The vertical flux of sensible heat Q_s which provides the main driving in the model is formulated in two ways. The shear form utilizing the vertical diffusion coefficient profile is applied at all levels in the model. An additional bulk aerodynamic form (after Lavoie, 1968) is used at the surface only. Use of the shear form at the surface allows the generation of a thermal circulation in an initially static condition, which would not be possible with the bulk term because of its dependence on wind speed. The shear form of Q_s is

$$Q_s = - \rho c_p K_{QV} \frac{\partial \theta}{\partial z} .$$

The bulk form of Q_s as derived by Lavoie (1968) is as follows.

Expressing the zonal stress as

$$\tau^x = \rho K_{MV} \frac{\partial u}{\partial z}$$

where K_{MV} is the vertical diffusion coefficient for momentum, and approximating derivatives by finite differences, we write

$$\frac{Q_s}{\tau^x} = - c_p \frac{K_{QV}}{K_{MV}} \frac{\Delta \theta}{\Delta u}$$

Re-defining the stress in bulk aerodynamic form, we have

$$\tau^x = \rho C_D |\underline{v}| \Delta u$$

where Δu is the x-directed interfacial relative velocity, and

$$Q_s = - \rho c_p C'_D |\underline{v}| \Delta \theta$$

where

$$C'_D = C_D \frac{K_{QV}}{K_{MV}}$$

$$C'_D = C_D \frac{K_{QV}}{K_{MV}}$$

$$|\underline{v}| = \sqrt{u^2 + v^2}$$

and $\Delta \theta$ is the temperature difference across an interface defined by

$$(\Delta\theta)_T = \theta_{k+1} - \theta_k$$

and

$$(\Delta\theta)_B = \theta_k - \theta_{k-1}$$

In this model we assume $K_{QV} = K_{TV}$ so that

$$C'_D = C_D$$

Since Q_s is required at the upper and lower interfaces for each layer, the interfacial values of $|V|$ are obtained as averages of the wind speeds in the adjacent layers, and the values of the diffusion coefficient are calculated by the method suggested by O'Brien (1970). Vertical derivatives and differences are treated as finite differences between the layer (upper - lower). However, mean layer densities are used since the interfacial values differ slightly from the mean layer values. If we now approximate θ_k/\bar{T}_k as 1 and introduce the above expressions for the advective and sensible heating terms together with the stretch coordinates, the heat equation becomes

$$\begin{aligned} \theta_{kt} = & -s'(u_k \theta_k)_s - \frac{1}{h_k} \left[w_T \bar{\theta}_T - w_B \bar{\theta}_B \right] + K_{QH} \left[s'' \theta_{ks} + (s')^2 \theta_{kss} \right] \\ & - \frac{1}{h_k} \left[(K_{QV} \theta_z)_B - (K_{QV} \theta_z)_T \right] - \frac{1}{h_1} \left[C_D |V|_1 (\Delta\theta)_B \right] \end{aligned} \quad (B-14)$$

The last term on the right hand side is evaluated only at the surface. The main forcing in the model is accomplished by surface heating acting through the last two terms of Eq. (B-14).

(e) Moisture

(e) Moisture

The moisture equation is derived in a manner completely analogous to the heat equation. The flux form of Eq. (B-5) is

$$q_t + (uq)_x + (wq)_z = E + K_{WH} q_{xx}$$

E is the divergence of the vertical flux of moisture defined as

$$E = - \frac{1}{\rho} \frac{\partial}{\partial z} (\rho K_{WV} \frac{\partial q}{\partial z}) .$$

Following the procedure adopted for the heat equation, the moisture equation becomes

$$\begin{aligned} q_{kt} = & - s' (u_k q_k)_s - \frac{1}{h_k} [w_T \bar{q}_T - w_B \bar{q}_B] \\ & - \frac{1}{h_k} [(K_{QV} q_z)_B - (K_{QV} q_z)_T] - \left\{ \frac{1}{h_1} C_D |v|_1 (\Delta q)_B \right\} \\ & + K_{QH} [s'' q_{ks} + (s')^2 q_{kss}] \end{aligned} \quad (B-15)$$

(f) State

The linearized equation of state is

$$\rho = \rho_0 (1 - \beta T')$$

where ρ_0 is initial mean density

β is the coefficient of thermal expansion, $\left(- \frac{1}{\rho} \frac{\partial \rho}{\partial T} \right)_p$

and T' is the deviation from the initial temperature.

Using Poisson

$$T(t) = \theta(t) \left\{ \frac{p(t)}{p_{00}} \right\}^\kappa$$

where $p_{00} = 1000$ mb and $\kappa = R/c_p$.

Expanding the quantity in brackets we have

$$\frac{p(t)}{p_{00}} = 1 - \frac{p_{00} - p(t)}{p_{00}}$$

In a shallow model (2 km) the time variations in pressure in any layer

In a shallow model (2 km) the time variations in pressure in any layer during a heating cycle is small relative to 1000 mb, therefore we assume

$$\frac{P_{00} - p(t)}{P_{00}} \approx \frac{P_{00} - p(0)}{P_{00}} \ll 1$$

and we write

$$\left(\frac{p(t)}{P_{00}}\right)^{\kappa} = (1 - p'')^{\kappa} \approx 1 - \kappa p'' \approx 1 - \kappa p'$$

where

$$p' = \frac{P_{00} - p(0)}{P_{00}}$$

and

$$p'' = \frac{P_{00} - p(t)}{P_{00}}$$

$$\begin{aligned} T(t) &= (T(0) + T'(t)) \\ &= \{\theta(0) + \theta'(t)\} \left\{ \frac{p(t)}{P_{00}} \right\}^{\kappa} \\ &\approx \{\theta(0) + \theta'(t)\} (1 - \kappa p'') \\ &\approx \{\theta(0) + \theta'(t)\} (1 - \kappa p') \\ T(0) &= \theta(0) \left\{ \frac{p(0)}{P_{00}} \right\}^{\kappa} \approx \theta(0) (1 - \kappa p') \end{aligned}$$

$$\therefore T'(t) \approx \theta'(t) (1 - \kappa p')$$

and

$$\rho \approx \rho_0 [1 - \beta(1 - \kappa p') \theta']$$

writing $\beta' = \beta(1 - \kappa p')$, the equation of state becomes

$$\rho \approx \rho_0 (1 - \beta' \theta') \quad (\text{B-16})$$

and the horizontal density gradient is expressed as

$$\rho_x \approx -\rho_0 \beta' \theta'_x$$

and the horizontal density gradient is expressed as

$$\rho_x \approx -\rho_0 \beta' \theta'_x$$

REFERENCES

- Abdullah, A. J., and J. J. O'Brien, 1966: Internal gravity waves of finite amplitude in a stratified incompressible atmosphere. A quasi characteristic method. NCAR Manuscript No. 218, 54 pp.
- Bhumralkar, C., 1972: An observational and theoretical study of atmospheric flow over a heated island. Final report prepared for NSF-Grant GA-1456, 150 pp.
- DeSouza, R. L., 1972: A study of atmospheric flow over a tropical island. Ph.D. Dissertation, The Florida State University, 204 pp.
- Dutton, J. A., and G. H. Fichtl, 1969: Approximate equations of motion for gases and liquids. J. Atmos. Sci., 26, 241-254.
- Estoque, M. A., 1961: A theoretical investigation of the sea breeze. Quart. J. Roy. Meteor. Soc., 87, 136-146.
- _____, 1962: The sea breeze as a function of the prevailing synoptic situation. J. Atmos. Sci., 19, 244-250.
- _____, and C. M. Bhumralkar, 1969: Flow over a localized heat source. Mon. Wea. Rev., 97, 850-859.
- Fisher, E. L., 1961: A theoretical study of the sea breeze. J. Meteor., 18, 216-233.
- Garstang, M., 1964: Distribution and mechanism of energy exchange between the tropical oceans and atmosphere. Ph.D. Dissertation, The Florida State University, 177 pp.
- _____, 1967: The role of momentum exchange in flow over a heated island. Proceedings of the 1967 Army Conference on Tropical Meteorology, Univ. of Miami, Florida, 178-195.
- Gammeltvedt, A., 1969: A survey of finite-difference schemes for primitive equations for a barotropic fluid. Mon. Wea. Rev., 97, 384-404.
- Holley, R. M., 1972: Surface temperatures of a tropical island and surrounding ocean measured with an airborne infrared radiometer. M.S. Thesis, The Florida State University, 249 pp.
- Holley, R. M., 1972: Surface temperatures of a tropical island and surrounding ocean measured with an airborne infrared radiometer. M.S. Thesis, The Florida State University, 249 pp.

- Lavoie, R. L., 1968: A mesoscale numerical model and lake-effect storms. Ph.D. Dissertation, The Pennsylvania State University, 102 pp.
- _____, 1972: A mesoscale numerical model of lake-effect storms. J. Atmos. Sci., 29, 1025-1040.
- Malkus, J. S., and M. E. Stern, 1953: The flow of a stable atmosphere over a heated island - Part I. J. Meteor., 10, 30-41.
- McNider, R. T., and J. J. O'Brien, 1973: A multi-layer transient model of coastal upwelling. J. Phys. Oceanogr., 3, 258-273.
- Neumann, J., and Y. Mahrer, 1971: A theoretical study of land and sea breeze circulation. J. Atmos. Sci., 28, 532-542.
- O'Brien, J. J., 1970: A note on the vertical structure of the eddy exchange coefficient in the planetary boundary layer. J. Atmos. Sci., 27, 1213-1215.
- _____, and R. O. Reid, 1967: The non-linear response of a two-layer, baroclinic ocean to a stationary, axially symmetric hurricane. Part I. Upwelling induced by momentum transfer. J. Atmos. Sci., 42, 197-207.
- _____, and H. Hurlburt, 1972: A numerical model of coastal upwelling. J. Phys. Oceanogr., 2, 14-26.
- Olfe, D. B., and R. L. Lee, 1971: Linearized calculations of urban heat island convection effects. J. Atmos. Sci., 28, 1374-1388.
- Pielke, R. A., 1973: A three dimensional numerical model of the sea breezes over South Florida. Ph.D. Dissertation, The Pennsylvania State University, 135 pp.
- Raymond, D. J., 1972: Calculation of air flow over an arbitrary ridge including diabatic heating and cooling. J. Atmos. Sci., 29, 836-843.
- Schaefer, J. T., 1973: On the computation of the surface divergence field. J. Appl. Meteor., 12, 546-547.
- Schulman, E. F., 1970: The antarctic circumpolar current. Proceedings of the 1970 Summer Computer Simulation Conference, Denver, Colorado, 955-961.
- Smith, R. C., 1955: Theory of airflow over a heated land mass. Quart. J. Roy. Meteor. Soc., 81, 382-395. Denver, Colorado, 955-961.
- Smith, R. C., 1955: Theory of airflow over a heated land mass. Quart. J. Roy. Meteor. Soc., 81, 382-395.
- _____, 1957: Air motion over a heated land mass: II. Quart. J. Roy. Meteor. Soc., 81, 243-256.

- Stern, M. E., and Malkus, J. S., 1953: The flow of a stable atmosphere over a heated island - Part II. J. Meteor., 10, 105-120.
- Thompson, J. D., and J. J. O'Brien, 1973: Time dependent coastal upwelling. J. Phys. Ocean., 3, 33-46.
- Ulanski, S. L., 1971: A kinematic and thermodynamic description of the Prandtl layer circulation over Barbados. M.S. Thesis, The Florida State University, 218 pp.

VITA

John D. Lee was born on April 22, 1929 in Trinidad, West Indies. He received his high school education at St. Mary's College, Port-of-Spain, Trinidad, where he obtained the Cambridge Higher School certificate in 1947.

He attended Florida State University where he received the Bachelor of Science degree in 1970. He received his M.S. in Meteorology in 1971, continuing towards the Ph.D. degree also in Meteorology.